ABSTRACT

LI, XIANG. Universal Density Shift Coefficients for Hydrodynamic Transport Properties of a Unitary Fermi Gas . (Under the direction of John E. Thomas).

This dissertation present the first measurement of the universal density shift coefficients for the shear viscosity and thermal conductivity of a unitary Fermi gas in the normal fluid regime. The experiment was performed with a near homogeneous unitary Fermi gas confined in a box potential, which is created by two Digital Micromirror Devices (DMDs). A third DMD was implemented to independently control the perturbation beam, which enables a full dynamic control of the perturbing potential. We developed a kinetic theory model to extract the hydrodynamic relaxation times τ_η and τ_κ from the time-dependent free-decay of a spatially periodic density perturbation, yielding the static transport properties and density shifts, corrected for finite relaxation time.

Universal Density Shift Coefficients for Hydrodynamic Transport Properties of a Unitary Fermi Gas

by
Xiang Li

A dissertation submitted to the Graduate Faculty of
North Carolina State University
in partial fulfillment of the
requirements for the Degree of
Doctor of Philosophy

Physics

Raleigh, North Carolina
2024

APPROVED BY:

Thomas Schaefer

Chueng Ji

Xiaoning Jiang

John E. Thomas
Chair of Advisory Committee

DEDICATION

To my families and Ying

BIOGRAPHY

Xiang Li was born in Tongchuan, Shaanxi, China on February 1993. He went to Shandong University for undergraduate, obtained Bachelor's degree in mathematics in 2015. He was enrolled in the graduate program at North Carolina State University in August 2018 and joined Prof. John Thomas' group in the summer of 2019, conducting cold atom experiments.

ACKNOWLEDGEMENTS

First I want to thank my advisor Prof. John Thomas. I still remember the day I stepped into John's office and asked him if I could join the lab, even though I knew almost nothing about experiments on cold atoms at that time. I asked John because his presentation for us new graduate students interested me most. He agreed I started in the summer, see if I could fit the lab. Since then, it's been five years. I'm extremely grateful to have John as my mentor, and learn from him, not just physics.

Next, I would like to thank Ilya Arakelyan, former research scientist in our group, also the best person I ever worked with. Every time when there was some issue I couldn't figure out how to fix, the first idea was " Is Ilya here today?". He is the person who knows how everything in the lab should work and taught me from scratch. Once I thought he would "babysit" us until we all graduate, I was wrong. But he still came back every time we needed him most and saved the day.

Jingjing joined the group one year later than me but graduated with top speed. Although she worked mainly in the other lab, she could always help me from time to time when I was the only student running the experiment. We even rebuilt the oven together, which have not been done for a decade since the group moved to NC State.

I want to thank the previous members in our group, Saeed Pegahan and Xin Wang. When I joined the group, they were the senior students. Xin taught me how to run the experiment in the lab. Saeed, although we did not work in the same lab, was always glad to discuss any problem I had , and TVs we both liked. Camen Royse was another student who joined the group the same time with me.

Besides my colleagues in JET lab, I would like to thank my committee members, Prof. Thomas Schaefer, Prof. Chueng Ji and Prof. Xiaoning Jiang. I want to thank Rhonda Bennet, the graduate coordinator in physics department. She's always there to help everyone of us, it's so good to have you as our coordinator.

I would like to thank all my friends in RCCC, who have helped me a lot since I came to the U.S., especially during the pandemic.

Finally, all of my work could not have been done without the support of my family. My parents, my sister and my two nieces, Lingling and Yuanyuan. I missed them so much.

Last but not least, I would like to thank my girlfriend Ying. Thank you for being there for me all the time for the past five years.

TABLE OF CONTENTS

LIST OF FIGURES

CHAPTER

1

INTRODUCTION

1.1 History

In 1995, the first Bose-Einstein condensate (BEC) were created in dilute vapors of alkali-metal atoms [Anderson et al. (1995); Bradley et al. (1995); Davis et al. (1995)], marking the new beginning of ultracold atomic physics. In the next few years, most studies, both experimental and theoretical, were devoted to the quantum gas of Bosons and were aimed at investigating the important consequences of BEC, which, before 1995, remained an elusive and inaccessible phenomenon. Soon after, the attention of experimentalists and theorists was oriented toward the study of Fermi gases.

When we cool down Bosons and Fermions (single component), we can immediately see the difference. The Bose gas shrinks continuously and form a tiny BEC at last , while the Fermi gas stops shirking at some point due to Pauli blocking [Truscott et al. (2001)], as shown in Figure 1.1. The first degenerate Fermi gas was obtained in JILA [DeMarco and Jin (1999)]. They worked with two spin components of ^{40}K atoms with attractive interaction, they achieved temperatures on the order of fractions of Fermi Temperature. The Bardeen-Cooper-Schrieffer (BCS) theory suggests that two atoms with different spin states should form Cooper pair and the gas should exhibit superfluidity at sufficient low temperature. However, the critical temperature of traditional BCS type superfluid is very small, typically less than 1% of Fermi temperature.

The Fermi gases created above are extremely dilute, the critical temperature required to enter superfluid phase was too small to reach in these experiments.

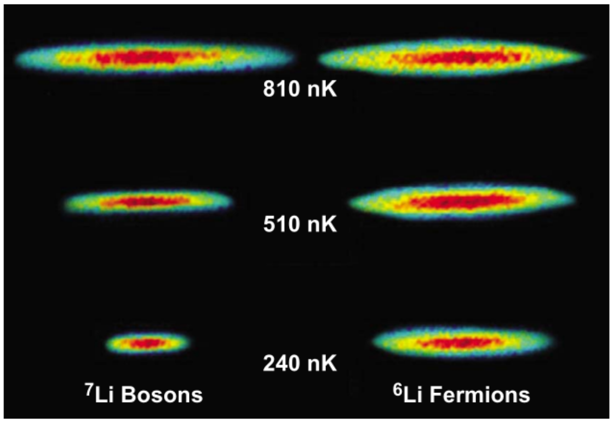

Figure 1.1: Simultaneous cooling of a bosonic and fermionic gas of ^{7}Li and ^{6}Li to quantum degeneracy. In the case of Fermi gas, the Fermi pressure prevents the atom cloud from shirking further in space as quantum degeneracy is approached. Figure adopted from [Bloch et al. (2008)], original from [Truscott et al. (2001)].

It did not take very long to achieve superfluidity with Fermi gas, as physicists realized that a crucial tool to do it is provided by accessing the Feshbach resonance. We will introduce Feshbach resonance in detail in the next chapter. In a nutshell, this resonance characterize the two-body interaction and permit one to change the value and even the sign of the scattering length by simply tuning the external magnetic field [Chin et al. (2010)]. When we tune the magnetic field toward Feshbach resonance, the interaction gets stronger and stronger. Right at Feshbach resonance, the scattering length divergence, the interaction is as strong as quantum mechanics allows. In 2002, our group reported the first experimental realization of such strongly interacting Fermi gas with ^{6}Li atoms [O'hara et al. (2002)]. Right around Feshbach resonance, which is called unitary regime, the gas is peculiar since it is simultaneously dilute (the effective range of interacting potential is much smaller than the inter-particle distance) and strongly interacting (the scattering length is much larger than the inter-particle distance). All length scales associated with interactions disappear from the problem and the system is expected to exhibit a universal behavior, independent of the details of the interatomic potential [Zwierlein (2016)].

Such strong interaction dramatically changes the properties of the system. One of the remarkable properties is the rising of critical temperature, which is now on the order of the Fermi temperature, $T_C \simeq 0.17\,T_F$ when at resonance. The superfluid phase is much easier to access in this case. The first evidence of superfluidity came from the measurements of collective oscillation [Kinast et al. (2004)]. Another important evidence is the measurement of the pairing gap observed in radio-frequency excitation spectra [Chin et al. (2004)]. But neither of these evidence are conclusive enough since these phenomena can also occur in the normal fluid regime. Convincing proof of superfluidity was provided by the observation of quantized vortices that were realized on both sides of Feshbach resonance [Zwierlein et al. (2005)].

No other system has ever been observed with a transition temperature as high as roughly 17% of their Fermi temperature. If we scale to the density of electrons in metal, T_C would occur far above room temperature. The strongly interacting Fermi gas has become one of the most important candidates to study high-temperature superconductor.

1.2 Motivation

The topic of this thesis does not include superfluid. Instead, we focus on the normal fluid regime, i.e. $T > T_C$. When the temperature is above superfluid transition T_C, the unitary Fermi gas is a single component normal fluid and obeys hydrodynamic transport laws for universal system.

The unitary Fermi gas is a hydrodynamic system, this is conformed by the observation of elliptical expansion after releasing the gas from the harmonic trap [O'hara et al. (2002)]. In 2012, our group did the first comprehensive measurement of shear viscosity with an expanding unitary Fermi gas [Cao et al. (2011)]. Over the years many group around the world have done various transport measurements of unitary Fermi gas, for example the spin transport or spin diffusivity [Sommer et al. (2011)], solitons and vortices [Yefsah et al. (2013); Ku et al. (2014)], second sound [Sidorenkov et al. (2013)], charge transport and conductivity [Krinner et al. (2015)]. All these experiments were done in a harmonic trap, the density varies from central maximum to zero at the edge. This large density variation is very unfriendly for the transport measurement. First, the inhomogeneous density profile means we are measuring an inhomogeneous transport coefficients. That's why the shear viscosity measured in [Cao et al. (2011)] is a cloud averaged value. Second, hydrodynamics does not valid all the way to the edge because the cloud is so dilute. To overcome these issues caused by inhomogeneous density, many groups, including us, switched to the techniques of optical box potential, where the density is nominally uniform. Not only did it resolve the issue of inhomogeneous density, but also enables new measurements of hydrodynamic transport properties.

Measurements of the universal hydrodynamic transport properties of unitary Fermi gas connect ultracold atoms to nuclear matter [Adams et al. (2012); Bloch et al. (2012); Strinati et al. (2018)] and provide new challenges to theoretical prediction [Bruun and Smith (2007);

Taylor and Randeria (2010); Braby et al. (2010); Enss et al. (2011); Wlazłowski et al. (2012); Romatschke and Young (2013); Bluhm et al. (2017); Frank et al. (2020); Hofmann (2020); Zhou and Ma (2021)].

For a unitary Fermi gas, the second bulk viscosity vanishes, as predicted for scale-invariant systems [Son (2007); Hou et al. (2013)] and demonstrated in experiments on conformal symmetry [Elliott et al. (2014)]. Hence, in the normal phase at temperature above the superfluid transition [Ku et al. (2012)], the hydrodynamic transport properties comprise only the shear viscosity η and the thermal conductivity κ_T.

Remarkably, the measured shear viscosity and thermal conductivity in the normal phase are well fit by the simple expression [Wang et al. (2022)],

$$\eta = \frac{15}{32\sqrt{\pi}} \frac{(m k_B T)^{3/2}}{\hbar^2} + \alpha_{2\eta} \hbar n_0 \tag{1.1}$$

and

$$\kappa_T = \frac{15}{4} \frac{k_B}{m} \eta(\alpha_{2\eta} \rightarrow \alpha_{2\kappa}) \tag{1.2}$$

with k_B the Boltzmann constant and m the atom mass. The density shift coefficients $\alpha_{2\eta}$ and $\alpha_{2\kappa}$ are fit parameters. Here, the temperature T and density n_0 contributions can be understood by dimensional analysis. For the shear viscosity, with the dimension of momentum/area, we expect $\eta \propto \hbar/L^3$, with L a length scale. At high temperature, $L \rightarrow \lambda_T$, the thermal de Broglie wavelength $\propto T^{-1/2}$. At lower temperature, where the cloud is degenerate, L is roughly the inter-particle distance, i.e. $1/L^3 = n_0$. For both η and κ_T, the leading high temperature $T^{3/2}$ dependence is obtained by variational calculations for a unitary gas in the two-body Boltzmann limit [Bruun and Smith (2007); Braby et al. (2010); Bluhm et al. (2017)]. Density shifts, relative to the high temperature limits, can arise from Pauli blocking in an ideal Fermi gas, but are reduced by in medium effects in a unitary Fermi gas [Frank et al. (2020)]. In contrast to the $T^{3/2}$ coefficients, the density shift coefficients $\alpha_{2\eta}$ and $\alpha_{2\kappa}$ are unknown universal constants, which can be determined by precise measurements of the static transport properties.

The density shifts of the transport properties measured at finite frequency are sensitive to the hydrodynamic relaxation times τ_η and τ_κ. Here we need to discuss more detail about relaxation times of a system. Generally, there are two time scales related to the behavior of a many body system. The first is a microscopic time scale τ_1, such as τ_η and τ_κ. This is the time scale for the system to reach local thermal equilibrium, which should only depend on the collisional properties of the particle. The other is the macroscopic time for the conserved charges, such as mass, momentum and energy, to diffuse τ_2. Fluid dynamics is an effective

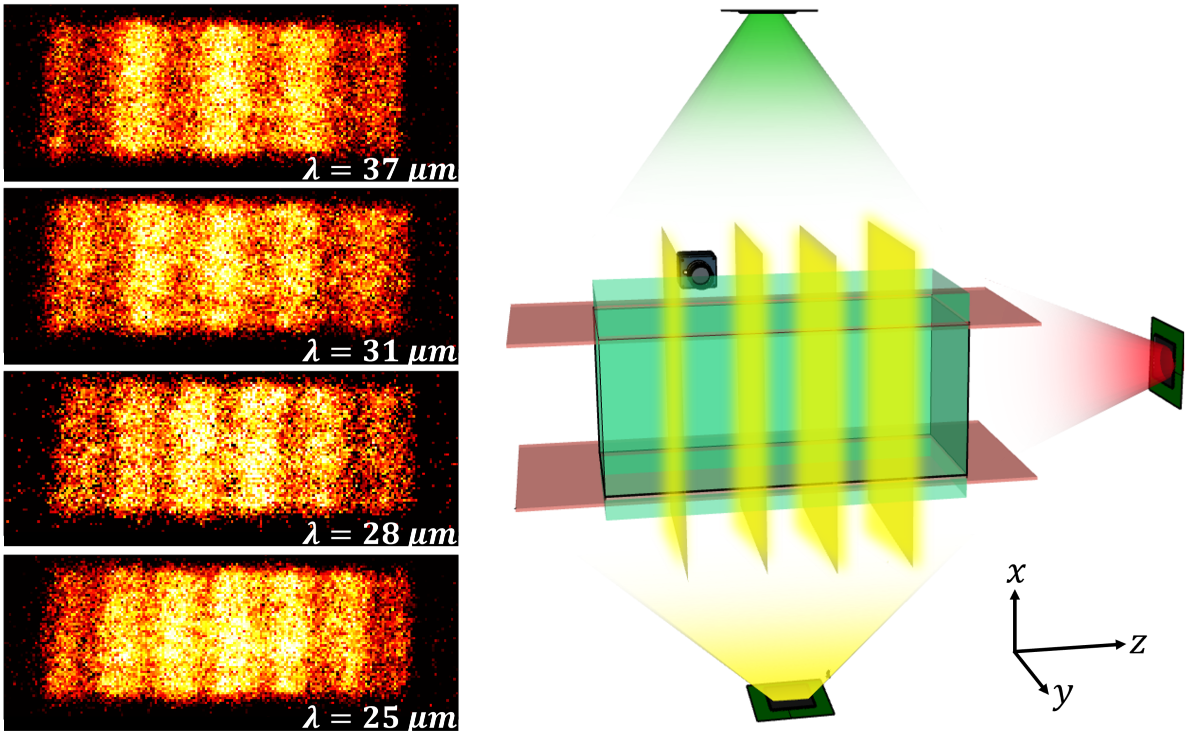

Figure 1.2: A unitary Fermi gas is loaded into a repulsive box potential created by two Digital Micromirror Devices, or DMDs (top and right). A third DMD (bottom) generates a static spatially periodic perturbation $\delta U(z)$ with an adjustable wavelength λ, creating a spatially periodic initial 1D density profiles (left). After δU is abruptly extinguished, the dominant Fourier component exhibits an oscillatory decay.

theory, technically it applies to any many-body system as long as $\tau_1 \ll \tau_2$[1].

In this dissertation, I present our work, which determines the universal density shift coefficients for both shear viscosity and thermal conductivity of a normal phase unitary Fermi gas trapped in an optical box potential. This work reports the first measurements of these next order pure density dependent terms for the transport properties.

We realize an ultracold (about 100 nK), near-homogeneous gas of strongly interacting ^{6}Li atoms, confined in a repulsive box potential. The optical box is created by two Digital Micromirror Devices (DMD). Figure 1.2 shows a schematic setup of our box beam. The top and right side DMD create the six box sheets (green and red light). Previously we used the top DMD to create the perturbing potential to probe the gas simultaneously [Baird (2019); Wang et al. (2022)]. For the experiment discussed in this dissertation, we upgraded our optical box system by implementing a third DMD, the bottom one with yellow beam, to independently project a static repulsive potential δU that spatially varies with an adjustable amplitude and wavelength λ along axial direction z. After reaching thermal equilibrium, the gas exhibits a spatially periodic density variation. The third DMD is illuminated with a low intensity beam to utilize its full dynamic range. Left side of Figure 1.2 are absorption images of atom cloud with four different periodic density variation, created by the third DMD.

The perturbation beam is then abruptly extinguished, causing an oscillatory decay of the measured density perturbation $\delta n(z,t) = n(z,t) - n_0$, with $n(z,t)$ the doubly integrated 3D density. We measure the free decay of the density profile by performing a Fast Fourier transform (FFT), then observing the time evolution of the dominant Fourier component. In previous work [Wang et al. (2022)], we used a hydrodynamic linear response model that assumed a fast relaxation, i.e. $\tau_\eta = \tau_\kappa = 0$. The measured shear viscosity and thermal conductivity were not their static values, we were unable to determine the universal density shift coefficients. In this work, in order to determine the static transport properties, we explicitly include the finite relaxation times in our model. We developed a kinetic relaxation model in the linear response regime by constructing four coupled equations: two describe the changes in the density $\delta n(z,t)$ and temperature $\delta T(z,t)$, and two describe the relaxation of the viscous force and heat current [Braby et al. (2010, 2011)]. Figure 1.3 shows a typical oscillation data (blue) we obtained , red solid curve is fitting to the new kinetic relaxation model.

We show that time-domain hydrodynamic relaxation experiments are well-suited to kinetic theory models that explicitly include the transport relaxation times for the viscous force and heat current, which are driven at the frequency and damping rate of the first sound mode and at the thermal decay rate of the thermally diffusive mode. Using this method, we obtain the static shear viscosity, thermal conductivity, and corresponding density shift coefficients,

---

[1] We can say that if the observation time is long enough, any system should behave like fluid.

relative to the high temperature limits, for a normal-phase unitary Fermi gas in a box potential.

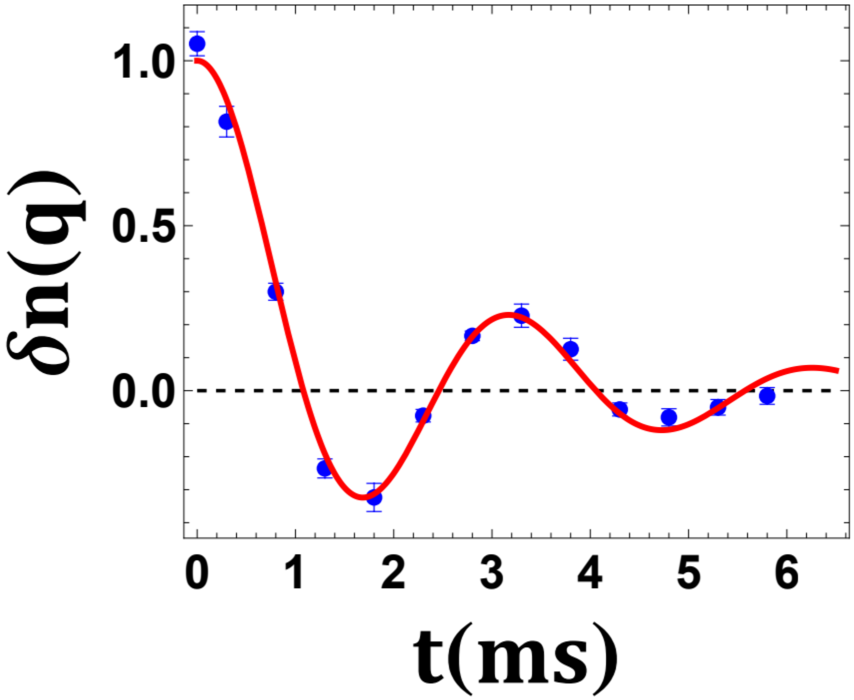

Figure 1.3: Relaxation model fit for $T/T_F \simeq 0.37$, perturbation wavelength $\lambda \simeq 37.0$ μm. Data (blue dots), model (red solid curve).

CHAPTER

2

SCATTERING PHYSICS AND FESHBACH RESONANCE

In this chapter,we briefly introduce the properties of ultracold Fermi gas of ^{6}Li with tunable interaction. We start with a general introduction of scattering physics, since this forms the basis for all the effects we want to study. Then we will provide a detailed description of Feshbach resonance, which is the main tool used in tuning the scattering properties of our sample.

2.1 Scattering theory

The topic of scattering problems can be found in any quantum mechanics textbook. Here we only cover the basis of it and the important results we need, detail introduction can be found in [Shankar (2012),Sakurai and Commins (1995)]

The problem we want to solve involves two atoms scattering against each other. We assume the interaction potential is a function that only depends on the distance between the two atoms $V(|\mathbf{r_1}-\mathbf{r_2}|)$. The time-independent Schrodinger's equation takes the form $\mathbf{H}\psi=\mathbf{E}\psi$ with the Hamiltonian $\mathbf{H}=\frac{P^2}{2\mu}+V(r)$, where $\mu=\frac{m_1 m_2}{m_1+m_2}$ is the reduced mass, m_1, m_2 are the mass of two atoms. Substituting these into the time-independent Schrodinger's equation, we obtain:

$$\nabla^2\psi + (k^2 - V(r))\psi = 0, \tag{2.1}$$

where $k = \sqrt{2\mu E}/\hbar$ is the associated wave vector. Solving the scattering problem equals to solving this equation. In actual experiment, measurements are taken at distance far away from scattering center, therefore we only need to find the form of ψ as $r \to \infty$.

The general form of a wavefunction undergoing scattering, written in spherical coordinates,is given by,

$$\psi(r,\theta) = e^{ikz} + f(\theta,k)\frac{e^{ikr}}{r}. \tag{2.2}$$

Here we define z-axis as the wave propagating direction, the wavefunction therefore has azimuthal symmetry. The first term represents the incoming wave, while the second term represents the scattering wave at large distance. $f(\theta,k)$ denotes the scattering amplitude. $f = 0$ if no scattering occurs. Integrating $|f|^2$ over a sphere gives a measure of the scattering strength, also known as scattering cross section σ_c,

$$\frac{d\sigma_c}{d\Omega} = |f(\theta,k)|^2. \tag{2.3}$$

As the scattering potential provided by the target is spherically symmetric, we can expand the scattering wave in partial waves as

$$f(\theta,k) = \sum_{l=0}(2l+1)f_l(k)P_l(cos\theta), \tag{2.4}$$

Here, l indicates the order of the angular momentum of outgoing wave and P_l are Legendre polynomials. The partial wave amplitude $f_l(k)$is related to the scattering phase shift δ_l by

$$f_l(k) = \frac{\exp(i\delta_l)\sin\delta_l}{k}. \tag{2.5}$$

The total scattering cross section can be obtained as:

$$\sigma_c = \frac{4\pi}{k^2}\sum_{l=0}(2l+1)\sin^2\delta_l. \tag{2.6}$$

Remember we are dealing with ultracold gases, the temperature is often 1μK or lower, corresponding to a thermal de Broglie wavelength $\lambda_{th} = h/\sqrt{2\pi m k_B T} \approx 700nm$. This corresponds to a linear momentum $p_{max} = h/\lambda_{th} = 9.5\times10^{-28}$m/s. Furthermore, if we consider an interparticle potential with an effective range $r_0 = 20a_0$,where a_0 is the Bohr radius, a reasonable approximation for the triplet potential that dominates the interaction of the particles, then the maximum quantized angular momentum l_{max} can be estimated as:

$$\hbar l_{max} = r_0 p_{max} \Longrightarrow l_{max} = \frac{2\pi r_0}{\lambda_{dB}} \approx 0.001. \tag{2.7}$$

Since l must be a nonnegative value, we are left with $l = 0$. Therefore at ultracold temperature, only s-wave scattering is permitted. Under this condition, Eq. 2.6 reduces to

$$\sigma_c = \frac{4\pi}{k^2} \sin^2 \delta_0. \tag{2.8}$$

Therefore we only need to calculate s-wave phase shift δ_0.

Now, we need to introduce an important quantity , the s-wave scattering length a_s, which is defined [Shankar (2012)]by:

$$a_s \equiv -\lim_{k\to 0} \frac{\tan \delta_0}{k}. \tag{2.9}$$

Then we can write the s-wave cross section in terms of s-wave scattering length a_s and incident wave vector k as

$$\sigma_c = \frac{4\pi a_s^2}{1 + k^2 a_s^2}. \tag{2.10}$$

As we stated before, the momentum we are dealing with is negligibly small. When $k a_s \to 0$, we have

$$\sigma_c \approx 4\pi a_s^2. \tag{2.11}$$

Eq. 2.11 provides some important information because the cross section can be understood as a crude characterisation of the scattering power of the potential. For low-energy scattering process, it can be effectively parameterized by a single quantity, a_s. when $|a_s|$ is large, the interaction between scattering atoms is strong. On the other hand, small $|a_s|$ corresponds to weak interaction. Furthermore, $a_s > 0$ indicates repulsive interaction , while $a_s < 0$ indicates attractive interaction .

Last but not the least, remember the wave function is a two-particle wave function. For identical particles, it has to be symmetric for bosons and anti-symmetric for fermions. However, the spatial part of s-wave collision is symmetric, so an ultracold Fermi gas is entirely collisionless unless two different spin states are trapped. In the experiment, we trap the two lowest hyperfine ground states of ^{6}Li, labeled as $|1\rangle, |2\rangle$, or as spin-up and spin down. Detail electronic structure of ^{6}Li is covered below. Control of these internal spin states are accomplished by applying radio-frequency pulse.

2.2 Electronic structure of ^{6}Li

In this section we cover the detail of the electronic structure of ^{6}Li, focusing on the two-component Fermi system used in our lab. The ^{6}Li atom is composed of 3 protons, 3 neutrons, and 3 electrons. The nuclear ground state has nuclear spin of $I = 1$, while the electronic ground state consists of 2 electrons in 1s orbital and 1 unpaired electron in 2s orbital. The unpaired electron in the valence band is the only electron of interest. For the ground state , the orbital angular momentum quantum number is $L = 0$, the spin quantum number is $s = 1/2$, and the total angular momentum F, which includes contributions from nuclear, orbital, and electron spin,can have two possible values, $F = 1/2, F = 3/2$. Therefore, the possible spin projection for $F = 1/2$ are $m_F = \pm 1/2$,and for $F = 3/2$ are $m_F = \pm 1/2, \pm 3/2$. The presence of a magnetic field lifts the degeneracy. The Hamiltonian we wish to solve is given by

$$H_i = \frac{a_{hf}}{\hbar^2}\mathbf{S}\cdot\mathbf{I} + \frac{\mu_B}{\hbar}(g_J\mathbf{S} + g_I\mathbf{I})\cdot\mathbf{B}, \tag{2.12}$$

where a_{hf} is the hyperfine constant, g_J is the electronic g-factor for ^{6}Li ground state, g_I is the nuclear g-factor, μ_B is the Bohr magnetton, $\mathbf{B}$ is the external magnetic field. The eigenstates of Eq.2.12, written in the basis of electron spin projectionm_s and nuclear spin projection m_I, $|m_s, m_I\rangle$, are[Houbiers et al. (1998)]:

$$|1\rangle = \sin\Theta_+|\frac{1}{2}, 0\rangle - \cos\Theta_+|-\frac{1}{2}, 1\rangle \tag{2.13}$$

$$|2\rangle = \sin\Theta_-|\frac{1}{2}, -1\rangle - \cos\Theta_-|-\frac{1}{2}, 0\rangle \tag{2.14}$$

$$|3\rangle = |-\frac{1}{2}, -1\rangle \tag{2.15}$$

$$|4\rangle = \cos\Theta_-|\frac{1}{2}, -1\rangle + \sin\Theta_-|-\frac{1}{2}, 0\rangle \tag{2.16}$$

$$|5\rangle = \cos\Theta_+|\frac{1}{2}, 0\rangle + \sin\Theta_+|-\frac{1}{2}, 1\rangle \tag{2.17}$$

$$|6\rangle = |\frac{1}{2}, 1\rangle \tag{2.18}$$

The above hyperfine states are labeled by increasing energy, with $|1\rangle$ being the lowest energy state and $|6\rangle$ is the highest. The coefficients in Eq.2.13 through Eq.2.18 are dependent on magnetic field.

The energy eigenvalues associated with eigenstates $|n\rangle$ are:

$$E_1 = -\frac{1}{4}(a_{hf} - 2g_I\mu_B B + 2a_{hf}R_+) \tag{2.19}$$

$$E_2 = -\frac{1}{4}(a_{hf} + 2g_I\mu_B B + 2a_{hf}R_-) \tag{2.20}$$

$$E_3 = \frac{a_{hf}}{2} - \frac{\mu_B B}{2}(2g_I + g_J) \tag{2.21}$$

$$E_4 = \frac{1}{4}(-a_{hf} - 2g_I\mu_B B + 2a_{hf}R_-) \tag{2.22}$$

$$E_5 = \frac{1}{4}(-a_{hf} + 2g_I\mu_B B + 2a_{hf}R_+) \tag{2.23}$$

$$E_6 = \frac{a_{hf}}{2} + \frac{\mu_B B}{2}(2g_I + g_J) \tag{2.24}$$

$\sin\Theta_\pm, \cos\Theta_\pm, R_\pm$ are coefficients dependent on B [Zhang (2012)]. We can plot the energy eighenvalues as a function of magnetic field shown in figure.2.1

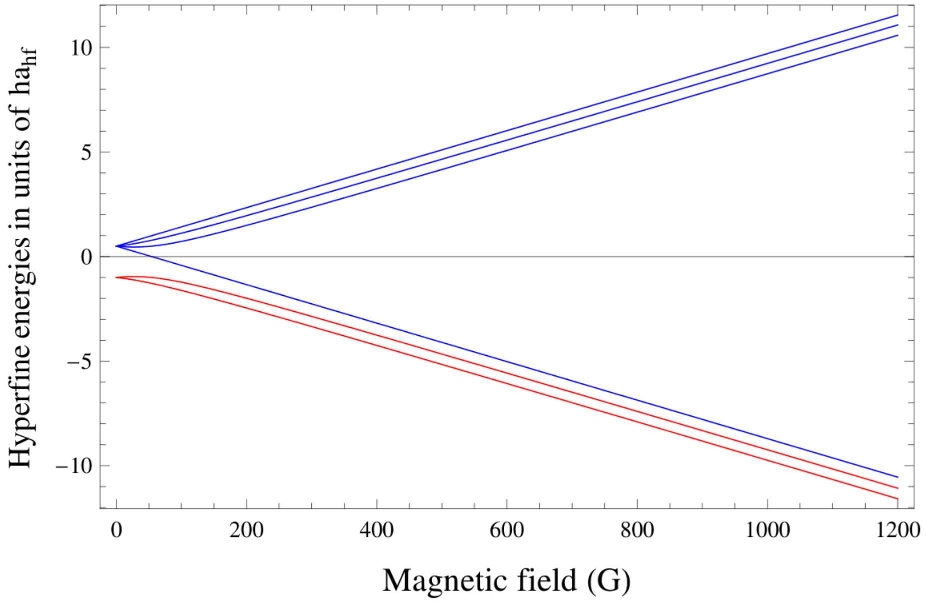

Figure 2.1: Hyperfine ground state structure of ^{6}Li plotted in units of ha_{hf} versus magnetic field in gauss. The two red curves are states $|1\rangle, |2\rangle$.

We can see in Figure. 2.1 that as the magnetic field increases, the original degenerate states for $F = 1/2, F = 3/2$ split into six different states. At high field, the hyperfine energy shifts are almost linear with magnetic field (about -1.4MHz/G for lowest three states).

2.3 Feshbach resonance and BEC-BCS crossover

With the material we have introduced so far, we can now introduce the concept of Feshbach resonance. Consider two ^{6}Li atoms, one in state $|1\rangle$ and one in state $|2\rangle$. If they are far apart from each other , the two atoms can be treated as independent particles, and there is no restriction on the wavefunction since their wavefunction hardly overlap. However, during the scattering process, the two atoms approach each other sufficiently so that their wavefunctions start to overlap, this is when the quantum nature starts to play its role. Quantum mechanics calls for a different treatment of the electrons, where we sum their spins, leading to singlet and a triplet state. Therefore, we introduce two different interaction potentials between the two atoms: one for the singlet, one for the triplet state, which correspond to the antisymmetric and symmetric spin-wavefunctions, respectively. The two potentials coincide at large distances since the individual wavefunction hardly overlap.

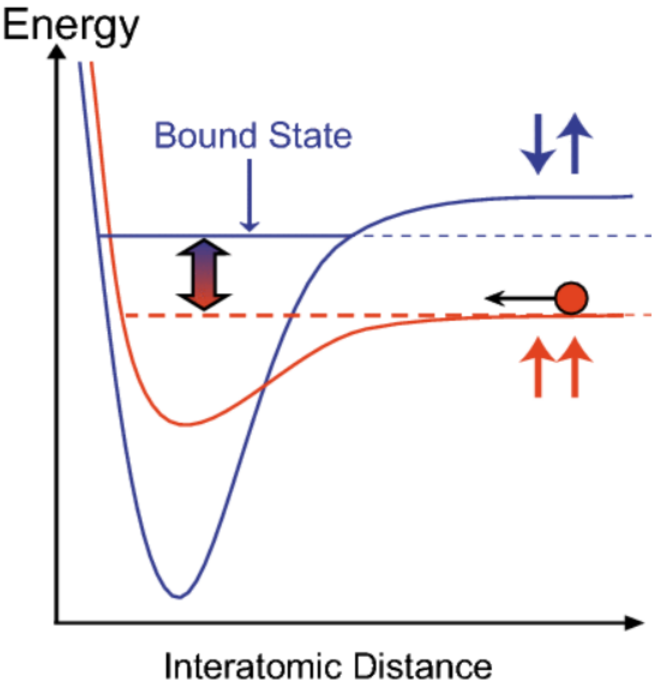

Figure 2.2: Triplet(red curve) and Singlet(blue curve) potentials involved in ^{6}Li Feshbach resonance, figure adopted from [Ketterle and Zwierlein (2008)].

In typical experiments, the magnetic field are larger than 500G, in such high field, the valence electron in ^{6}Li atom will be fully polarized for both states. This can also be observed from the eigenstate wavefunction of state $|1\rangle$ and $|2\rangle$, namely Eq. 2.13 and Eq.2.14. For large **B**, $\sin\Theta_\pm$ are negligible, therefore

$$|1\rangle \to -|-\frac{1}{2},1\rangle \tag{2.25}$$

$$|2\rangle \to -|-\frac{1}{2},0\rangle \tag{2.26}$$

Both states have electron spin $m_s = -\frac{1}{2}$. The two scattering atoms are in triplet potential, but they still have different nuclear spin. This gives a total spin $F = m_s + m_I = \pm\frac{1}{2}$, which represent our spin-up and spin-down atoms,repectively. Figure.2.2 shows the triplet $V_T(r)$ and singlet potential$V_S(r)$ of two colliding atoms as function of interparticle distance. We refer to the triplet configuration as open channel since the atoms are in triplet state, and the singlet configuration as closed channel. The singlet state has a total electron spin $S = 0$, and only triplet state has a nonvanishing Magnetic quantum number $M_s \neq 0$. Therefore, only triplet state can couple to magnetic field.

If there is no coupling between V_T and V_S, then the two atoms would simply scatter off each other in V_T, acquiring some fixed phase shift. However, V_T and V_S are coupled through hyperfine interaction V_{hf} between electrons and nucleons. To see this, recall from the text book that V_{hf} is given by $V_{hf} = a_{hf}\mathbf{s_1}\cdot\mathbf{i_1}$, $\mathbf{s_1}$ and $\mathbf{i_1}$ are electron spin and nuclear spin for one atom, then the total hyperfine interaction between the two atoms are[Ketterle and Zwierlein (2008)]

$$V_{hf} = V_{hf1} + V_{hf2} = a_{hf}(\mathbf{s_1}\cdot\mathbf{i_1} + \mathbf{s_2}\cdot\mathbf{i_2}) \tag{2.27}$$

$$= \frac{a_{hf}}{2}\mathbf{S}\cdot(\mathbf{i_1}+\mathbf{i_2}) + \frac{a_{hf}}{2}(\mathbf{s_1}-\mathbf{s_2})\cdot(\mathbf{i_1}-\mathbf{i_2}), \tag{2.28}$$

V_{hf} is not diagonal in the total electron spin $\mathbf{S} = \mathbf{s_1} + \mathbf{s_2}$ of the two atoms. The second term in Eq.2.28 connects singlet and triplet states since $\mathbf{s_1} - \mathbf{s_2}$ is antisymmetric in 1 and 2, therefore coupling triplet state and singlet state. Thus, V_{hf} is totally off-diagonal in triplet and singlet basis, the off-diagonal element describes the coupling of two states.

The singlet potential contains a bound state that is close to the dissociation limit. By applying an external magnetic field , we can shift down the triplet channel relative to singlet channel until the continuum is at the same level as the weakly bound state in singlet channel. The existence of a bound state close to the dissociation limit greatly changes the scattering length of the atoms. Theoretically, we have a bound state coupled to a continuum scattering states. This was treated independently in nuclear physics by Feshbach[Feshbach (1958)] and in atomic physics by Fano[Fano (1961)], and is well-known in cold atom community as Fano-Feshbach resonance, or simply Feshbach resonance.

At Feshbach resonance, the s-wave scattering length diverges, $a_s \to \infty$. Referring back on Eq.2.10, this implies that

$$\sigma_c = \lim_{a_s \to \infty} \frac{4\pi a_s^2}{1 + k^2 a_s^2} = \frac{4\pi}{k^2}. \tag{2.29}$$

Here, k is on the order of Fermi wave vector k_F, which only depends on the density of the gas. This suggests that the scattering properties of the system become independent of the sign, strength, or any detailed structure of the interparticle interaction. In this situation , the gas is called unitary Fermi gas. Figure.2.3 shows the s-wave scattering length (i.e. the interaction strength) of state $|1\rangle, |2\rangle$ of ^{6}Li atoms as a function of external magnetic field near Feshbach resonance.

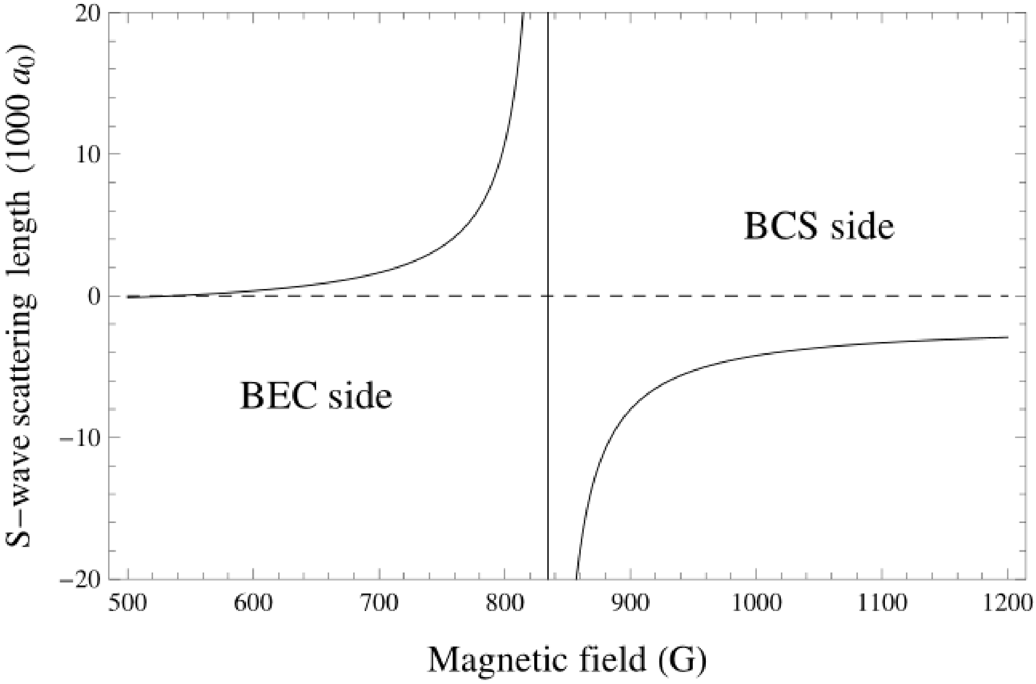

Figure 2.3: s-wave scattering length vs external magnetic field for ^{6}Li state $|1\rangle, |2\rangle$

Atomic physics would not be the same without Feshbach resonance, we are now able to control the interaction by simply tuning the external magnetic field. For the states $|1\rangle, |2\rangle$ of ^{6}Li, Feshbach resonance occurs at $B \approx 832$G as shown in Figure.2.3. On the left side of the resonance, $a_s > 0$, interaction is repulsive, the energy of the triplet state is still above the singlet bound state, atoms therefore tend to fall into the bound state and form stable molecules, Bose-Einstein condensate (BEC) can form at ultracold temperature. This side is called the BEC side. On the other side of the resonance , where $a_s < 0$, interaction is attractive. The Energy of the triplet state is lower than the singlet bound state, allowing atoms to form weakly bound Cooper pairs at low temperature and turn into a superfluid. This side of resonance is called the BCS side. The entrie region across the Feshbach resonance is known as BEC-BCS crossover. In fact, by tuning the interaction strength between two fermionic spin states, one can smoothly cross over from a regime of tightly bound molecules to a regime of long range Cooper pairs, whose characteristic size is much larger than the interparticle spacing. In the middle, we have a new type of superfluidity, where the pair size is comparable to interparticle spacing.

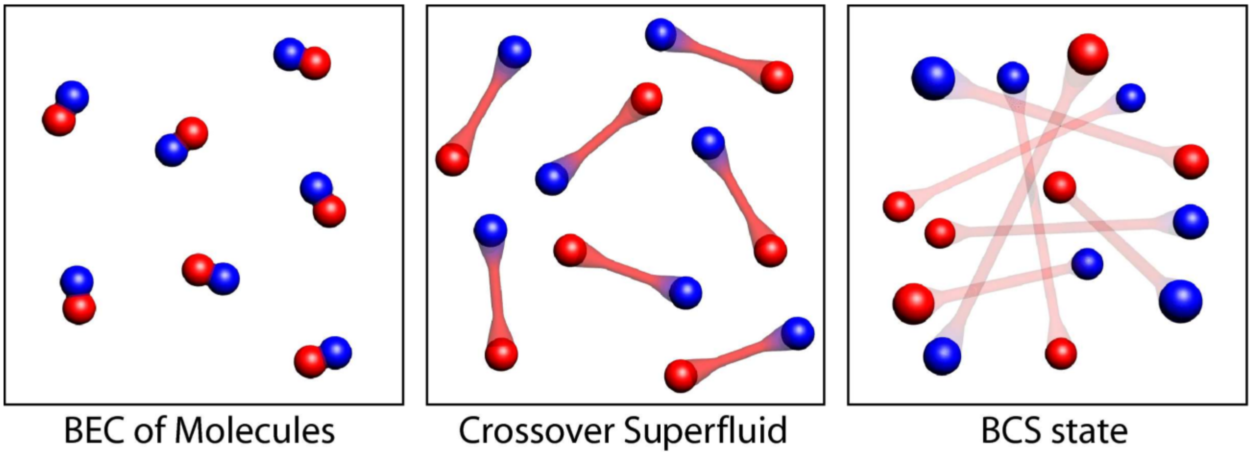

Figure 2.4: Atom pairs in the BEC-BCS crossover, figure adopted from [Ketterle and Zwierlein (2008)].

CHAPTER

3

EXPERIMENTAL SETUP

This chapter introduces our experimental setup for trapping and cooling ^{6}Li atoms, specifically highlighting the innovative use of Digital Micro-Mirror Devices (DMDs) to create a versatile box potential and manipulate ultracold atomic gases. Our apparatus consist of a high vaccum chamber featuring the lithium source, Zeeman slower, a magnet system providing high magnetic field surrounding the chamber, a Coherent 899 ring dye laser for lasering cooling and imaging, two CCD cameras, a high power CO_2 laser for evaporative cooling, three DMDs for creating box potential and perturbation, and all other associated optics. Comprehensive details of our trapping and cooling techniques can be found in previous students' theses [Kinast (2006); Elliott (2014)], this chapter provides a concise summary of our standard techniques and focuses on the upgrade of our box potential-the additional DMD and associated optics that we added for creating an independent controlled perturbation inside the box.

3.1 Optical cooling and trapping

3.1.1 Zeeman slower

For daily experiment, it starts with heating up the lithium sample in the oven region. Typically when temperature reaches 395^0C, the lithium sample is adequately vaporized. As atoms exit the oven region, they attain speeds of approximately 2 km/s, which is too fast to be captured by the Magneto-optical trap(MOT) in the main chamber. Therefore the first stage of cooling is provided by a Zeeman slower. The slower is composed of several wire coils coaxial with the slowing beam direction, creating a spatially varying bias magnetic field. Upon entering the slower, the motion of atoms is impeded by a slowing beam ,which is red-detuned from the D_2 transition of ^{6}Li by roughly 200 MHz. The velocity of atomic beam and slowing beam are counterpropagating, causing a Doppler shift that brings a portion of the atoms close to resonance with slowing beam. Atoms therefore absorb counterpropagating photons and then emit photons in random directions. The net result is slowing down of atom speed. The tapered bias field shifts the energy level of atoms, making sure atoms remain resonant with the Doppler-shifted slowing beam as they travel along the slower. Upon exiting the slower, atom speed drops to approximately 30 m/s, which is sufficiently slow for them to be captured by the MOT.

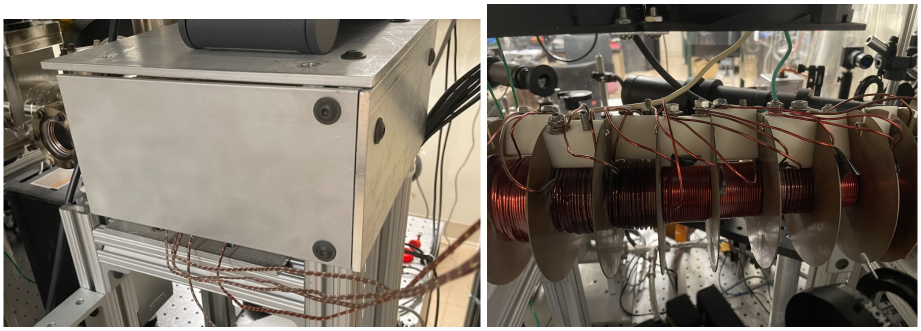

Figure 3.1: Left: ^{6}Li oven. Right: Zeeman slower

3.1.2 Magneto-optical trap(MOT)

When atoms enter the main vacuum chamber, they undergo trapping and cooling through the interaction with three pairs of retroreflected, mutually orthogonal, red-detuned laser beams. These beams are carefully arranged to intersect near the zero point of a quadrupole magnetic field, forming what is known as a Magneto-Optical Trap (MOT). The laser beams employed in the MOT are generated by a Coherent 899 ring dye laser, which is pumped by a Verdi-12 solid-state laser, alongside standard frequency stabilization techniques. The wavelength of these beams is finely tuned to the D_2 transition,as illustrated in Fig 3.2, resonating near 670.79 nm with FWHM of 5.9 MHz.

The cooling mechanism of the Magneto-Optical Trap(MOT) comprises two parts: velocity-dependent radiation pressure and spatially-dependent radiation pressure. We are going to

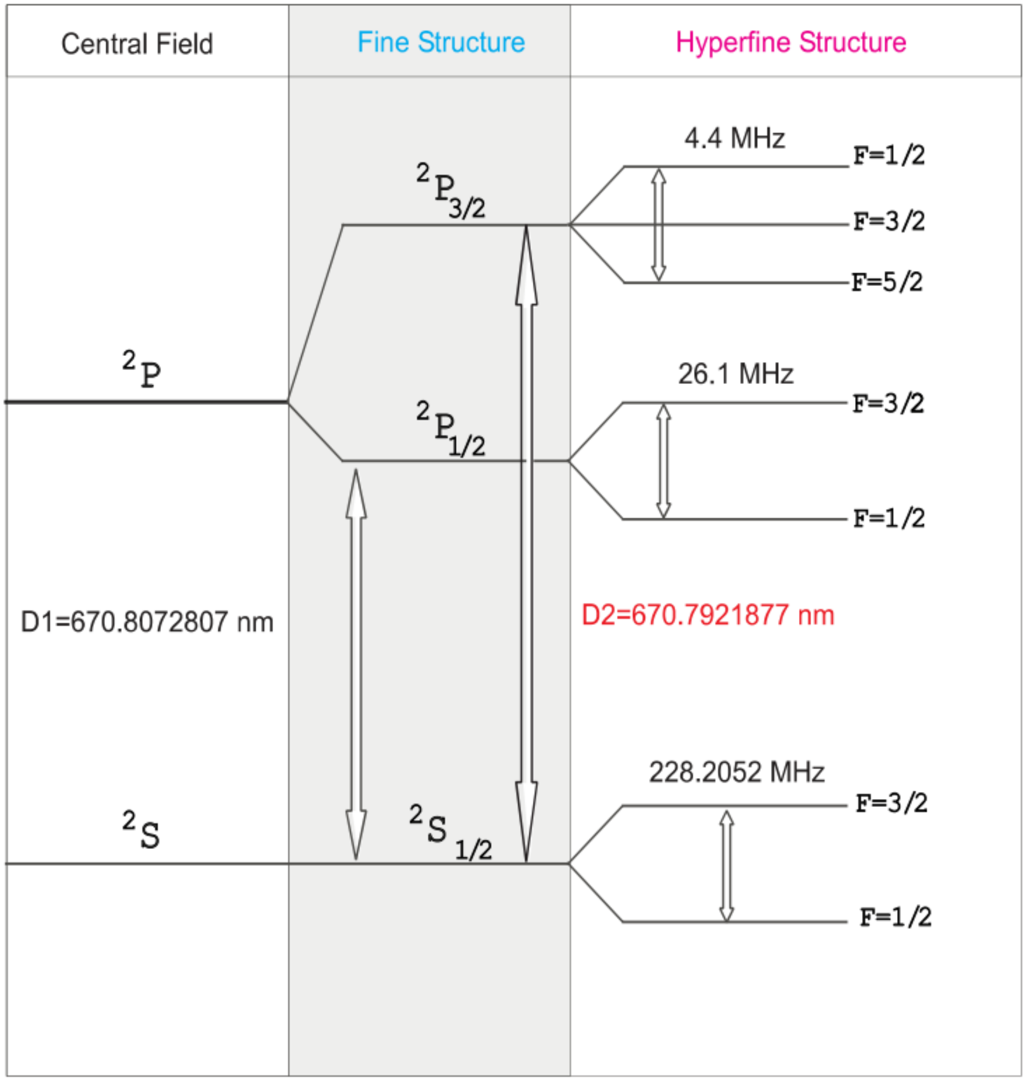

Figure 3.2: Fine structure and hyperfine structure of ^{6}Li.

discuss the velocity -dependent part first. Consider an atom with a simple two level transition frequency ω_a moving from right to left, illuminated by a counterpropagating laser beams composed of photons with a frequency ω_p that is red-detuned from atomic transition, $\omega_p < \omega_a$, as illustrated in Figure 3.3. As the atom moves, the laser beam approaching from the left undergoes a Doppler shift toward resonance with the atomic transition, while the beam approaching from the right experiences a Doppler shift further away from resonance. Consequently, the atom is more likely to absorb photons from the beam propagating from left to right, opposite to its velocity direction, resulting in a reduction of the atom's momentum in that direction. This one-dimensional illustration can be extended to three dimensions, involving three pairs of mutually orthogonal, counterpropagating, red-detuned laser beams. This optical aspect of the MOT constrains atoms in momentum space without spatial confinement. To achieve spatial confinement, the magnetic component is required.

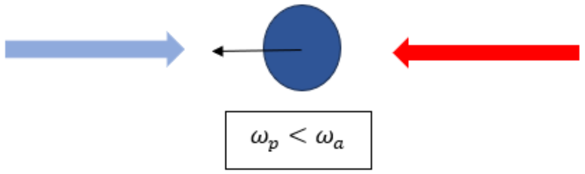

Figure 3.3: Illustration of Doppler cooling. Laser frequency is smaller than atomic transition frequency, $\omega_p < \omega_a$. Atom moving from right to left , photons propagating from left to right is Doppler shifted towards ω_a, photons propagating from right to left are Doppler shifted away from ω_a, therefore atom is more likely to absorb photons travelling from left to right, reducing its momentum. Same principle applies to atoms travelling from left to right.

To elucidate the achievement of spatial confinement, consider an atom with a ground state total angular momentum $F = 0$ and an excited state with total angular momentum is $F' = 1$. For ground state, $m_F = 0$, while for excited state, $m'_F = 0, \pm 1$. A spatially varying magnetic field will induces a spatially dependent energy shift, or Zeeman shift, for the $m'_F = \pm 1$ excited sublevels of ^{6}Li atom. Figure 3.4 shows how the energy tuning of magnetic field sublevels in the ground and excited states varies with dimension x. The laser frequency is slighted red-shifted relative to the atomic transition from $F = 0$ to $F' = 1$ at zero magnetic field by δ. Transition from ground state to excited state with $m'_F = 1$ requires absorption of σ^+-circularly polarized photons, while transition to excited state with $m'_F = -1$ requires absorption of σ^- -circularly polarized photons. Now consider an atom move freely in a magnetic field increasing linearly in the positive direction about a zero point $x = 0$. If we arrange our beams such that σ^-

polarized light travelling from right to left, σ^+ polarized light travelling from left to right. The laser frequency is red-detuned with respect to atomic transition from $F = 0$ to $F' = 1$, then an atom in regions of negative magnetic field is more likely to absorb σ^+ photon, likewise an atom in regions of positive magnetic field is more likely to absorb σ^- photon. The net result is that the atom will move toward the zero point. For small displacement about $x = 0$, this restoring force is linear. Again, this 1D case can be generalized to 3D, together with the momentum damping.

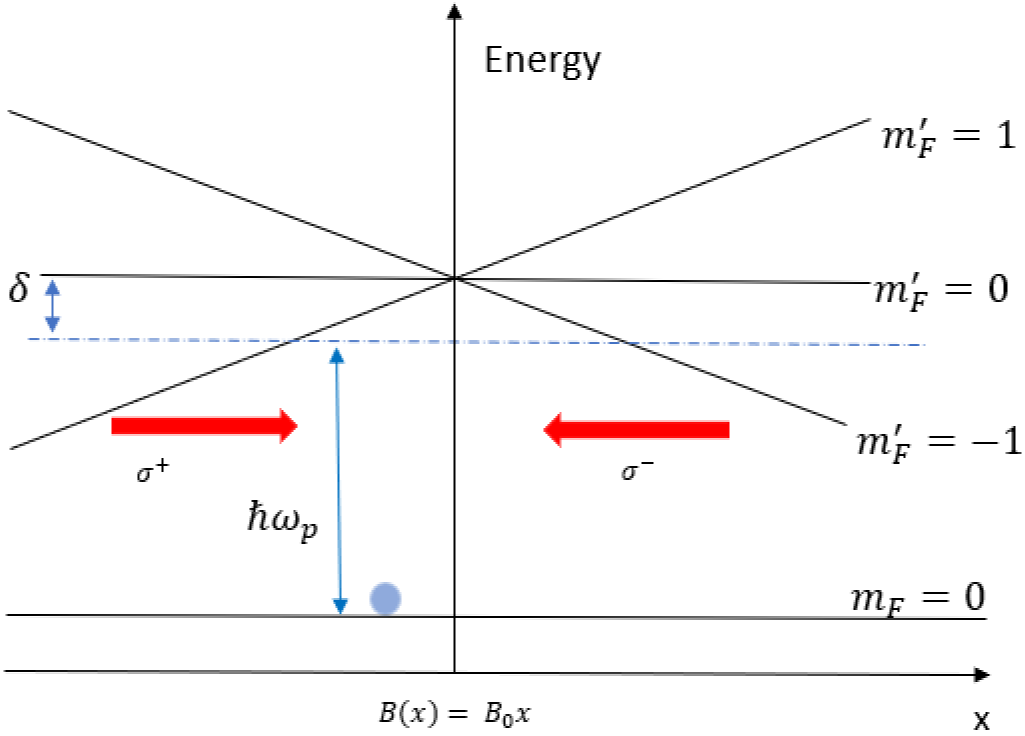

Figure 3.4: The spatial restoring force of MOT arises from preferential absorption of photons with a particular polarization based on atom's position. ω_p is laser frequency, it is red-shifted δ relative to atomic transition frequency. In the figure atom is on the $x < 0$ part, it is more likely to absorb photons with σ^+ polarization since this transition is Zeeman shifted toward resonance, atom is pushed toward $x = 0$. When atom wanders toward $x > 0$, it is more likely to absorb σ^- photon, again pushed toward $x = 0$.

The frequency of the MOT beam primarily corresponds to the transition from $F = 3/2$ ground state to the excited state,as illustrated in Figure 3.2. However, upon exiting the Zeeman slower, atoms populate both $F = 1/2$ and $F = 3/2$ ground states. The $F = 1/2$ ground state is about 228 MHz lower than $F = 3/2$ state. To effectively cool down atoms in both states, an

Acoustic-Optical Modulator is employed to generate an additional 'repumper' beam, corresponding to the transition from the $F = 1/2$ ground state to the excited state. These repumper beams are then combined with the MOT beams before entering the vacuum chamber. The power ratio of the MOT beam to the repumper beam is set to 3:1 based on experience for best cooling performance.Figure 3.6 is the schematic setup of the MOT around the vacuum chamber, inset shows the fluorescence of atom cloud trapped in the MOT.

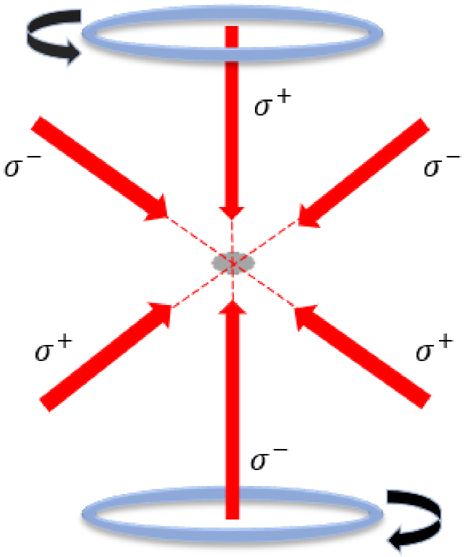

Figure 3.5: The Magneto-Optical Trap(MOT) configuration. Three pairs of mutually orthogonal, counter propagating, red-shifted, fix polarized laser beam and the quadrupole magnetic field generated by two Anti-Helmholtz coils.

Despite the success of laser cooling and trapping in MOT, there are limitations on how cold this method can reach. These techniques rely on atoms constantly absorbing and re-emitting photons. Trapped atoms therefore experience small, random momentum transfers that fundamentally restrict how low a temperature can be reached. This lower bound is given by [Fox (2006)]

$$T_{limit} = \frac{\hbar\Gamma}{2k_B}, \tag{3.1}$$

where Γ is the linewidth of the relevant optical transition. For ^{6}Li, this yields $T_{limit} \approx 140\mu$K. While 140μK sounds already a very low temperature, it is still many orders of magnitude above the temperature to reach quantum degeneracy. Therefore, we require a second stage of cooling, known as evaporative cooling, which does not involve absorption and emission of photons.

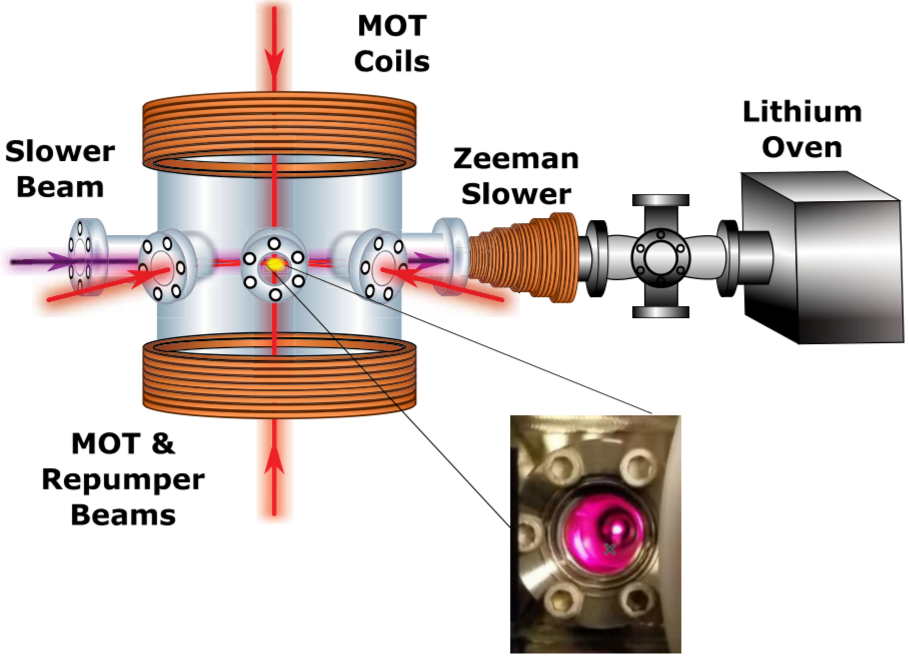

Figure 3.6: Schematics of the setup of MOT,along with Zeeman slower and lithium oven. Inset shows fluorescence from atoms trapped in the MOT.

3.2 Far Off-resonance Trap(FORT)

In our lab, evaporative cooling is conducted in a far off-resonance trap(FORT) that is produced by a Coherent GEM CO_2 laser. The output power of this laser is approximately 140 watts, operating at a wavelength of 10.6 μm. This wavelength is almost sixteen times larger than the 670.9 nm D_2 transition of ^{6}Li. As a result, the absorption rate is only 2 photons/hour.

3.2.1 Electric Dipole Force

Our CO_2 laser is positioned so that the focus of the beam overlaps with the location of ^{6}Li atoms confined in the MOT. The beam induces an electric dipole moment on the atoms. The interaction energy associated with an atom of polarizability α in the electric field **E** is given by

$$U_d = -\frac{\alpha\overline{\mathbf{E^2}}}{2}. \tag{3.2}$$

Here, the bar indicates that the field is averaged over many optical cycles. Assuming electric field is slowly varying, then $\overline{\mathbf{E^2}} = E_0^2/2$, whre E_0 is the magnitude of electric field. U_d can be expressed in terms of laser intensity I, in MKS units as

$$U_d = -\frac{1}{2\epsilon_0 c}\alpha I. \tag{3.3}$$

Here, ϵ_0 is the permittivity of free space,c is speed of light. Since ϵ_0, c, I are all positive quantities, whether the dipole potential is attractive or repulsive denpends on the sign of α. For a cylindrically symmetric system, the intensity of a focused Gaussian beam is given by[Brooker (2003)]

$$I(r,z) = \frac{I_0}{1+(z/z_0)^2}\exp\left(-\frac{2r^2}{r_0^2}\right). \tag{3.4}$$

Here, I_0 is the maximum beam intensity, $z_0 = \frac{\pi r_0^2}{\lambda}$ is the Rayleigh range, and r_0 is the $1/e^2$ intensity radius of the beam at $z = 0$. λ is the wavelength of the beam. Therefore, the dipole potential Eq.3.2 can be expressed as

$$U_d(r,z) = -\frac{U_0}{1+(z/z_0)^2}\exp\left(-\frac{2r^2}{r_0^2}\right). \tag{3.5}$$

Here, the maximum trap depth in MKS units is given by

$$U_0 = \frac{\alpha I_0}{2\epsilon_0 c}. \tag{3.6}$$

The polarizability can be written as

$$\alpha = \frac{\alpha_0 \omega_0^2}{\omega_0^2 - \omega^2} \tag{3.7}$$

α_0 is the static polarizability, ω is the laser frequency, ω_0 is the transition frequency. Notably, atoms are drawn towards regions of high intensity when exposed to red-detuned beams and repelled by blue-detuned beams. Figure.3.7 shows the geometry of the attractive dipole potential. Furthermore, due to the considerable detuning of our CO_2 beam from any considered atomic transition frequency, atoms in different quantum states undergo essentially identical forces. This aspect is particularly significant for our experiments, as we consistently confine at least two distinct hyperfine ground states of ^{6}Li. Consequently, the trapping potential generated by the CO_2 beam offers a state-independent trapping mechanism.

3.2.2 Evaporative cooling

Evaporative cooling is a very powerful cooling method to reach nano-Kelvin temperature. In fact, it is so far the only cooling method for Boson and Fermion gas to reach quantum

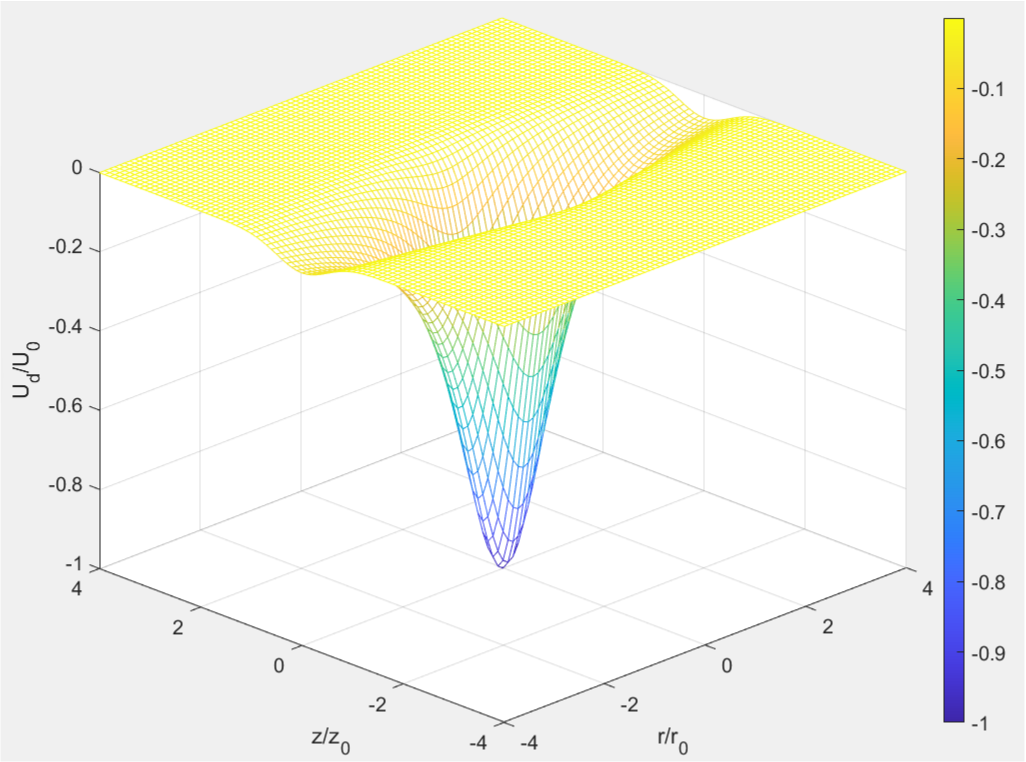

Figure 3.7: Attractive dipole potential generated by a focused laser beam propagating in z direction

degeneracy with high density[1].

The mechanism of evaporative cooling, as its name suggests, is very similar to cooling down a cup of coffee. When a cup of coffee cools, it does so because the most energetic water molecules escape. The molecules which have become steam trade some of their kinetic energy to overcome the heat of evaporation, and when they do, they can leave the cup. Because only the most energetic molecules can surmount this evaporation barrier, the atoms which leave have, on average, more energy than the atoms in the cup, and the total average energy of the tea is reduced. In the same way, we design our experiments so that the most energetic atoms will leave the trap.

At the beginning of evaporative cooling, the FORT loaded completely, the MOT beam extinguished. At this point, we have over 2 million atoms confined in the FORT. Assuming atoms equally populate state $|1\rangle$ and $|2\rangle$, then all the atoms start to collide with each other. When the trap depth is way higher than the average energy of trapped atom, the probability of an atom escaping the trap is negligible. However, if the trap depth is only a few times greater

---

[1] Recently, direct laser cooling to quantum degeneracy are achieved by several groups [Stellmer et al. (2013); Hu et al. (2017)]

than the average energy of a trapped atom, collisions between atoms result in some acquiring sufficient energy to escape the trap, while others lose energy and go into deep portion of the trap. As high-energy atoms exit the trap, those remaining are left with lower average energy. This process occurs continuously: the hottest atoms leave the trap, the remaining cooler atoms rethermalize via collision. Consequently, evaporative cooling is a cooling procedure that we sacrifices majority of hot atoms to get ultracold atoms with high phase space density.

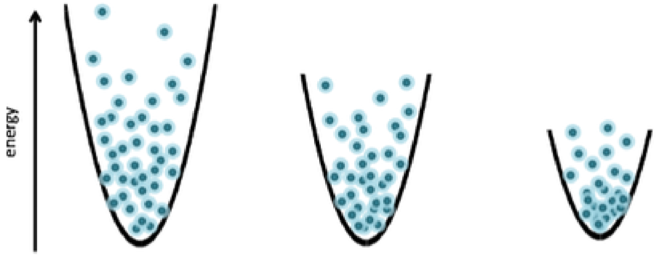

Figure 3.8: Forced evaporative cooling by lowering the trap depth, atoms with high energy continuously leave the trap.

Evaporation with trap depth hold at constant,i.e. the CO_2 laser maintaining at full power, the process is called " free evaporation." Using this method, atoms can be cooled down to 50 μK. Further cooling of the sample is achieved through "forced evaporation", wherein the trap depth is gradually reduced. This reduction is accomplished by applying a 40 MHz RF signal to an acoustic-optical modulator (AOM) placed at the output of CO_2 laser. Consequently, the output beam undergoes modulation by the RF signal. A lowering curve is sent to the function generator with user defined parameters including final trap depth and lowering time. A standard lowering curve is

$$U(t) = U_0\left(1+\frac{t}{\tau}\right)^{-1.44}. \tag{3.8}$$

By the end of the process, we are left with around 100,000 atoms in each spin state, and temperature as low as a few tens of nano-Kelvin.

3.2.3 Imaging the atoms

To image the atomic cloud, we perform absorption imaging with two CCD Andor cameras, one for horizontal imaging, the other for vertical imaging[Elliott (2014)], to image the atoms in two orthogonal directions. Approximately 1 mW of resonant light from the dye laser illuminates the atoms for about 5 μs. The atoms absorb the resonant light from the imaging pulse and prevent the light from reaching the CCD array of the Andor camera that is placed behind the atom cloud. As the size of the imaging beam is much larger than the size of the atom cloud, a shadow of the atom cloud is observed in the camera. This imaging beam completely destroys the cloud. Immediately after imaging the atoms, the camera is set to take another shot with no atoms present. We refer to the first shot with cloud shadow as signal shot, the second shot as reference shot or background shot. The image of atomic cloud can be extracted by subtracting the reference shot from signal shot.The subtracted image is further processed to extract the total atom number and the width of the atom cloud. From the total atom number and the width of the atom cloud, the temperature and the density of the atom cloud is calculated. Figure 3.9 shows the typical absorption image of forced evaporative cloud taken by horizontal CCD camera. The final trap depth is 0.18% of total CO_2 power, the cloud is around 200 μm long along axial direction. Each imaging beam is set to on-resonance with one of the two spins at magnetic field of 832G. The imaging frequency is controlled by two different AOMs. At 832G, we calculate the frequency separation between the two trapped states $|1\rangle$ and $|2\rangle$ is 76.2 MHz.

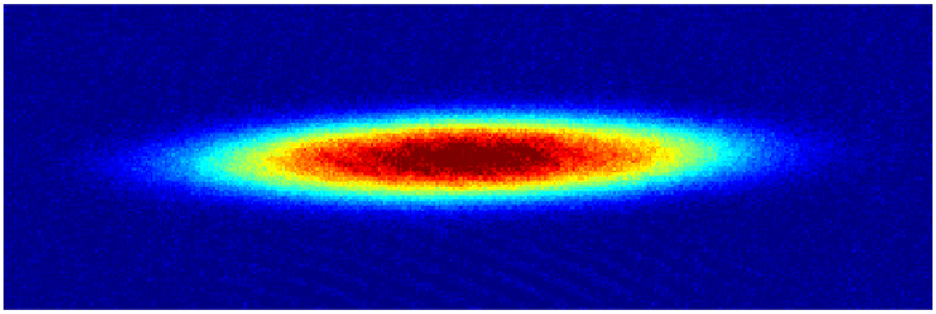

Figure 3.9: Absorption image of atomic cloud after forced evaporation to 0.18% of the maximum trap depth, the cloud is one spin of the atoms.

3.3 Optical box potential

At the end of forced evaporation, we maintain the CO_2 laser at final depth power, simultaneously we ramp up the repulsive box potential. Once the box potential reaches its maximum intensity, the FORT is turned off, allowing the atoms to be released into the box. Our Box potential are formed by 2 blue-detuned laser beams and 2 digital-micromirror devices(DMDs), along with other associated optics. One DMD produces four vertical beam sheets at a frequency of 532 nm, while the other generates two horizontal beam sheets at a frequency of 669 nm. The reason why we chose beams with different wavelengths will be addressed later. We carefully align the box to the position of the center of the magnetic bowl formed by the bias magnetic field. A schematic configuration of the box potential is depicted in Figure 3.10. From now on, we denote the DMD responsible for generating the four vertical box walls as the vertical DMD, and the one generating the two horizontal box walls as the horizontal DMD. For the experiment discussed in this dissertation, we added a third DMD which enables independent control of the perturbation used to probe the atoms. We refer to this DMD as perturbation DMD.

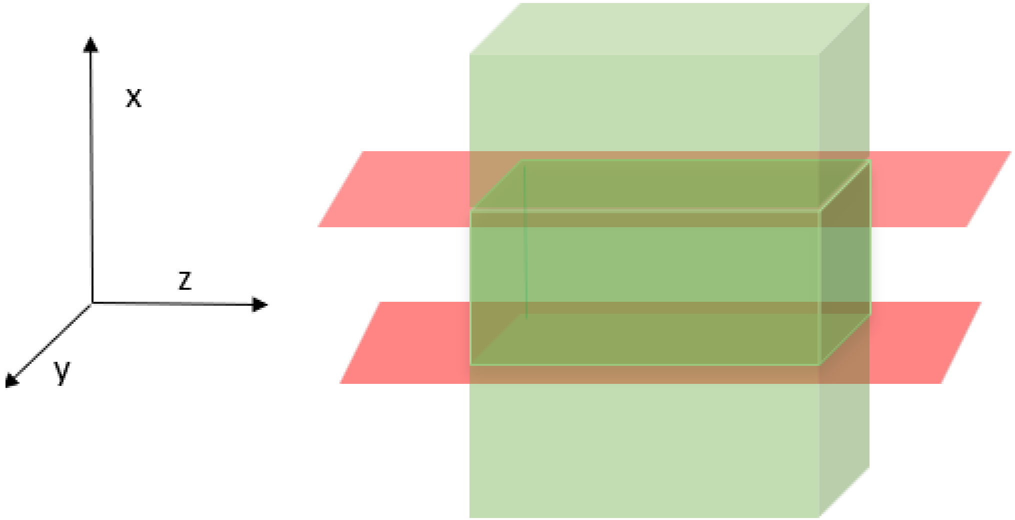

Figure 3.10: Configuration of the box potential. The box is formed by two horizontal beam sheets with wavelength 669 nm and four verical beam sheets with wavelength 532 nm.

3.3.1 Motivation for using box potential

Many previous experiments conducted by our group [Joseph et al. (2007); Cao et al. (2011); Elliott et al. (2014); Joseph et al. (2015)], which focused on studying the transport properties of unitary Fermi gas, were performed in the harmonic trap generated by the focused CO_2 laser beam. However, this method has a significant drawback: the cloud density varies from central maximum to zero at edge. As a result, the transport coefficients extracted from these experiments were always "cloud averaged" values [Joseph et al. (2015)]. This feature makes the theoretical calculation [Bluhm et al. (2017)] much more complicated. The theorists would rather have a uniform density. That's why we decided to switch to the spatial light modulation techniques. The box potential creates an almost uniform density distribution inside the trap. Although there is still variation from the center of the box to the edge due to magnetic curvature as shown in Figure 3.16, that is a considerable improvement over the harmonic trap. Box potentials have been widely adopted by research groups worldwide over the last decade to study many-body physics of quantum gas. For further details on the subject, we recommend consulting a recent review [Navon et al. (2021)].

3.3.2 Digital Micromirror Devices(DMDs)

A digital micromirror devices(DMDs) is essentially a prgrammable rectangular array of millions highly reflective aluminum micromirrors, each around 10 μm in size,capable of being individually switched 'on' or 'off' (corresponding to different tilting angles) to spatially modulate the amplitude of a beam. This enables the creation of arbitrary intensity patterns. Additionally, DMDs offer the advantage of fast full-frame refresh rates on the order of 20 kHz, approximately 20 times faster than comparable liquid crystal-based spatial light modulators (SLMs).

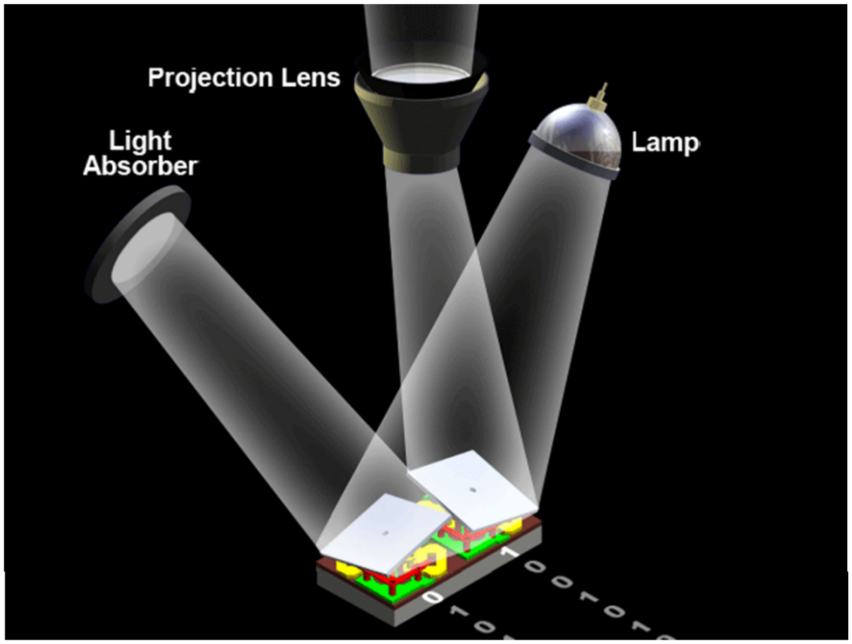

Figure 3.11: Two micromirrors, one in on state, one in off state. Figure adopted from [Lee (2008)]

The two DMDs we utilized for the horizontal box walls and perturbation are TI-DLP6500

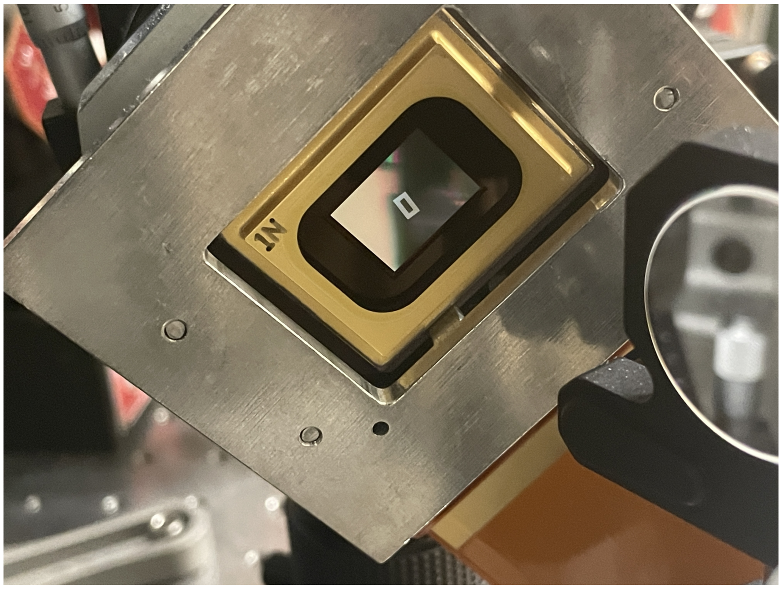

Figure 3.12: A rectangular pattern is loaded into the DMD chip.

models, with an array size of 1920x1080 and each mirror measuring 7.56 μm in size, resulting in over 2 million micromirrors. Each micromirror can be tilted to +/-12^o relative to a flat state, corresponding to an 'on' or 'off' state, with a refresh rate of 9500Hz for binary patterns. The DMD chip is connected to a DLPC900 digital controller via a ribbon cable, and the controller is linked to our lab computer, providing a reliable and efficient programming environment. We program the DMD array with binary image patterns of corresponding resolution, where "1" represents the 'on' state, directing the beam into the vacuum chamber, and "0" represents the 'off' state, diverting the beams away from the system. To control the horizontal and perturbation patterns, we utilized a graphical user interface (GUI) downloaded from the Texas Instruments website, offering sufficient functions for pattern control.

For the vertical box DMD, we utilize VIALUX V7001 SuperSpeed V-Modules, which incorporate TI-DLP7000 with a high performance controller board. Together, they provide a pattern refresh rate up to 32 kHz, mirror size is 13.56um. Figure 3.12 displays a picture showing the binary box pattern loaded into the vertical DMD.

The choice of these DMDs, along with the associated projection beams, is driven by practical considerations. The goal is to construct a box potential that is robust enough to confine atoms with a range of energies for a reasonably long duration, ideally on the order of seconds. The depth of the potential needs to exceed the typical Fermi energy by several times, which is approximately 0.2 μK. Referring back to the expression of the dipole potential in Eq.3.5,3.6 and 3.7, the potential scales inversely with $\omega_0^2-\omega^2$. A beam with frequency close to atomic transition frequency will produce a much deeper potential. However, the beam frequency cannot be too close to the atomic transition frequency, as this would lead to the loss of most atoms. Therefore, we utilize a Toptica single-mode diode laser centered at 669 nm as the source beam for the horizontal DMD. The output for this laser is about 200 mW. This frequency is 2 nm away from atomic transition frequency, which is close enough to produce a strong box wall, about a few μK deep, with such low power (consider the loss of power through the optical path). Also, we only use the horizontal beam to project the two horizontal beam sheets of the box, to ensure negligible atom loss due to this closer to resonance beam.

The setup for the vertical beam requires some additional considerations. We have only two window ports available in the vertical direction of the vacuum chamber: one at the top and one at the bottom. These ports are primarily used for the vertical MOT beams and vertical imaging beams. Given this limitation, we have no other choice to setup the vertical box beam but to share partial of the same beam path with MOT and imaging beam. This arrangement poses no issues for the MOT, as the MOT beam is extinguished at the start of forced evaporation, well before data collection begins. However, for optimal measurements, it is desirable to capture in-situ images to minimize any disturbances to the properties under study. This means that the imaging beams need to be activated when the box beams are present. To separate the imaging beam from the box beam, we utilize a dichroic mirror capable of spectrally separating light based on wavelength. Lowpass dichroic mirrors feature a transmission and reflection band divided by a cut-on wavelength. These dichroics are highly reflective below the cut-on wavelength and highly transmissive above it. By employing such a dichroic mirror, we can separate the box beam from the imaging beam just outside the vacuum chamber.

However, a challenge arises due to the proximity of the 669 nm box beam to the frequency of the imaging beam, which is at 671 nm. This close frequency match makes it nearly impossible to find a suitable dichroic mirror capable of effectively separating them.

Another factor we need to consider is that the vertical beams are also utilized as perturbation beams. Given that the dipole force exerted by the 669 nm beam, even with a small amount of light, is still too strong, we risk losing control over the perturbation strength. Additionally, light close to resonance is more likely to be absorbed by atoms, resulting significant atom loss, therefore it cannot illuminate the atoms for too long.

All of these considerations lead us to opt for a vertical beam that is far from resonance. However, this necessitates a significant increase in input power compared to the horizontal input power. We employ a Coherent Verdi 10 diode laser, which outputs a high-power beam at 532 nm. This wavelength is sufficiently below the atomic transition wavelength, allowing the dichroic mirror to efficiently separate the box beam and imaging beam. The Verdi 10 has an output power of up to 10 watts, but considering the damage threshold of the DMD and losses along the optical path, a 2.2-watt output power is deemed sufficient. Figure 3.13 displays the

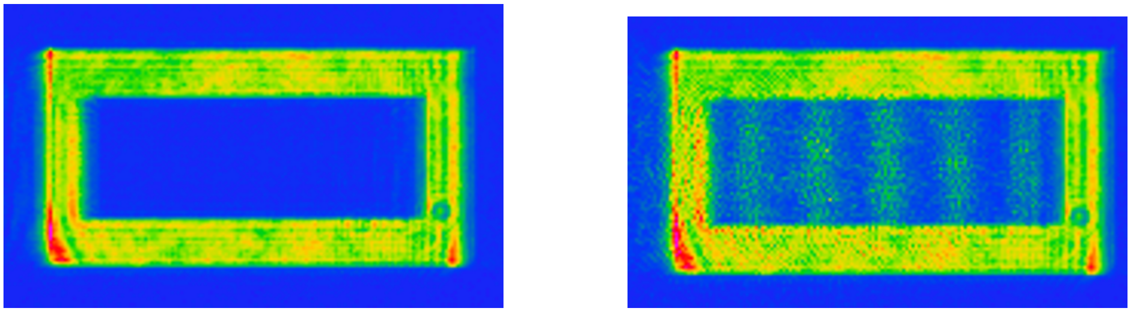

(a)

(b)

Figure 3.13: Box beam pattern taken by Thorlab camera at focus of microscopic objective, the size of the box is 150 $\mu m\times$ 50 μm. (a) image of box only, (b) image of box plus perturbation.

image of pure box pattern(left) along with typical sinusoidal perturbation(right).The images are taken by a ThorLabs DCC1545M CMOS camera(pixel size $\approx 5.3\mu$m) placed at the focal plane of the microscopic objective, which we use to de-magnify the DMD pattern.

3.3.3 Box alignment and loading

With the DMDs and other optical components[Wang (2022)] in place, the next step is to position the box correctly inside the main chamber. Obviously we need to align the box with the FORT, but there is one more thing we need to be aware of: the effect of the bias magnetic field. The experiment is typically conducted in the strongly interacting regime, where $|B|\approx 832$G. Chapter 2 covered the detail electronic structure of ^{6}Li. Refering back to Figure.2.1, we can see that the two lowest states $|1\rangle, |2\rangle$ are both high-field seeking, which means they tend to fall into the high field region. The geometry of the magnets allows for the measurement of single harmonic oscillation frequency to describe the magnetic potential in all three directions. The large size of the magnet coils relative to the atomic cloud creates a harmonic potential for initial energies of the confined atoms, and elementary magnetostatics relates the oscillation frequency of a single direction to the remaining two.

If we position the origin at the center of the atomic cloud, with the CO_2 beam propagating in the z-direction and the two coils aligned along the x-direction, the magnetic field decreases as we approach the origin along the x-axis, while it increases toward the origin in the y-z plane. Given that the two trapped states are high-field seekers, the magnetic potential must be repulsive along the x-axis and attractive along the y and z axes. Thus, we have

$$U_{mag}=-\frac{1}{2}m\omega_{xm}^2x^2+\frac{1}{2}m\omega_{ym}^2y^2+\frac{1}{2}m\omega_{zm}^2z^2 \tag{3.9}$$

Meanwhile, the magnetic dipole moment $\boldsymbol{\mu}$ aligns itself with local magnetic field, leading to $U_{mag} = -\boldsymbol{\mu} \cdot \mathbf{B} = -\mu B$. Maxwell's equation requires $\nabla^2 \mathbf{B} = 0$. Assuming $\mathbf{B} = B\hat{x}$, we have

$$\nabla^2 \mathbf{B} = \nabla^2 B\hat{x} = \nabla^2 \left(\frac{-U_{mag}}{\mu} \right) \hat{x} = 0 \tag{3.10}$$

Using Eq.3.9 yields

$$-\omega_{xm}^2 + \omega_{ym}^2 + \omega_{zm}^2 = 0 \tag{3.11}$$

Cylindrical symmetry of the magnets requires $\omega_{ym} = \omega_{zm}$, therefore

$$\omega_{zm}^2 = \omega_{ym}^2 = \frac{\omega_{xm}^2}{2} \tag{3.12}$$

This implies that the magnetic force in the vertical direction is twice as strong as in the horizontal direction. Additionally, since the force is repulsive, any vertical misalignment of the box position can be easily detected by observing a density distribution leaning toward one side of the wall.

Horizontal alignment is more complex, as the force is weaker and attractive. To align the box centered on the magnetic field, first we need to find where the center is. This is achieved through what we refer to as the "Slosh mode" experiment, where we intentionally release the gas from the FORT at an off-centered position. The cloud then moves toward the horizontal center of the magnetic field and oscillates around this center with an angular frequency of ω_{zm}. The trajectory of the cloud is captured by two CCD cameras. The measurement position of the central density versus time after release in the y-direction is depicted in Figure 3.14. This enables us to determine the degree of deviation from the horizontal center.

With the box positioned correctly, the actual experiment starts with transfer the atoms from FORT into box potential. At the conclusion of forced evaporation, the FORT is maintained at its desired minimum value, and we gradually ramp up (a process taking 0.5 seconds) both the vertical and horizontal box beams to their maximum strength. Subsequently, we release the atoms from the FORT into the box trap by turning off the CO_2 laser power, allowing 80 milliseconds for the atoms to thermalize. Unfortunately, the axial size of the cloud in CO_2 trap, which is over 200 μm, is larger than the typical axial size of the box, 150μm. Consequently, there will always be some portion of the atoms that cannot be captured by the box, as depicted in Figure 3.15.

One might question why not utilize a longer box to capture the entire cloud. The reason lies in the bias magnetic field, which causes the density to vary gradually from the center of the box to its edge. As the length of the box increases, this effect becomes more pronounced. Furthermore, a larger box implies lower density. To maintain a better signal-to-noise ratio and operate within the hydrodynamic regime, it is essential to maintain a reasonably high

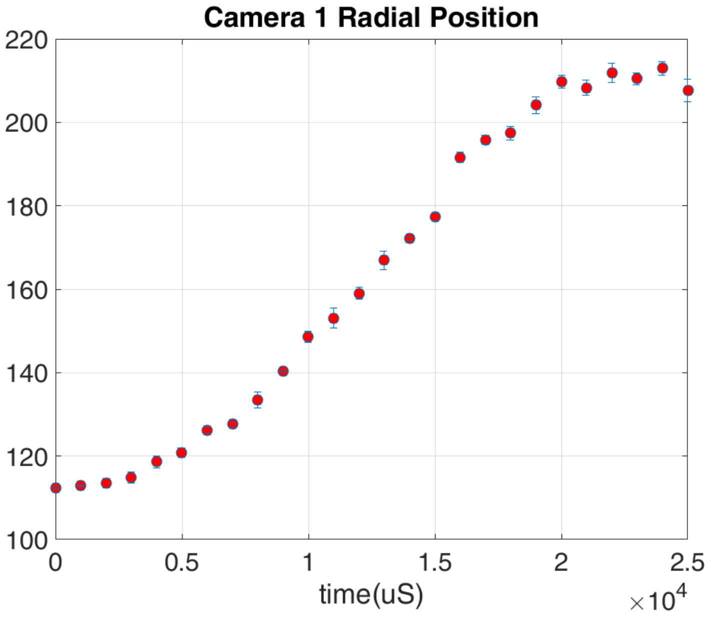

Figure 3.14: Measured position of the central density of the atomic cloud vs time after release from a shallow optical trap which has been moved off of the magnetic bowl center in the attractive y-direction. The magnets are producing a field of 832 Gauss. Though only a portion of one oscillation is visible in the plot, the frequency is found within a quarter of one hertz to be $\omega_{ym} = 2\pi \times 21.5(0.25)$Hz.

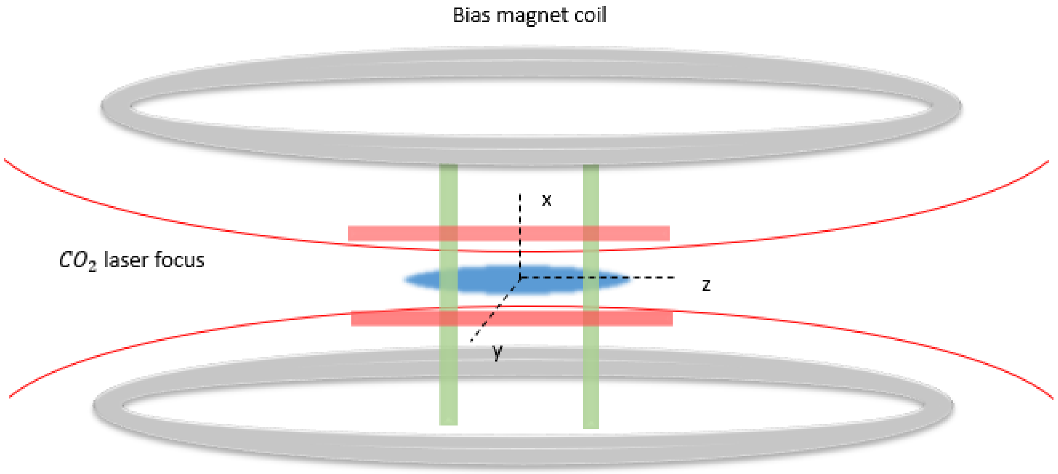

Figure 3.15: Atomic cloud after forced evaporation in the FORT, with box beam raising up. The cloud is over 200 μm long in z direction. The vertical box beam (green) cut at the edge of the cloud,result loss of portion of the atoms.

atom density. For day to day experiments, we can load approximately 75,000 to 80,000 atoms per spin state into the box. Figure 3.16 are images of atoms trapped inside the box, where the box potential $U_0(\mathbf{r})$ produces a rectangular density profile with typical dimension $(x, y, z) = (52 \times 50 \times 150)\ \mu m$. The density varies slowly in the axial z direction due to the magnetic field curvature, but exhibits almost no effect on the narrow radial x and y directions.

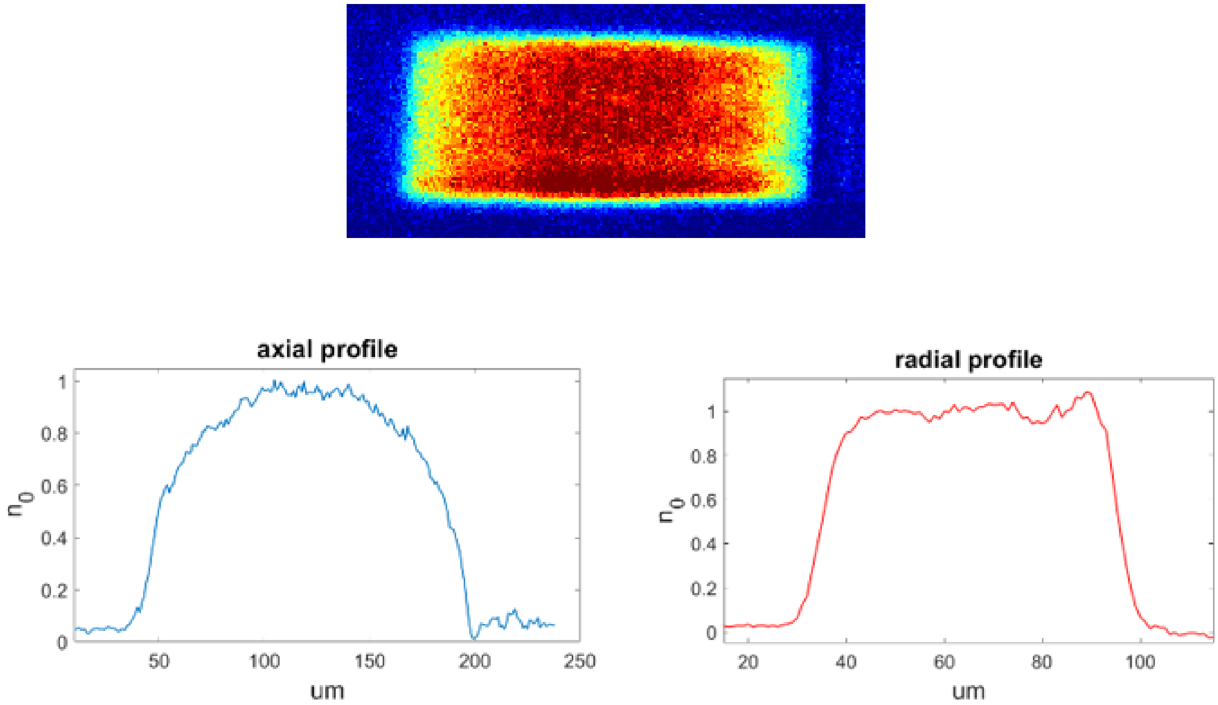

Figure 3.16: Absorption image of atomic cloud confined by the box potential(upper), taken by the horizontal CCD camera, with the normalized 1D density distribution along axial direction(lower left) and radial direction(lower right)

3.3.4 Perturbing potential

For the hydrodynamic experiments, we establish the initial condition by introducing a small perturbation potential, $\delta U(z)$, to the atom cloud and allowing it to reach equilibrium. This sinusoidal periodic optical potential is generated using the vertical beam DMD and has the following form:

$$\delta U(z) = \epsilon[1 + \cos(qz + \phi)]. \tag{3.13}$$

Here, ϵ represents a small amplitude coefficient, which determines the maximum strength

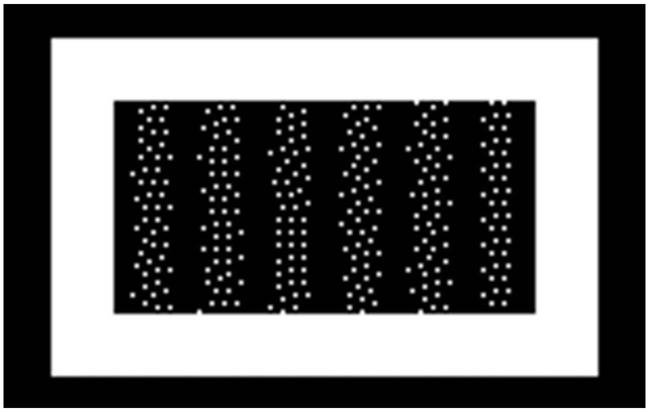

Figure 3.17: Binary pattern of the sinusoidal perturbation with six spatial periods, generated by the “JarvisHalftone” error diffusion method.

of the perturbation. The parameter $q = 2\pi/\lambda$ is the spatial frequency of the modulation, while ϕ denotes a phase factor used to position the perturbation relative to the box. These values are designated as programmable input parameters to generate the DMD patterns.

To generate the binary pattern of the sinusoidal perturbation, we employ the error diffusion algorithm [Floyd (1976); Ulichney (1987)]. Error diffusion, a form of halftoning, operates by dispersing the quantization error accrued during the conversion process to neighboring pixels, thereby spreading the error across the image. In our application, we utilize "JarvisHalftone", a method where an input grayscale image is converted into a halftone image of the same size using Jarvis’s Error Diffusion Method. Figure 3.17 depicts the typical binary pattern utilized for the hydrodynamic relaxation experiment.

3.3.5 Independent control of perturbations

As we have mentioned before, in our previous experiments, the vertical DMD was responsible for generating both the box walls and the perturbations within the box trap. In the first experiment [Baird et al. (2019)], where we measured the hydrodynamic linear response, the sinusoidal perturbation needed to propagate through the box axially with different speeds, ranging from subsonic to supersonic. In the second experiment [Wang et al. (2022)], where we measured the hydrodynamic relaxation, a static sinusoidal perturbation needed to be smoothly ramped up then turned off instantly. Figure 3.18 shows the binary pattern we used to project the perturbation. The perturbation was created by switching the patterns in sequence. All these experimental conditions can only be fulfilled with the high refresh rate DMD, where the micromirror arrays can be switched between on and off below 30 μs. However, this setup has some serious limitations. First, the perturbation beam comes from the same source-the vertical DMD-as the vertical box beam, which means we can only control the strength of the perturbation by reducing or increasing the number of micromirrors projecting the perturbation. Therefore only a small portion of micromirrors could be used to generate the perturbation; otherwise, it would be too strong to perform any experiments.

Figure 3.18: Perturbation patterns switching on one by one in the hydrodynamic relaxiation experiment. These binary patterns were uploaded on vertical DMD and triggered in sequence.

Due to this limitation in dynamic range, our ability to vary the wavelength for the perturbation was restricted. This constraint led to the experiment in [Wang et al. (2022)] primarily using a wavelength around 22 μm. In our new experiment, however, we seek to investigate whether the measured coefficients depend on the wavelength or remain independent. Consequently, we require a new method that allows for reliable changes in the perturbation wavelength.

Additionally, the changing of perturbation was realized by flipping the micromirrors.For the hydrodynamic relaxation experiments, the perturbation was gradually switched on pattern by pattern, as shown in Figure 3.18. This approach may result in unexpected heating of the atoms. Additionally, the mirror switching procedure inevitably results in some atom loss.

To address the previously discussed challenges, we adopted a straightforward solution: separating the box beam from the perturbation beam. Our goal was to independently control both the wavelength and intensity of the perturbation relative to the box beam. To achieve this, we redesigned our vertical beam path and introduced a third DMD dedicated to projecting the perturbation only, the new optical layout is depicted in Figure 3.19. Figure 3.20 is the picture of the new optical system setup in our lab for the vertical beam path.

The perturbation DMD we employed is TI-DLP6500. After the DMDs projecting the desired patterns, the box beam and perturbation beam are combined using a polarizing beam splitter(PBS) before entering the chamber. The intensity of each beam is controlled by two AOMs (not shown in the figure). So the intensity of perturbation is fully controlled by the AOM now. During the experiment cycle, after the box beam reaches its full strength, we switch off the CO_2 laser trap and allow the atoms to thermalize within the box trap. Subsequently, the perturbation AOM gradually ramps up the perturbation beam. We load only one pattern into

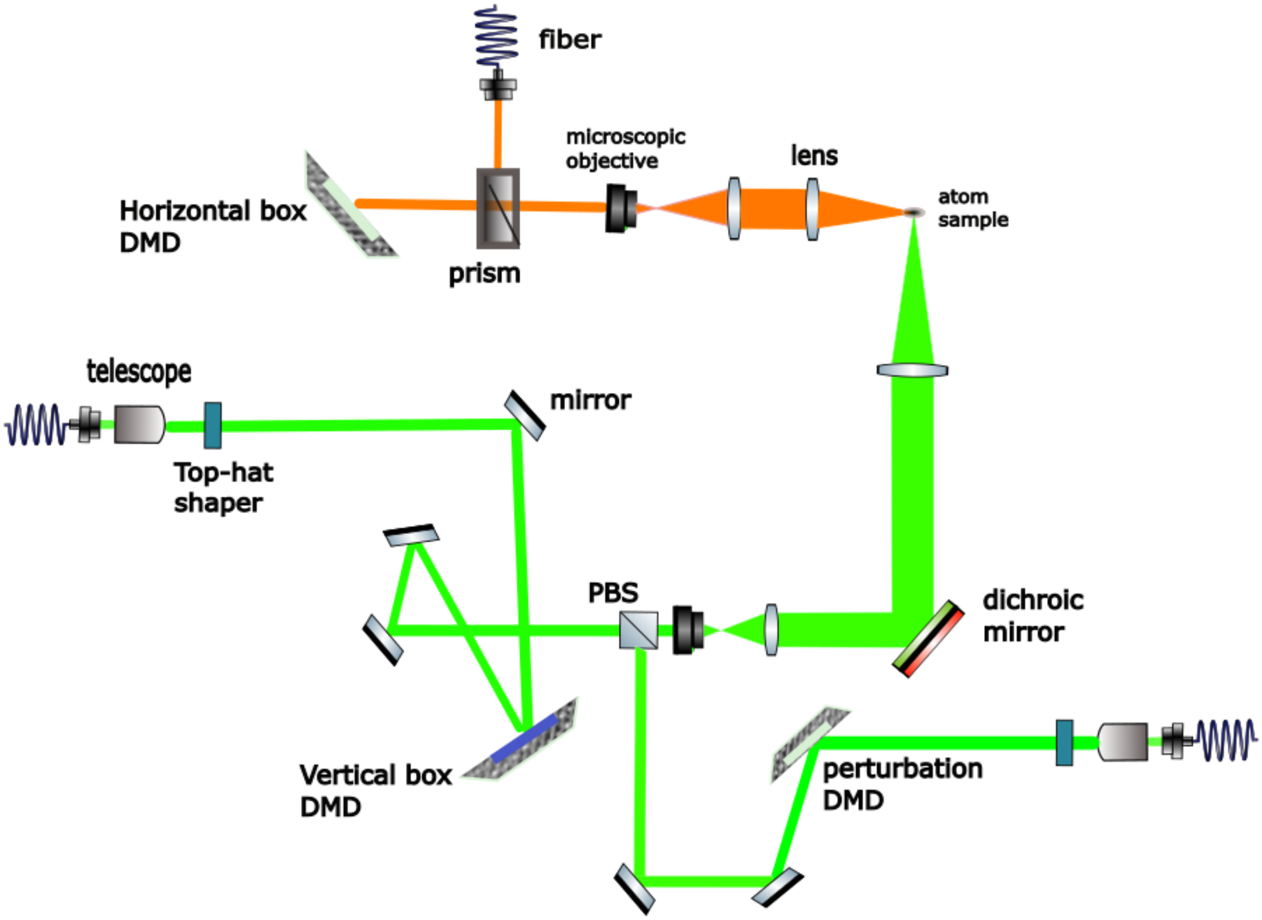

Figure 3.19: New box beam and perturbation beam setup around main chamber. The vertical box DMD and perturbation DMD generate vertical box bema and perurbation beam separately. They are combined at the polarizing beam splitter placed before the microscopic objective.

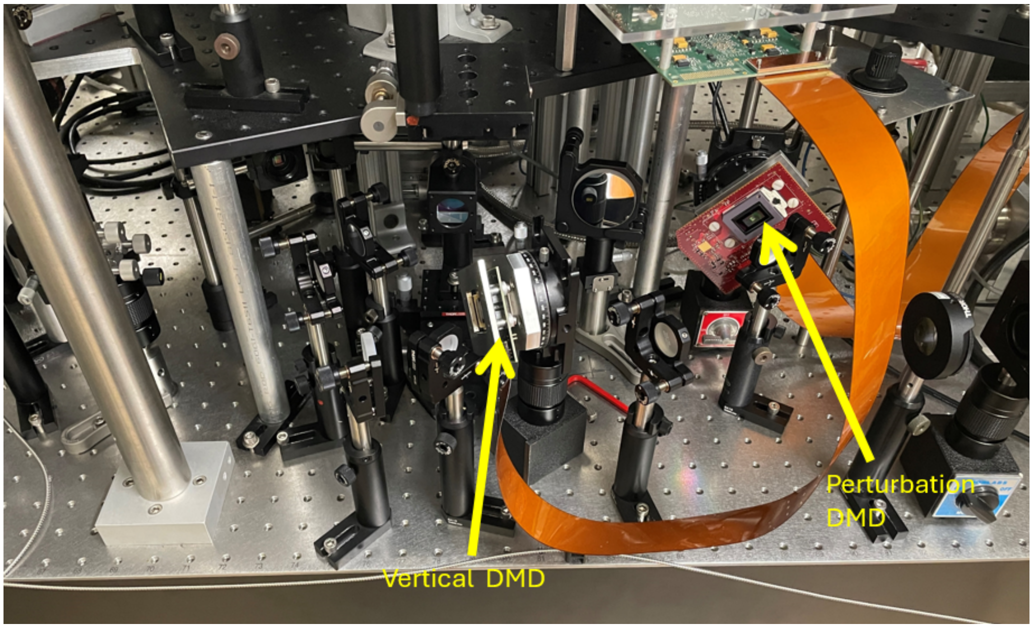

Figure 3.20: Picture of the new vertical optical system setup in our lab. Vertical DMD and perturbation DMD are shown in the picture.

the perturbation DMD, generating the desired perturbation on the atoms. The perturbation beam takes approximately 10 ms to reach its maximum intensity. Figure 3.21 illustrates the power ramp of the perturbation beam over time, measured by a photodiode detector. In the actual experiment, we first load the sinusoidal pattern into the perturbation DMD. Once atoms have thermalized inside the box trap, the AOM ramps up the perturbation beam linearly, then hold it at its maximum for tens of milliseconds until the atoms come to equilibrium again. The overall atomic cloud exhibits the sinusoidal modulation as shown in Figure 3.22. Subsequently, we abruptly switch off the perturbation and allow the density profile to relax.

This ramping method is much better than previous method of switching mirrors, thereby avoiding unnecessary heating and potential atom loss. More importantly, this independent control of perturbation frees us from the limitation of dynamical range. We are now able to utilize essentially arbitrary perturbation wavelengths, and the perturbation strength can be easily adjusted by the AOM to match the desired pattern. Figure 3.22 and Figure 3.23 are the absorption images of the atomic cloud trapped in the box potential with perturbation of four different wavelengths. We also plot the corresponding normalized density variation along z-direction. In actual experiments, this sets the initial condition for studying the hydrodynamic relaxation.

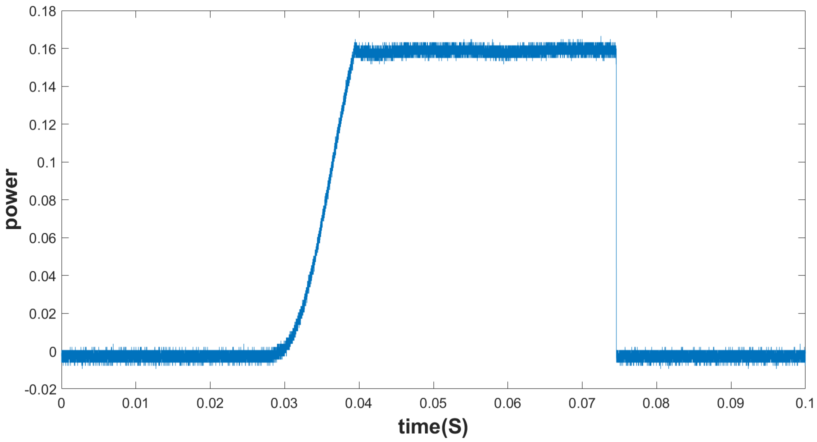

Figure 3.21: Measured perturbation beam power versus time, it takes roughly 10ms to ramp up the perturbation. The power is controlled by a separate AOM. The perturbation power is held at its maximum for tens of miliseconds so that the system can thermalize, then abruptly turned off to initialize the relaxiation.

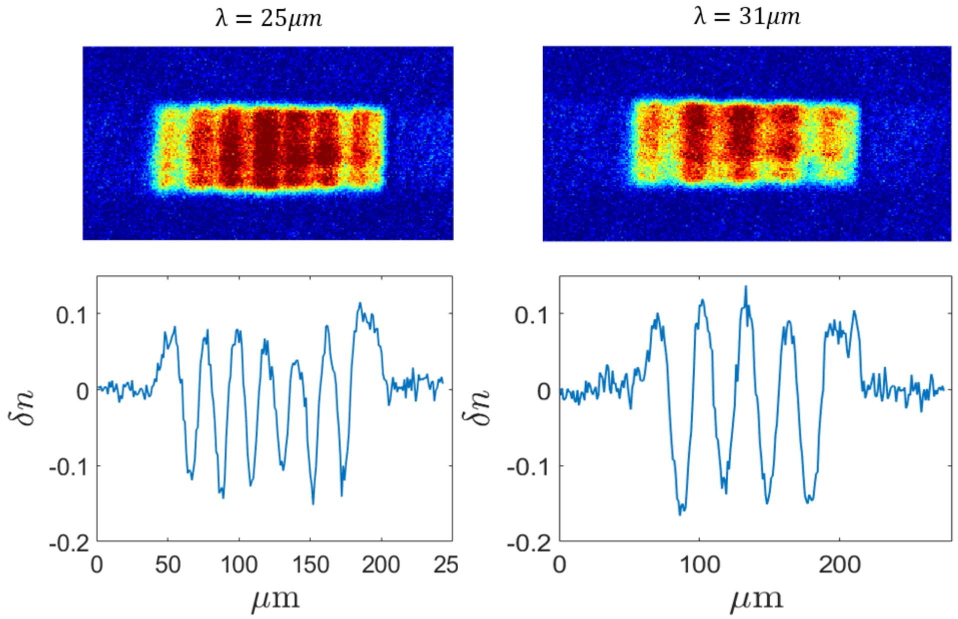

Figure 3.22: Absorption images of atomic cloud in the box trap with perturbation wavelength of 25 μm and 31 μm.

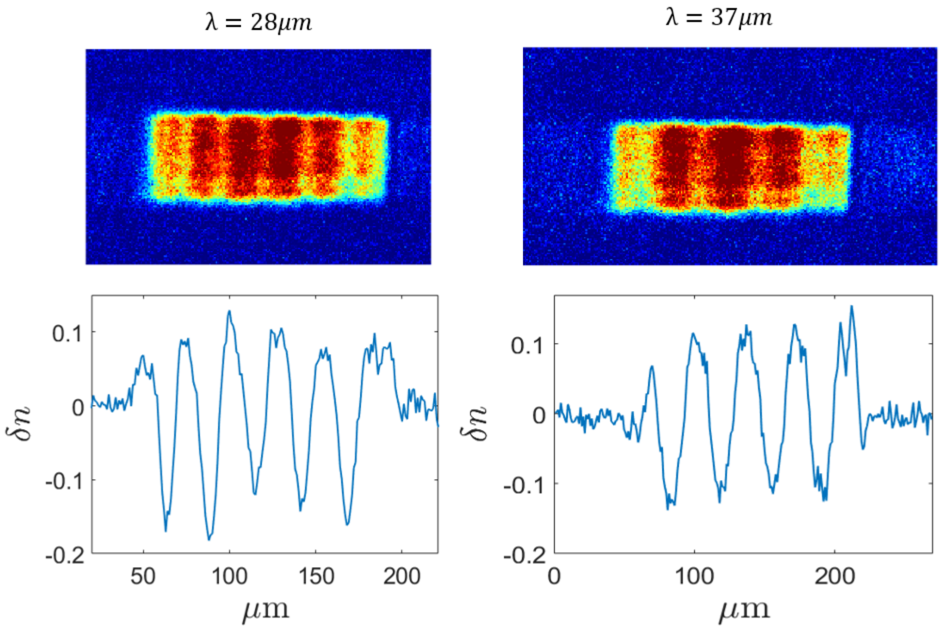

Figure 3.23: Absorption images of atomic cloud in the box trap with perturbation wavelength of 28 μm and 37 μm.

3.3.6 Cancelling the density variation due to the bias magnetic field

The perturbation DMD can now project any pattern without restriction of the intensity of light. One experiment we did is to try to cancel the density variation of the axial direction caused by the magnetic bowl, as shown in Figure 3.16. The bias field creates a harmonic confining potential $\propto z^2$ in the axial direction, resulting the near quadratic density variation. In order to cancel this effect, we need to program the DMD to project an inverse quadratic intensity distribution using the perturbation beam. When combined, these two potentials effectively raise the bottom of the magnetic bowl, resulting in an almost uniform density profile as illustrated in Figure 3.24.

In principle, we can calculate the 2D image of DMD pattern numerically and design the pattern to obtain desired potentials. However, due to optical interference, the actual dipole potential is sensitive to precise alignment of optical elements and imperfections in the setup, making it difficult to predict accurately in a real-world setting. Hence, an iterative pattern optimization is necessary to obtain the best possible reconstruction of the target potential. Figure 3.25 shows the atomic cloud trapped in the box with added correcting potential. We plot the normalized 1-dimensional density distribution along axial direction(red curve), and compare it with the original non-perturbed distribution(blue curve). It shows that we have created a region over 100μm long around the center of the box where the density distribution

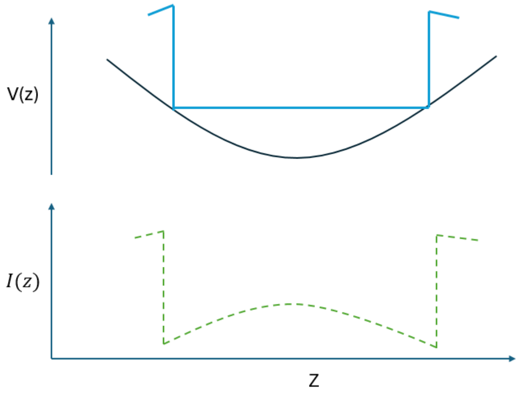

Figure 3.24: Illustration of cancelling the density variation due to bias field. The magnetic potential(black curve) is harmonic near the center. We project a customized beam with quadratic intensity distribution(green dashed curve). This intensity profile needs to achieve the target potential(blue curve).

is nominally uniform.

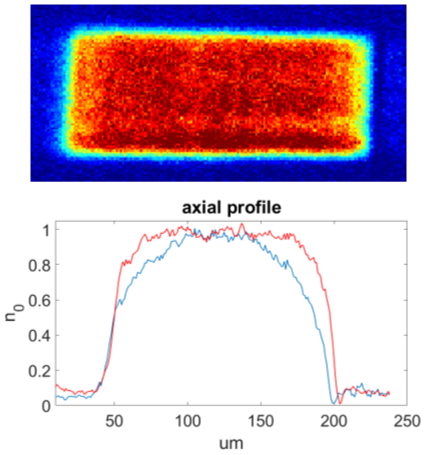

Figure 3.25: Absorption image of an almost uniform atom density distribution(upper) and the normalized 1D density profile along z direction(lower). Blue curve is the original density distribution, red curve is with correcting potential.

CHAPTER

4

HYDRODYNAMICS AND THERMODYNAMICS

This chapter covers hydrodynamic and thermodynamic theory, which are the main frame for describing the evolution of a unitary Fermi gas following a perturbation inside the optical box potential for our experiment. I will first cover the basic of hydrodynamics and thermodynamics. Then I will describe the new relaxiation model, which we directly fit the two relaxiation times,τ_η and τ_κ, associated with shear viscosity η and thermal conductivity κ. We then calculate η and κ from the extracted relaxiation times. There is an important benefit of fitting the relaxation times directly, instead of fitting the transport coefficients, η and κ, as we did in the previous experiments [Wang et al. (2022)]. We extract the universal hydrodynamic relaxation times τ_η and τ_κ directly from fitting the free-decay of the spatially periodic density perturbation. The extracted relaxation times determines the **static shear viscosity, static thermal conductivity**, and universal density shift parameters, corrected for the finite response time over which the viscous force and heat current relax to their Navier-Stokes forms. In the following, we first derive the thermodynamic relations that appear in our hydrodynamic model. Then briefly discuss the universal thermodynamics of the unitary Fermi gas. Finally we will cover in detail the hydrodynamic relaxation model.

4.1 Thermodynamic relations

We begin by deriving the basic thermodynamic relations that will be used in our later hydrodynamic model. Defining V_1 as the volume per particle, the density is $n = 1/V_1$. The expansivity is

$$\beta \equiv \frac{1}{V_1}\left(\frac{\partial V_1}{\partial T}\right)_p = -\frac{1}{n}\left(\frac{\partial n}{\partial T}\right)_p . \tag{4.1}$$

Note that β has a dimension of inverse temperature.

The iosthermal sound speed c_T and adibatic sound speed c_S are defined by

$$m c_T^2 = \left(\frac{\partial p}{\partial n}\right)_T = -\left(\frac{\partial p}{\partial T}\right)_n \left(\frac{\partial T}{\partial n}\right)_p , \tag{4.2}$$

$$m c_S^2 = \left(\frac{\partial p}{\partial n}\right)_{s_1} = -\left(\frac{\partial p}{\partial s_1}\right)_n \left(\frac{\partial s_1}{\partial n}\right)_p , \tag{4.3}$$

where we have defined s_1 as the entropy per particle in Eq 4.3.

Taking the ratios of Eq 4.2 and Eq 4.3, noticing that $(\partial T/\partial n)_p = 1/(\partial n/\partial T)_p$ and $(\partial p/\partial s_1)_n = 1/(\partial s_1/\partial p)_n$, we obtain the well-known relation

$$\frac{c_T^2}{c_S^2} = \frac{\left(\frac{\partial s_1}{\partial p}\right)_n \left(\frac{\partial p}{\partial T}\right)_n}{\left(\frac{\partial s_1}{\partial n}\right)_p \left(\frac{\partial n}{\partial T}\right)_p} = \frac{\left(\frac{\partial s_1}{\partial T}\right)_n}{\left(\frac{\partial s_1}{\partial T}\right)_p} = \frac{c_{V_1}}{c_{P_1}} \tag{4.4}$$

where $c_{V_1} = T(\partial s_1/\partial T)_n$ and $c_{P_1} = T(\partial s_1/\partial T)_p$ are the heat capacities per particle at constant volume and at constant pressure.

Next, we find the first order pressure change, δp which will be needed later. We have

$$\delta p = \left(\frac{\partial p}{\partial n}\right)_T \delta n + \left(\frac{\partial p}{\partial T}\right)_n \delta T = \left(\frac{\partial p}{\partial n}\right)_T \left[\delta n + \left(\frac{\partial n}{\partial p}\right)_T \left(\frac{\partial p}{\partial T}\right)_n \delta T\right]. \tag{4.5}$$

Applying the chain rule gives

$$\left(\frac{\partial n}{\partial p}\right)_T \left(\frac{\partial p}{\partial T}\right)_n = -\left(\frac{\partial n}{\partial T}\right)_p = \beta n, \tag{4.6}$$

where we have used Eq 4.1 for expansivity β. From Eq 4.2, Eq 4.5 and Eq 4.6, we have

$$\delta p = m c_T^2 (\delta n + \delta \tilde{T}). \tag{4.7}$$

Here, we have defined a scaled temperature that has a dimension of density

$$\delta\tilde{T} \equiv \beta n \delta T. \tag{4.8}$$

For the first order temperature change, we have

$$\delta T = \left(\frac{\partial T}{\partial n}\right)_{s_1} \delta n + \left(\frac{\partial T}{\partial s_1}\right)_n \delta s_1 = \left(\frac{\partial T}{\partial s_1}\right)_n \left[\left(\frac{\partial s_1}{\partial T}\right)_n \left(\frac{\partial T}{\partial n}\right)_{s_1} + \delta s_1\right]. \tag{4.9}$$

The chain rule gives

$$\left(\frac{\partial s_1}{\partial T}\right)_n \left(\frac{\partial T}{\partial n}\right)_{s_1} = -\left(\frac{\partial s_1}{\partial n}\right)_T, \tag{4.10}$$

which we evaluate as follows. Consider $s_1[T, n(T,p)]$. Then

$$c_{P_1} = T\left(\frac{\partial s_1}{\partial T}\right)_p = T\left(\frac{\partial s_1}{\partial T}\right)_n + T\left(\frac{\partial s_1}{\partial n}\right)_T \left(\frac{\partial n}{\partial T}\right)_p = c_{V_1} - \beta n T \left(\frac{\partial s_1}{\partial n}\right)_T. \tag{4.11}$$

Therefore,

$$\left(\frac{\partial s_1}{\partial n}\right)_T = -\frac{c_{p_1} - c_{V_1}}{\beta n T}. \tag{4.12}$$

With $(\partial T/\partial s_1)_n = T/c_{V_1}$ and Eq 4.10, Eq 4.9 takes the simple form,

$$\delta T = \left(\frac{c_{P_1}}{c_{V_1}} - 1\right)\frac{\delta n}{\beta n} + \frac{T\delta s_1}{c_{V_1}}. \tag{4.13}$$

Here, the first term is the adiabatic change in temperature arising from the change in density. For a monatomic gas in the high temperature limit, Eq 4.1 with $n = p/k_B T$ gives $\beta \to 1/T$ and $c_{P_1}/c_{V_1} - 1 \to 2/3$. Then, $\delta T/T = 2/3(\delta n/n)$, i.e., $T/T_0 = (n/n_0)^{2/3}$ as expected. For a unitary Fermi gas, where $s_1 = k_B f_S(\theta)$, this result holds for all temperature, since $(\partial T/\partial n)_{s_1} = (\partial T/\partial n)_\theta$, with $T = \theta\, T_F$, and $T_F \propto n^{2/3}$. The second term is the temperature change arising from the heat flow per particle, $T\delta s_1 = \delta q_1$.

4.2 Universal thermodynamics

For the unitary Fermi gas, universality [Ho (2004)] requires that the pressure p and the energy density $\mathcal{E}$ are functions only of density and temperature, related by $p = 2\mathcal{E}/3$. Dimensional analysis then shows that the energy density takes the simple form

$$\mathcal{E} = \frac{3}{5} n \epsilon_F(n) f_E(\theta) \equiv n E_1, \tag{4.14}$$

where E_1 is the energy per particle and $\theta \equiv T/T_F$ is the reduced temperature with T_F the local Fermi temperature. For a balanced 50-50 mixture of two spin components of total density n, the local Fermi energy is $k_B T_F = \epsilon_F(n) = \hbar^2(3\pi^2 n)^{2/3}/(2m)$. The universal function $f_E(\theta)$, which has been measured in [Ku et al. (2012)], determines all of the thermodynamic properties. The pressure is then

$$p = \frac{2}{5} n\epsilon_F(n) f_E(\theta). \tag{4.15}$$

At high temperature limit, $f_E(\theta) \to 5\theta/2$, we have the classic thermodynamic relation

$$p = n k_B T \tag{4.16}$$

The entropy density is

$$s = n k_B f_S(\theta) = n s_1(\theta) \equiv n s_1, \tag{4.17}$$

where s_1 is entropy per particle and $f_S(\theta)$ can be determined from $f_E(\theta)$.

The adibatic sound speed Eq 4.3 is obtained from Eq 4.15, as Eq 4.17 requires constant θ for constant s_1,

$$m c_S^2 = \left(\frac{\partial p}{\partial n}\right)_\theta = \frac{2}{3}\epsilon_F(n) f_E(\theta) = \frac{10}{9} E_1, \tag{4.18}$$

where the last form on the right follows from Eq 4.14. Since $\epsilon_F(n) = m v_F^2/2$, Eq 4.18 yields

$$c_S^2 = \frac{v_F^2}{3} f_E(\theta). \tag{4.19}$$

The isothermal sound speed, Eq 4.2, is determined from Eq 4.15, with $p = p[n, \theta(n, T)]$,

$$c_T^2 = \frac{1}{m}\left(\frac{\partial p}{\partial n}\right)_T = \frac{v_F^2}{3}\left[f_E(\theta) - \frac{2}{5}\theta f_E'(\theta)\right], \tag{4.20}$$

where $f_E'(\theta) = \partial_\theta f_E(\theta)$. At high temperature limit, $f_E(\theta) \to 5\theta/2$, we have

$$m c_T^2 = k_B T \tag{4.21}$$

From Eq 4.19 and Eq 4.20, we can see that c_S/v_F and c_T/v_F are completely determined by the universal function $f_E(\theta)$. With the measured $f_E(\theta)$ in [Ku et al. (2012)], we can plot c_S/v_F and c_T/v_F as a function of reduced temperature θ,i.e. T/T_F. Alternatively, because θ is monotonically increasing with increasing c_S/v_F and c_T/v_F, we can plot T/T_F as a function of c_S/v_F or c_T/v_F, as shown in Figure 4.1. This relation is very important, it serves as thermometer for our experiment: we can determine the reduced temperature of atoms trapped in the box potential from the measured density and sound speed. The data in Figure 4.1 are fitted with a

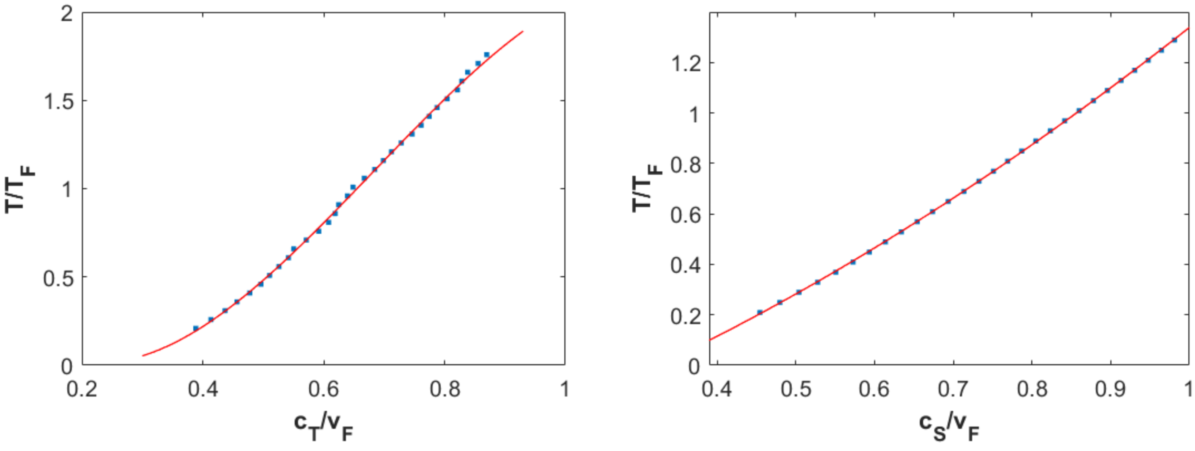

(a) (b)

Figure 4.1: (a) Reduced temperature $\theta = T/T_F$ as a function of c_T/v_F. (b) Reduced temperature $\theta = T/T_F$ as a function of c_S/v_F. For $\theta > 0.2$, θ increases monotonically with c_T/v_F and c_S/v_F. Blue dots are obtained from measured Equation of State from [Ku et al. (2012)]. Red curves are fitting with cubic polynomials: $\theta(c_T/v_F) = 0.478 - 4.410(c_T/v_F) + 11.688(c_T/v_F)^2 - 5.711(c_T/v_F)^3$; $\theta(c_S/v_F) = -0.399 + 0.958(c_S/v_F) + 0.839(c_S/v_F)^2 - 0.059(c_S/v_F)^3$. These relations serve as thermometers in our experiments, where the reduced temperature is determined from the fitted sound speed.

cubic polynomial $\theta(c_T/v_F)$ and $\theta(c_S/v_F)$.

The heat capacity per particle at constant volume takes a simple form. Using Eq 4.14,

$$c_{V_1} = T\left(\frac{\partial s_1}{\partial T}\right)_n = \left(\frac{\partial E_1}{\partial T}\right)_n = \frac{3}{5} k_B f_E'(\theta). \tag{4.22}$$

Eq 4.4 then determines the ratio $c_{P_1}/c_{V_1} = c_S^2/c_T^2$ from Eq 4.19 and Eq 4.20,

$$\frac{c_{P_1}}{c_{V_1}} = \frac{f_E(\theta)}{f_E(\theta) - \frac{2}{5}\theta f_E'(\theta)}. \tag{4.23}$$

Finally, Eq 4.22 and Eq 4.23 determine

$$\frac{1}{c_{V_1}} - \frac{1}{c_{P_1}} = \frac{1}{k_B}\frac{2}{3}\frac{\theta}{f_E(\theta)} \tag{4.24}$$

which will appear later when we derive the equation for sound diffusivity.

With Eq 4.15, we have

$$\frac{\theta}{k_B f_E(\theta)} = \frac{T}{T_F k_B f_E(\theta)} = \frac{T}{\epsilon_F f_E(\theta)} = \frac{2}{5}\frac{nT}{p}, \tag{4.25}$$

Eq 4.24 then takes the form [Ku et al. (2012)]

$$\frac{1}{c_{V_1}} - \frac{1}{c_{P_1}} = \frac{4}{15}\frac{nT}{p}. \tag{4.26}$$

4.3 Hydrodynamic theory

The hydrodynamic theory forms the foundation of our data analysis model. In this section, we derive a kinetic theory relaxation model, which is used to extract the hydrodynamic transport time τ_η for the shear viscosity and τ_κ for the thermal conductivity from the measured free oscillatory decay of a spatially periodic density perturbation in the normal phase of a unitary Fermi gas.

4.3.1 Hydrodynamic linear response for a normal fluid

Consider a normal phase unitary Fermi gas, which is a single component fluid with with mass density $\rho \equiv mn$, where n is the total particle density (we assume a 50-50 mixture of two spin components) and m is the atom mass. $\rho(\mathbf{r}, t)$ satisfies the continuity equation,

$$\partial_t \rho + \partial_i(\rho\, v_i) = 0, \tag{4.27}$$

where a sum over $i = x, y, z$ is implied. The mass flux (momentum density) is $\rho\, v_i$, with $v_i(\mathbf{r}, t)$ the velocity field.

Our experiments measure the response of the density in the central region of the box over short enough time scales that forces arising from the walls of the box can be neglected. As the perturbing potential $\delta U = 0$ during the measured evolution, then momentum density and corresponding momentum flux $\rho\, v_i\, v_j$ obey

$$\partial_t(\rho\, v_i) + \partial_j(\rho\, v_i\, v_j) = -\partial_i p - \partial_j p^1_{ij}, \tag{4.28}$$

where $-\partial_i p$ is the force per unit volume arising from the scalar pressure p and $\partial_j p^1_{ij}$ is the viscous force per unit volume, which we will determine using a kinetic theory relaxation model later. Taking the divergence of Eq 4.28 and using Eq 4.27, we immediately obtain

$$-\partial^2_t \rho + \partial_i \partial_j(\rho\, v_i\, v_j) = -\partial^2_i p - \partial_i \partial_j p^1_{ij}. \tag{4.29}$$

In the linear response regime, the second term on the left hand side is second order in small quantities and can be dropped. Focusing on one dimension, taking $\delta n = n - n_0$, where n_0 is the unperturbed background density, the change in density $\delta n(z,t)$ obeys

$$\partial_t^2 \delta n = \frac{1}{m}\partial_z^2 \delta p + \frac{1}{m}\partial_z^2 p_{zz}^1. \tag{4.30}$$

As our initial condition is isothermal, we find the pressure change $\delta p = p - p_0$ in terms of the changes in the density δn and temperature δT. In this case, the pressure change can be written in the form $\delta p = m c_T^2(\delta n + \delta \tilde{T})$, as in Eq. 4.7, so that

$$\delta \ddot{n} = c_T^2 \partial_z^2 (\delta n + \delta \tilde{T}) + \frac{1}{m}\partial_z^2 p_{zz}^1 \tag{4.31}$$

where $\delta \tilde{T} \equiv n_0 \beta \delta T$ with $\beta = -1/n(\partial n/\partial T)_p$ the expansivity.

Next, we require the evolution equation for δT, which obeys [Wang et al. (2022)],

$$\delta \dot{T} = \epsilon_{LP} \frac{\delta \dot{n}}{\beta n_0} + \frac{\delta \dot{q}}{n_0 c_{V_1}}, \tag{4.32}$$

where $\epsilon_{LP} = c_{P_1}/c_{V_1} - 1$ is the Landau-Placzek parameter, which describe the adibatic change in the temperature arising from the change in density. c_{V_1}, c_{P_1} are heat capacities per particle. The heat flow per unit volume $\delta \dot{q} = -\partial_z J_E$, where J_E is the energy current, which we determine from a kinetic theory relaxation model later. Multiplying Eq 4.32 by $n_0 \beta$, we obtain

$$\delta \dot{\tilde{T}} = \epsilon_{LP} \delta \dot{n} - \frac{\beta}{c_{V_1}} \partial_z J_E \tag{4.33}$$

4.3.2 Kinetic theory relaxation model

In this section, we derive the relaxation model equations for the normal phase unitary Fermi gas, which determine how the viscous force and heat current relax to their Navier-Stokes forms. To proceed, we rewrite Eq 4.31 as

$$\boxed{\delta \ddot{n} = c_T^2 \partial_z^2 (\delta n + \delta \tilde{T}) + \delta Q_\eta} \tag{4.34}$$

where

$$\delta Q_\eta \equiv \frac{1}{m}\partial_z^2 p_{zz}^1. \tag{4.35}$$

Similarly, Eq 4.33 is written as

$$\boxed{\delta\dot{\tilde{T}} = \epsilon_{LP}\delta\dot{n} + \delta Q_\kappa} \tag{4.36}$$

with

$$\delta Q_\kappa = -\frac{\beta}{c_{V_1}}\partial_z J_E. \tag{4.37}$$

We derive the evolution equations for δQ_η and δQ_κ using a relaxation time approximation for the Boltzmann equation. In this case, the single particle phase space distribution $f(\mathbf{r},\mathbf{v},t)$ obeys

$$\partial_t f + \mathbf{v}\cdot\nabla f = -\frac{1}{\tau}(f - f_0) \equiv -\frac{1}{\tau} f_1 \tag{4.38}$$

with τ is the relaxation time and $f = f_0 + f_1$, with f_0 the equilibrium distribution.

In the high-temperature Maxwell-Boltzmann limit, the equilibrium distribution is

$$f_0 = n_0 W_0(\mathbf{U})\,, \tag{4.39}$$

where $\mathbf{U} = \mathbf{v} - \mathbf{u}$ is the particle velocity relative to the stream velocity $\mathbf{u}(\mathbf{r},t)$ and $\int d^3\mathbf{U}\,W(\mathbf{U}) = 1$. Here

$$W_0(\mathbf{U}) = \frac{e^{-\mathbf{U}^2/v_0^2}}{(v_0\sqrt{\pi})^3}\,, \tag{4.40}$$

where $v_0 = \sqrt{2k_B T/m}$ is the thermal speed. In general, the background temperature T_0 spatially varies $T \equiv T(\mathbf{r})$. For convenience, we drop the subscript $_0$ and use T for the temperature in deriving the relaxation equations.

Without specifying the phase space distribution f, the pressure tensor is given by

$$p_{ij} = m\int d^3\mathbf{U}\,U_i U_j f(\mathbf{r},\mathbf{v},t). \tag{4.41}$$

Taking $p_{ij} = p_{ij}^0 + p_{ij}^1$, the scalar pressure $p_0 \equiv p$, is immediately obtained from $p_{ij}^0 = \delta_{ij}p$ with $f = f_0$ and $i = j = x$,

$$p = m\int d^3\mathbf{U}\,U_x^2 f_0. \tag{4.42}$$

Writing $\int d^3\mathbf{U}\,U_x^2 f_0 = n_0\langle U_x^2\rangle \equiv n_0\overline{U_x^2}$, we have

$$p = n_0 m\overline{U_x^2} \tag{4.43}$$

which gives $p \rightarrow n_0 k_B T_0$ in the Maxwell-Boltzmann limit with Eq 4.40.

Shear viscosity

We find the relaxation equation for δQ_η of Eq 4.35 from that of p^1_{ij}, assuming that the stream velocity $\mathbf{u}(\mathbf{r}, t)$ is position dependent, producing a shear stress. Here, we assume that the background temperature T_0 is spatially constant. To proceed, we first consider Eq 4.41 for $i \neq j$. The equilibrium distribution f_0 is a symmetric function of $\mathbf{U}$, so that

$$\int d^3\mathbf{U} U_i U_j f_0 = 0. \tag{4.44}$$

Then Eq 4.41 with $f = f_0 + f_1$ and Eq 4.44 yield

$$p^1_{ij} = m \int d^3\mathbf{U} U_i U_j f = m \int d^3\mathbf{U} U_i U_j f_1. \tag{4.45}$$

Multiplying Eq 4.38 by $\int d^3\mathbf{U} U_i U_j$ and using Eq 4.45, we obtain

$$\dot{p}^1_{ij} + m \int d^3\mathbf{U} U_i U_j v^k \partial_k f = -\frac{1}{\tau_\eta} p^1_{ij}, \tag{4.46}$$

where we define $\tau \equiv \tau_\eta$ for the shear viscosity. Then

$$\dot{p}^1_{ij} + \frac{1}{\tau_\eta} p^1_{ij} = -I_{ij}, \tag{4.47}$$

where

$$I_{ij} = m \int d^3\mathbf{U} U_i U_j v^k \partial_k f = m \int d^3\mathbf{U} U_i U_j v^k \frac{\partial U^l}{\partial x^k} \frac{\partial f}{\partial U^l}. \tag{4.48}$$

For fast relaxation, where $f_1 \to \tau_\eta v_k \partial_k f$ in Eq 4.38, we see that $p^1_{ij} \backsimeq \tau_\eta I_{ij}$ is already first order in τ_η, so that we can take $f \to f_0$ in Eq 4.48. Using $\mathbf{U} = \mathbf{v} - \mathbf{u}$,

$$\frac{\partial U^l}{\partial x^k} = -\frac{\partial u^l}{\partial x^k}. \tag{4.49}$$

Then with $v_k = U_k + u_k$ in Eq 4.48, we obtain

$$I_{ij} = -m \frac{\partial u^l}{\partial x^k} \int d^3\mathbf{U} U_i U_j (U_k + u_k) \frac{\partial f_0}{\partial U^l}. \tag{4.50}$$

Integrating by parts, we then have

$$I_{ij} = m \frac{\partial u^l}{\partial x^k} \int d^3\mathbf{U} \frac{\partial}{\partial U^l} [U_i U_j (U_k + u_k)] f_0, \tag{4.51}$$

Using $\partial U_i/\partial U_l = \delta_{il}$ and defining $\int d^3\mathbf{U} g(\mathbf{U}) f_0(\mathbf{U}) = n_0\langle g(\mathbf{U})\rangle$, Eq 4.51 can be rewritten as

$$I_{ij} = m\frac{\partial u^l}{\partial x^k} n_0\{\delta_{ij}\langle U_j(U_k+u_k)\rangle + \delta_{jl}\langle U_i(U_k+u_k)\rangle + \delta_{kl}\langle U_i U_j\rangle\} \tag{4.52}$$

Eq 4.52 is simplified with

$$n_0\langle U_j(U_k+u_k)\rangle = \int d^3\mathbf{U}\, U_j(U_k+u_k)\, f_0 = n_0\,\delta_{jk}\overline{U_x^2}, \tag{4.53}$$

where the u_k term vanishes since f_0 is symmetric in U_j. Hence, we can write $\langle U_i U_j\rangle = \delta_{ij}\overline{U_x^2}$. With $p = n_0 m\,\overline{U_x^2}$ from Eq 4.43, we have

$$I_{ij} = p\frac{\partial u^l}{\partial x^k}\{\delta_{il}\delta_{jk} + \delta_{jl}\delta_{ik} + \delta_{kl}\delta_{ij}\}. \tag{4.54}$$

Carrying out the sums over repeated indices, we obtain

$$I_{ij} = p\left(\frac{\partial u^i}{\partial x^j} + \frac{\partial u^j}{\partial x^i} + \delta_{ij}\nabla\cdot\mathbf{u}\right), \tag{4.55}$$

where the δ_{ij} term vanishes for $i \neq j$.

To determine p^1_{ij} for all i, j, we consider the symmetric second rank traceless pressure tensor,

$$p^1_{ij} \to m\int d^3\mathbf{U}\left(U_i U_j - \frac{1}{3}\delta_{ij}\mathbf{U}^2\right) f_1. \tag{4.56}$$

where the f_0 part of f vanishes because it is scalar function of $\mathbf{U}$. Since $\mathbf{U}^2 = Tr\{U_i U_j\}$, evaluating Eq. 4.56 just changes I_{ij} in Eq. 4.47 and Eq. 4.55 to

$$I_{ij} \to I_{ij} - \frac{1}{3}\delta_{ij}Tr\{I_{ij}\} \equiv p\,\sigma_{ij}. \tag{4.57}$$

The δ_{ij} term in Eq. 4.55 makes no contribution to the symmetric traceless tensor, yielding

$$\sigma_{ij} = \frac{\partial u^i}{\partial x^j} + \frac{\partial u^j}{\partial x^i} - \frac{2}{3}\delta_{ij}\nabla\cdot\mathbf{u} \tag{4.58}$$

With Eq. 4.57 and Eq. 4.58, Eq. 4.47 determines the relaxation equation for the shear stress tensor,

$$\dot{p}^1_{ij} + \frac{1}{\tau_\eta}p^1_{ij} = -p\,\sigma_{ij}. \tag{4.59}$$

For small τ_η, $\dot{p}^1_{ij} \ll p^1_{ij}/\tau_\eta$, we see that

$$p^1_{ij} \to -\tau_\eta p\,\delta_{ij} = -\eta\,\sigma_{ij}, \tag{4.60}$$

where

$$\eta = \tau_\eta p \tag{4.61}$$

is the static shear viscosity.

Now we can evaluate δQ_η, Eq. 4.35. To first order in small quantities, current conservation, Eq. 4.27, requires $\delta\dot{n} + n_0\,\partial_z v_z = 0$, so that

$$\sigma_{zz} = \frac{4}{3}\,\partial_z v_z = -\frac{4}{3}\,\frac{\delta\dot{n}}{n_0}. \tag{4.62}$$

Then, using Eqs. 4.35, 4.58 and 4.59, we obtain finally,

$$\boxed{\delta\dot{Q}_\eta + \frac{1}{\tau_\eta}\delta Q_\eta = \frac{4}{3}\,\frac{p}{m n_0}\,\partial_z^2\delta\dot{n}.} \tag{4.63}$$

For fast relaxation, $\delta\dot{Q}_\eta \ll \delta Q_\eta/\tau_\eta$, we find,

$$\delta Q_\eta \to \frac{4}{3}\,\frac{\tau_\eta p}{m n_0}\,\partial_z^2\delta\dot{n} = \frac{4}{3}\,\frac{\eta}{m n_0}\,\partial_z^2\delta\dot{n}. \tag{4.64}$$

In this limit, Eq. 4.34 with Eq. 4.64 reproduces the Navier-Stokes form used in [Wang et al. (2022)]. We note that Eq. 4.63 is independent of the form of the single particle phase space distribution, $f_0(\mathbf{r},\mathbf{v})$, which has not been explicitly used.

Thermal conductivity

Next, we assume a temperature gradient $T(\mathbf{r})$ and find the relaxation equation for δQ_κ of Eq. 4.37 from that of the 1D energy current, J_E,

$$J_E = \int d^3\mathbf{v}\,v_z\,\frac{m}{2}\,\mathbf{v}^2\,f, \tag{4.65}$$

which vanishes for $f = f_0$, since the integrand would be odd in v_z. Using Eq. 4.38 with $\tau \equiv \tau_\kappa$, we have

$$\dot{J}_E + \frac{m}{2}\,\partial_z\int d^3\mathbf{v}\,v_z^2\mathbf{v}^2\,f_0 = -\frac{1}{\tau_\kappa}\,J_E \tag{4.66}$$

or

$$\dot{J}_E + \frac{1}{\tau_\kappa} J_E = -\partial_z I_{zz}. \tag{4.67}$$

Here

$$I_{zz} = \frac{m}{2} \int d^3\mathbf{v}\, v_z^2 \mathbf{v}^2 f_0. \tag{4.68}$$

We take the equilibrium phase space distribution to be $f_0(\mathbf{r},\mathbf{v}) = n_0(\mathbf{r})\, W_0(\mathbf{v})$, where

$$W_0(\mathbf{v}) = \frac{e^{-\mathbf{v}^2/v_0^2}}{(v_0\sqrt{\pi})^3} \tag{4.69}$$

with $v_0 = \sqrt{2k_B T/m}$ the thermal speed. We assume that $T = T(\mathbf{r})$ spatially varies, producing a temperature gradient, as discussed below. Then,

$$I_{zz} = \frac{m}{2}\frac{1}{3}\langle v^4\rangle\, n(\mathbf{r}). \tag{4.70}$$

Here,

$$\langle v^4\rangle = \int d^3\mathbf{v}\, v^4\, W_0(\mathbf{v}) = \frac{4}{\sqrt{\pi}} v_0^4 \int d\left(\frac{v}{v_0}\right)\left(\frac{v}{v_0}\right)^6 e^{-(v/v_0)^2}, \tag{4.71}$$

which yields

$$\langle v^4\rangle = \frac{15}{4}\, v_0^4 = 15\left(\frac{k_B T}{m}\right)^2. \tag{4.72}$$

Using Eq. 4.72 in Eq. 4.70, and the pressure $p(\mathbf{r}) = n(\mathbf{r})\, k_B T(\mathbf{r})$, we have

$$I_{zz} = \frac{5}{2}\frac{k_B}{m}\, n(\mathbf{r})\, k_B T^2(\mathbf{r}) = \frac{5}{2}\frac{k_B}{m}\, p(\mathbf{r})\, T(\mathbf{r}). \tag{4.73}$$

With Eq. 4.67, we then obtain

$$\dot{J}_E + \frac{1}{\tau_\kappa} J_E = -\frac{5}{2}\frac{k_B}{m}\, \partial_z[\, p(\mathbf{r})\, T(\mathbf{r})\,]. \tag{4.74}$$

For pure heat flow, mechanical equilibrium requires

$$\nabla p(\mathbf{r}) = 0. \tag{4.75}$$

Therefore, Eq. 4.74 becomes

$$\dot{J}_E + \frac{1}{\tau_\kappa} J_E = -\frac{5}{2}\frac{k_B}{m}\, p\; \partial_z \delta T, \tag{4.76}$$

where we suppress the argument $\mathbf{r}$. Note that the temperature $T = T_0 + \delta T$, with T_0 the uniform background temperature, so that $\partial_z T = \partial_z \delta T$.

For fast relaxation, where $\dot{J}_E \ll J_E/\tau_\kappa$, Eq. 4.76 gives

$$J_E \to -\frac{5}{2}\frac{k_B}{m}\,\tau_\kappa\, p\, \partial_z \delta T \equiv -\kappa_T\, \partial_z \delta T. \tag{4.77}$$

Here, we see that the static thermal conductivity is

$$\kappa_T = \frac{5}{2}\frac{k_B}{m}\,\tau_\kappa\, p\,. \tag{4.78}$$

We find $\delta\dot{Q}_\kappa$ using Eq. 4.37, $\delta Q_\kappa \equiv -(\beta/c_{V_1})\,\partial_z\, J_E$. Then, operating on Eq. 4.76 with $-(\beta/c_{V_1})\,\partial_z$, we have

$$\boxed{\delta\dot{Q}_\kappa + \frac{1}{\tau_\kappa}\delta Q_\kappa = \frac{5}{2}\frac{k_B}{m}\frac{p}{n_0 c_{V_1}}\,\partial_z^2\,\delta\tilde{T},} \tag{4.79}$$

where $\delta\tilde{T} = n_0\beta\,\delta T$ (see Eq. 4.31).

We note that the explicit coefficient 5/2 in Eq. 4.79 is dependent on the assumed Maxwell-Boltzmann approximation for the phase space distribution f_0, which was used to evaluate Eq. 4.69. For fast relaxation, where $\delta\dot{Q}_\kappa \ll \frac{1}{\tau_\kappa}\delta Q_\kappa$, Eq. 4.79 gives

$$\delta Q_\kappa \to \frac{5}{2}\frac{k_B}{m}\frac{\tau_\kappa\, p}{n_0 c_{V_1}}\,\partial_z^2\delta\tilde{T} = \frac{\kappa_T}{n_0 c_{V_1}}\,\partial_z^2\,\delta\tilde{T}. \tag{4.80}$$

In this limit, Eq. 4.36 with Eq. 4.80 reproduces the Navier-Stokes form in [Wang et al. (2022)].

Eqs. 4.34, 4.63, 4.36 and 4.79 together constitute our hydrodynamic relaxation model. Different from the model used in [Wang et al. (2022)], where we assumed instantaneous local relaxation, (i.e. $\tau_\eta = 0, \tau_\kappa = 0$), here we explicitly incorporate the finite relaxation times into our model. Next chapter will cover the experimental results that justifies the new model [Li et al. (2024)], where the measurements demonstrate that τ_η and τ_κ are small, but not negligible, compared to the timescales for the oscillatory decay of the density perturbation.

CHAPTER

5

DATA PROCESSING AND SIMULATION

With all the experimental and theoretical materials introduced, we are now ready to discuss our experimental results and data analysis techniques we used to analyze the data.

5.1 Data processing

The experiment starts with taking background shots, which are images of the atom cloud trapped inside the box potential without any perturbation. At the end of forced evaporation, the box beams are slowly ramped up(takes about 500 ms) by two AOMs. After the box beam reaches its maximum, we abruptly turn off the FORT, the atoms start to oscillate inside the box, and eventually come to equilibrium. One thing worth discussing is the time scale for extinguishing the CO_2 laser trap. The proper procedure should be adiabatically ramped down the CO_2 laser power, so that the atoms can smoothly transfer to the box without any loss. In reality, we usually load the atoms from a very shallow CO_2 trap. Usually the final trap depth is only 0.18% of the total CO_2 power, the energy of the atoms is low enough so that they can not escape from the box regardless of the switching procedure. This is not true when we release the atoms from trap with higher depth, 0.5% for instance , the atoms are "hotter" and the cloud is vertically compressed more strongly, so that sudden release from the FORT results huge loss of atoms. Additionally, raising the CO_2 laser trap depth compresses the cloud vertically, transverse to the axial direction, result in an axially longer cloud. Since we can not extend the box axially further, more atoms will not be captured by the box potential.

The typical background image is shown in Figure 3.16, which also includes the normalized density distribution along z-axis. From this we can calculate the static box potential $U_0(z)$. In order to improve the signal to noise ratio, we do not use the original background density profile to do the calculation directly. Instead, we fit our normalized 1-D background density profile with an analytic function first.

For the 1-D density profile, we always work with the normalized density distribution, where we devide the over all density distribution by its peak value n_0[1]. We can then fit $\tilde{n}_0(z) = n_0(z)/n_0$ with an analytic function, which is a multiplication of tanh function and a polynomial,

$$h(z) = \frac{\tanh[(z - z_{10})/w_1] - \tanh[(z - z_{20})/w_2]}{2} \sum_n a_n z^n. \tag{5.1}$$

The numerator on the right hand side, the difference between the two tanh functions, produces a top-hat shape of nominal width $z_{20} - z_{10}$. w_1 and w_2 determine the slopes on each side. The flat top is modulated by multiplying a polynomial. Figure 5.1 shows a typical fit with a fifth order polynomial. The density offset outside of the box region comes from atoms trapped outside the box. They are trapped by the repulsive box potential and the harmonic trap generated by the bias magnetic field, which is attractive on z-axis.

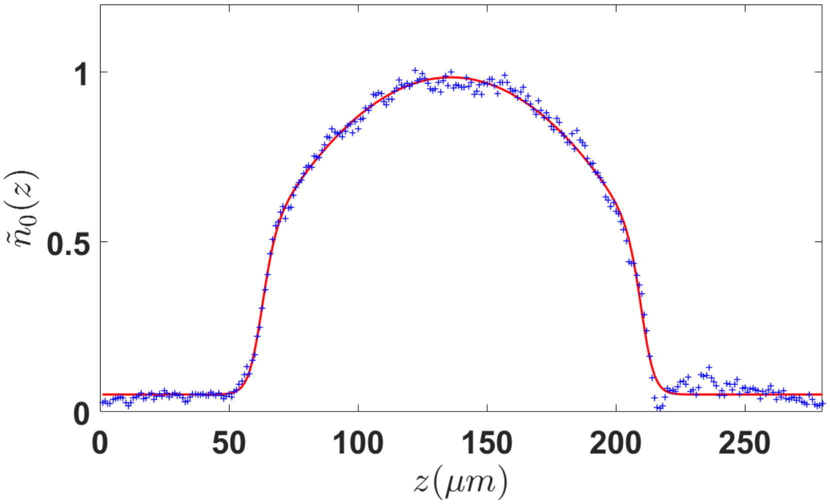

Figure 5.1: Normalized 1D background density $\tilde{n}_0(z)$ along the axial direction. Blue dots are data, red solid curve is fitting with Eq. 5.1 up to $n = 5$.

---

[1] In actual analysis, we define n_0 as the average density of the central 35 μm region

With a smooth density profile obtained from the fit, we can derive the confining potential of the box trap from the chemical potential μ. The force arising from the confining potential along z-axis can be extracted from the measured 1-D density profile $n_0(z)$. The trapping potential is easily found in the local density approximation from the local chemical potential, $\mu(z)$, where $\mu(z)+U_0(z)=\mu_G$, with μ_G the global chemical potential. Then

$$U_0(z)=\mu_G-\mu(z)=\mu_G-\epsilon_F[n_0(z)]f_\mu[\theta(z)] \tag{5.2}$$

Here, $f_\mu(\theta)$ is a dimensionless universal function of reduced temperature θ, which determines μ in terms of local Fermi energy $\epsilon_F(n)$. $f_\mu(\theta)$ has been measured precisely in [Ku et al. (2012)]. The reduced temperature $\theta(z)=T_0/T_F(n)=\theta_0/[\tilde{n}_0(z)]^{2/3}$. $\theta_0=T_0/T_F(n_0)$ is determined from the measured isothermal sound speed c_T and $\tilde{n}_0(z)=n_0(z)/n_0$, here n_0 is the central density. The global chemical potential is then $\mu_G=\epsilon_F(n_0)f_\mu(\theta_0)$, so that $U_0=0$ at the region where $n_0(z)=n_0$ by construction. We define $\tilde{U}_0(z)=U_0(z)/\epsilon_F(n_0)$, then

$$\tilde{U}_0(z)=f_\mu(\theta_0)-[\tilde{n}_0(z)]^{2/3}f_\mu(\theta_0/[\tilde{n}_0(z)]^{2/3}). \tag{5.3}$$

We obtain $U_0(z)$ in units of $\epsilon_F(n_0)$ as shown in Figure 5.2Typically, we have $\epsilon_F(n_0)\simeq 0.18\ \mu$K, the box depth $U_0\simeq 0.75\ \mu$K.

After taking the background images, we add the perturbation beam and start to take density relaxation data. The perturbation beam is adiabatically turned on and held at maximum for around 30 ms so that the atoms can thermalize. The cloud exhibits this sinusoidal density variation as shown in Figures. 3.22 and 3.23, as we have discussed before, this serves as our initial condition. Therefore, the initial condition is directly measured without any approximation or involvement of free fitting parameters.

In principle, one can start with this initial spatial density profile and simulate the whole evolution process. However, we have found that the initial condition is easily affected by noise, imaging imperfection and effect of the wall, especially the region close to the box wall where the oscillation amplitude is small. In practice, we apply a band-pass noise filter to the data in order to discard the noise and improve the performance of fitting. Figure. 5.3 shows the raw data (red) and processed data (blue). We can see that the filtered data are smoother and in good agreement with the fitting. Additionally, the filtering process help us choose the region of interest (ROI) more precisely, where it contains exactly an integer number of spatial periods.

For a sinusoidal perturbation, the best way to analyze the evolution is to look at the Fourier space. We perform a Fast Fourier Transform (FFT) and focus on the dominant Fourier component that has the largest $|\delta n(q)|$, as shown in Figure. 5.4, since it contains most information. In actual analysis, we found that the real part of $\delta n(q)$ contains the correct information we need,

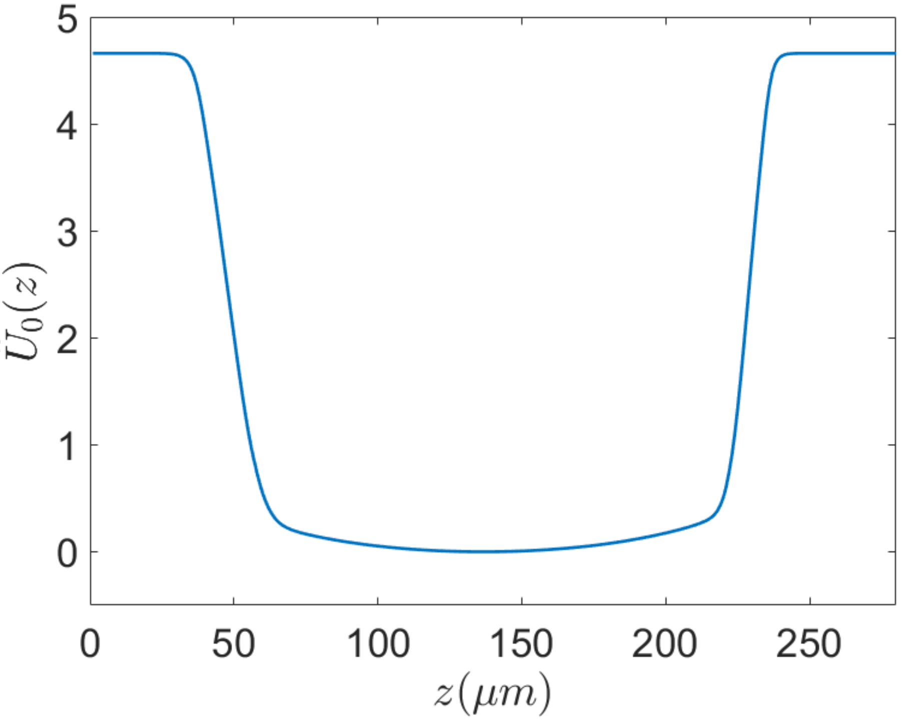

Figure 5.2: Typical box potential $\tilde{U}_0(z)$ in units of central Fermi energy $\epsilon(n_0)$ claculated from Eq. 5.3 for the density profile of Figure 5.1.

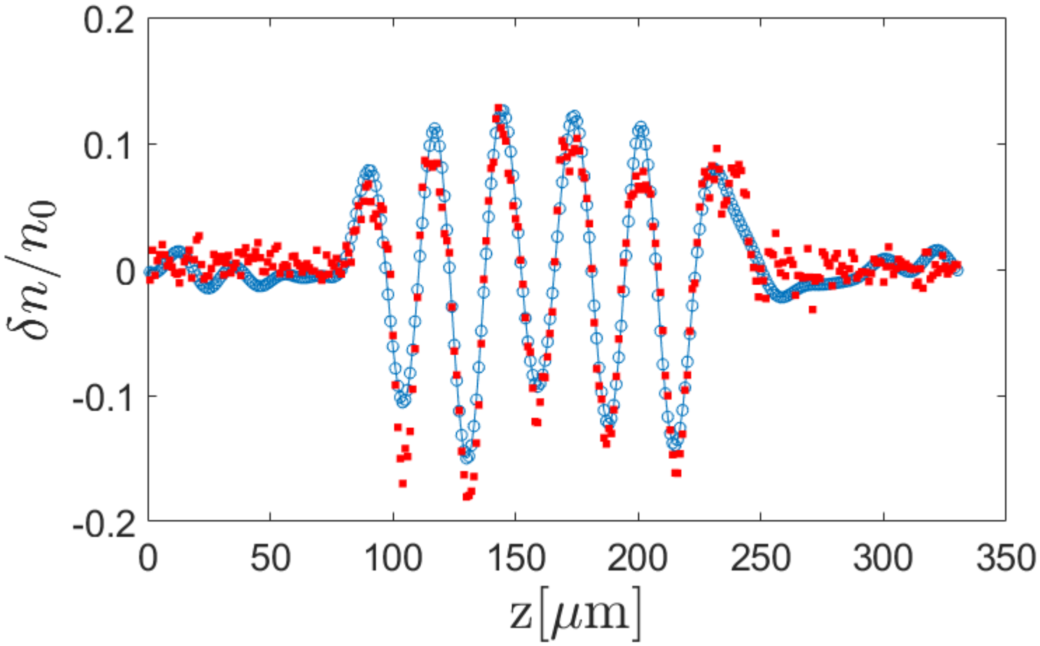

Figure 5.3: Spatial profile of raw data (red dot) and processed data (blue circle) with fitting. The perturbation wavelength $\lambda \approx 28\mu$m.

the imaginary part is negligible and just gives a small phase shift. By carefully choosing the ROI, we can minimize this phase shift and make sure it does not contribute. The corresponding q is in agreement with the perturbation wavelength we use.

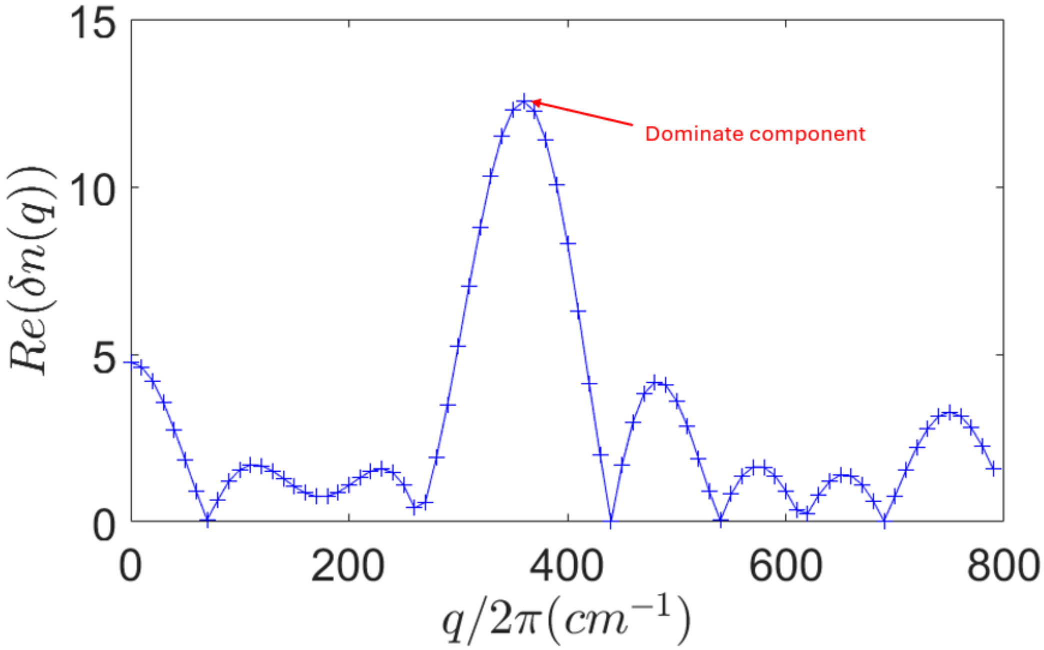

Figure 5.4: FFT of the data in Figure. 5.3. Real part of $\delta n(q)$ as a function of $q/2\pi$. The dominant component has the largest amplitude and contains the most useful information.

The q value is found from the initial condition where the perturbation amplitude is maximum, and then fixed for all later time to make sure that the data analysis is consistent. Therefore the data that we fit with our model is Re($\delta n(q,t)$). From now on we use $\delta n(q,t)$ to denote Re($\delta n(q,t)$). We compare $\delta n(q,t)$ with the predicted value $\delta n_p(q,t)$ from our hydrodynamic model. We use the standard Chi-square test to compare $\delta n(q,t)$ and $\delta n_p(q,t)$ at each time,

$$\chi^2(q) = \sum_{t_i} \frac{(\langle \delta n(q,t_i) \rangle - \delta n_p(q,t))^2}{\sigma^2_{\delta n(q,t_i)}} \tag{5.4}$$

Here $\delta n_p(q,t_i)$ is obtained from simulation at given time t_i by fitting τ_η, τ_κ and c_T in the hydrodynamic model in chapter 4. Detail fitting method will be covered later in this chapter. In one experiment cycle, we take 5 to 8 shots through the whole sequence of t_i in random order. $\langle \delta n(q,t_i) \rangle$ is the mean of all $\delta n(q,t_i)$ at t_i. $\sigma_{\delta n(q,t_i)}$ is the standard deviation from the mean at each t_i.

5.2 Determining the central density

The central 3D-density n_0 is used to find the central Fermi energy, corresponding Fermi Temperature T_F, and Fermi speed v_F, which determines the reduced temperature $\theta \equiv T/T_F$ from the measured isothermal sound speed c_T using the known equation of state [Ku et al. (2012)]. The reduced temperature then determines the thermodynamic properties of the sample.

In order to get n_0, we take images of the trapped cloud along the x and y axes with two cameras. In this way, we measure the two-dimensional column densities $\tilde{n}(z,x) = \int_{-\infty}^{\infty} dy\, n(x,y,z)$ and $\tilde{n}(z,y) = \int_{-\infty}^{\infty} dx\, n(x,y,z)$, for each spin state, where z denotes the long axis of the box and x denotes the direction of the bias magnetic field. For our experiment, the typical box dimensions are $\Delta x = 52\ \mu$m, $\Delta y = 50\ \mu$m, and $\Delta z = 150\ \mu$m.

The curvature of the bias magnetic field produces a harmonic confining potential $\propto z^2$, which causes a noticeable variation of the density over 150 μm as we discussed in chapter 3. In contrast, the confining potential $\propto y^2$ produces a much smaller variation of the density over 50 μm along y direction. Further, the number of atoms trapped outside the box along x and y is negligible. We note that the measured $n(y)$ is distorted on the right side. This is an artifact of the imaging path for the vertical camera, which is collinear with the vertically projected beams that form the sides of the box potential. We assume that the true shapes are nearly identical.

The one-dimensional density along axial direction that we use in analysis, is obtained by integrating the measured 2D-column density over a limited central region along x, where the density is slowly varying,

$$n(z) = \int_{x_1}^{x_2} dx\, \tilde{n}(z,x) \tag{5.5}$$

To estimate the 3D density, we assume that $n(x,y,z)$ approximately factors, as it would in a true 3D box potential,

$$n(x,y,z) \simeq \tilde{n}(x,z)\, n(y) \tag{5.6}$$

We normalize $\int_{-\infty}^{\infty} dy\, n(y) = 1$, so that $\int_{-\infty}^{\infty} dy\, n(x,y,z) = \tilde{n}(x,z)$ as it should. The normalized 1D density $n(y)$, averaged near the center of the box $y = y_c$, is essentially the inverse of the box length L_y along y, as it would for a true box potential. We determine

$$n(y) = \frac{\int_{z_1}^{z_2} dz\, \tilde{n}(z,y)}{\int_{-\infty}^{\infty} dy \int_{z_1}^{z_2} \tilde{n}(z,y)} \tag{5.7}$$

where $\tilde{n}(z,y)$ is the column density measured by the camera oriented along x direction. $n(y)$ satisfies $\int_{-\infty}^{\infty} dy\, n(y) = 1$ for any choice of z_1 and z_2. We take z_1 and z_2 in the central region of the cloud, where the density is nearly uniform, as used to measure the Fourier transform

$\delta n(q,t)$.

Averaging the column density near the center, x_c, z_c, where the 2D density is nearly uniform, we obtain the total central density $n_0 = 2\tilde{n}(x_c, z_c)n(y_c)$. For a single spin state, typical values are $n(y_c) = 0.0196/\mu\text{m} = 196/\text{cm}$, i.e. $L_y = 51.0\ \mu\text{m}$, and $\tilde{n}(x_c, z_c) = 8.72\times 10^8/\text{cm}^2$, which yields $n_0/2 = 1.71\times 10^{11}/\text{cm}^3$. From n_0 we find the Fermi speed v_F. This in turn determines the reduced temperature $\theta(c_T/v_F)$, where $c_T = \omega_T/q$ is determined from the fit to $\delta n(q,t)$.

5.3 Hydrodynamic simulation

Our simulation starts with the hydrodynamic relaxation model we derived in chapter 4, namely the four coupled differential equations,

$$\delta\ddot{n} = c_T^2\partial_z^2(\delta n + \delta\tilde{T}) + \delta Q_\eta \tag{5.8}$$

$$\delta\dot{Q}_\eta + \frac{1}{\tau_\eta}\delta Q_\eta = \frac{4}{3}\frac{p}{m n_0}\partial_z^2\delta\dot{n} \tag{5.9}$$

$$\delta\dot{\tilde{T}} = \epsilon_{LP}\delta\dot{n} + \delta Q_\kappa \tag{5.10}$$

$$\delta\dot{Q}_\kappa + \frac{1}{\tau_\kappa}\delta Q_\kappa = \frac{5}{2}\frac{k_B}{m}\frac{p}{n_0 c_{V_1}}\partial_z^2\delta\tilde{T} \tag{5.11}$$

Eqs. 5.8 and 5.10 describe the changes in density $\delta n(z,t)$ and temperature $\delta T(z,t)$, Eqs. 5.9 and 5.11 describe the relaxation of viscous force and heat current.

One can directly integrate these four equations numerically, but that would be too time consuming and inefficient. The best way to do the analysis, as we discussed before, is to look at Fourier space. We perform a spatial Fourier transformation for the four equations and define the time dependent Fourier components $\delta n(q,t) \equiv \delta n$, $\delta\tilde{T}(q,t) \equiv \delta\tilde{T}$, $\delta Q_\eta(q,t) \equiv \delta Q_\eta$ and δQ_κ, we have

$$\delta\ddot{n} = -\omega_T^2(\delta n + \delta\tilde{T}) + \delta Q_\eta \tag{5.12}$$

$$\delta\dot{Q}_\eta = -\frac{1}{\tau_\eta}\delta Q_\eta - \Omega_\eta^2\delta\dot{n} \tag{5.13}$$

$$\delta\dot{\tilde{T}} = \epsilon_{LP}\delta\dot{n} + \delta Q_\kappa \tag{5.14}$$

$$\delta\dot{Q}_\kappa = -\frac{1}{\tau_\kappa}\delta Q_\kappa - \Omega_\kappa^2\delta\tilde{T} \tag{5.15}$$

where

$$\omega_T \equiv c_T q \tag{5.16}$$

$$\Omega_\eta^2 \equiv \frac{4}{3}\frac{p}{m n_0} q^2 \tag{5.17}$$

$$\Omega_\kappa^2 \equiv \frac{5}{2}\frac{k_B}{m}\frac{p}{n_0 c_{V_1}} q^2 \tag{5.18}$$

Because we are working with unitary Fermi gas, using Eq. 4.15 and taking $\epsilon_F(n) = m v_F^2/2$, v_F is the Fermi speed, we have

$$\Omega_\eta^2 \equiv \frac{4}{15}\omega_F^2 f_E(\theta), \tag{5.19}$$

where we define $\omega_F \equiv v_F q$. Similarly, we can write

$$\Omega_\kappa^2 \equiv \frac{1}{2}\frac{k_B}{c_{V_1}}\omega_F^2 f_E(\theta). \tag{5.20}$$

In the short relaxation time limit, we see that $\delta Q_\eta \to -\gamma_\eta \delta \dot{n}$, with $\gamma_\eta \equiv \tau_\eta \Omega_\eta^2 = \frac{4\eta}{3n_0 m} q^2$ and $\delta Q_\kappa \to -\gamma_\kappa \delta \tilde{T}$, with $\gamma_\kappa \equiv \tau_\kappa \Omega_\kappa^2 = \frac{\kappa_T}{n_0 c_{V_1}} q^2$, reproducing the results in [Wang et al. (2022)].

We limit the spatial region for Fourier transform to the region near the center of the box, where the variation of background density is small, less than 15%. And we choose exact integer number of spatial periods so that the imaginary part of Fourier transform is consistent and negligible. After release from the initial condition, it only takes a few ms for the density variation to decay completely. This rather short evolution time scale makes sure that the box potential has negligible contribution to the time dependent density profile in the region of interest, so that we can ignore it safely.

The four coupled differential equations can be easily solved to determine $\delta n(q,t)$ with the initial conditions $\delta n(q,0) = A, \delta \tilde{T}(q,0) = 0, \delta Q_\eta = 0$, and $\delta Q_\kappa = 0$. The data are fitted with initial amplitude A, the isothermal sound frequency ω_T, and relaxation times τ_η, τ_κ as free parameters.

The data shown in Figures 5.5 and 5.6 are experiments done with four different perturbation wavelengths. The blue dots are measured data with error bars. The corresponding color curve are best fit with minimized χ^2. We perform the simulation with MATLAB built-in solver ODE 45 to solve theses second-order differential equation numerically. As discussed before, we vary A, ω_T, τ_η and τ_κ as the fitting parameters to run χ^2 search for the global minimum. The obtained isothermal sound frequency $\omega_T = c_T q$ determine the reduced temperature $\theta(c_T/v_F)$ as we discussed in chapter four.

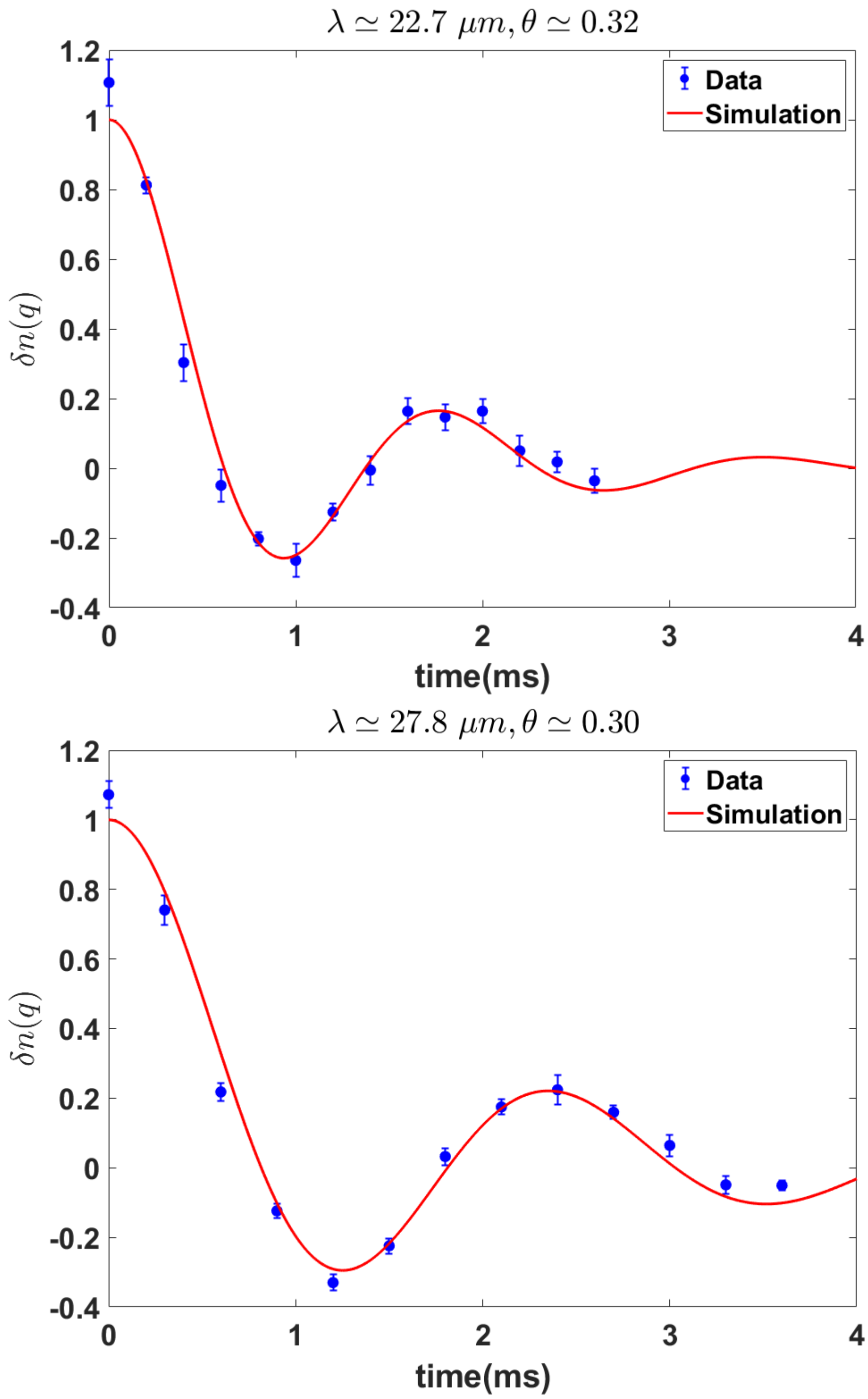

Figure 5.5: Fourier component of the density perturbation $\delta n(q,t)$ with $q = 2\pi/\lambda$, for wavelength $\lambda = 22.7\ \mu$m (upper) and $\lambda = 27.8\ \mu$m (lower), at reduced temperatures $\theta \simeq 0.32$ and $\theta \simeq 0.30$, respectively. Blue dots are data with errorbars. Red solid curves are fitting to the kinetic relaxation model.

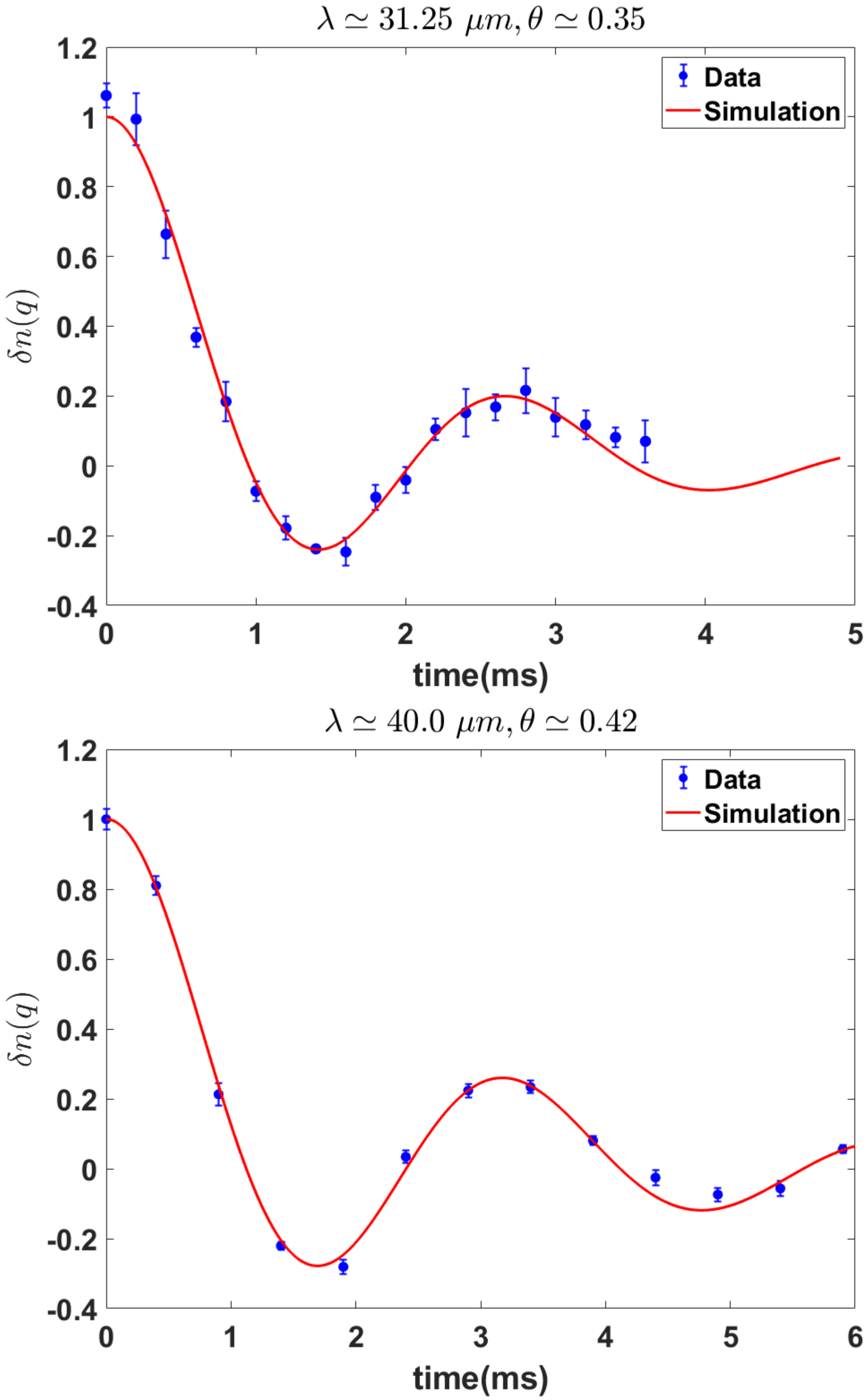

Figure 5.6: Fourier component of the density perturbation $\delta n(q,t)$ with $q = 2\pi/\lambda$, for wavelength $\lambda = 31.25$ μm (upper) and $\lambda = 40.0$ μm (lower), at reduced temperatures $\theta \simeq 0.35$ and $\theta \simeq 0.42$, respectively. Blue dots are data with errorbars. Red solid curves are fitting to the kinetic relaxation model.

5.4 Analytic solution

The fitting also give us the analytic solutions for all of the responses $\delta n(q,t), \delta\tilde{T}(q,t), \delta Q_\eta(q,t)$ and $\delta Q_\kappa(q,t)$. For each response, we can obtain analytic solution that determines the contributions of 4 different modes, as shown in Figure 5.7 for the density and temperature response. Here, we use data at $\lambda = 37.0\ \mu$m, $\theta = 0.37$ as an example. Two fast modes (purple) arise predominately from relaxation of the viscous force and heat current to their Navier-Stokes forms on time scales of τ_η and τ_κ. A zero-frequency thermally-diffusive mode (orange) decays at a rate determined by τ_κ, which controls the effective frequency dependent thermal conductivity. Finally, an oscillating first sound mode (blue) decays at a rate determined by τ_η and τ_κ, which control the effective frequency dependent sound diffusivity.

For the density perturbation, the fast modes contribute only 1% at $t = 0$, and are multiplied by a factor of 10 in Figure 5.7 to make them visible. The thermally diffusive mode contributes $\simeq$ 35% to the density perturbation, while the first sound mode contributes $\simeq$ 65%. For this reason, the fit parameters, comprising the frequency ω_T and the transport times τ_η and τ_κ , which determine the oscillation frequency and decay rates of the two dominant modes, are nearly independent, simplifying the fit procedure.

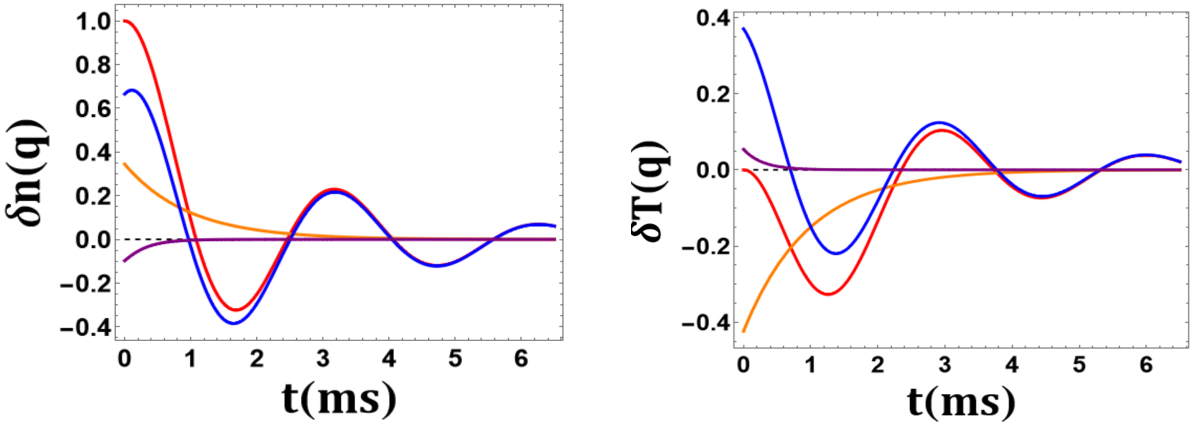

Figure 5.7: Density and temperature response for $T/T_F \simeq 0.37$ and $\lambda \simeq 37.0\ \mu$m showing the mode content. First sound mode (blue), thermally diffusive mode (orange), fast relaxation mode (purple). The fast relaxation modes are increased ×10 in the density response to make them visible, ×1 in temperature response.

In contrast to the density response, the fast modes contribute significantly $\simeq$ 10% to the short time response of the temperature perturbation, shown ×1 in Figure.. and more significantly 30% to the short time response of the viscous force and heat current, shown ×1 in Figure 5.8

We display δQ_η in units of $\omega_F^2 \delta n(q,0) = \omega_F^2$ as seen in Eq. 5.8. Similarly, Eq. 5.10 shows that the natural scale for δQ_κ is $\delta \dot{n}(q,t)$. We display δQ_κ in units of $\omega_F \delta n(q,0) = \omega_F$.

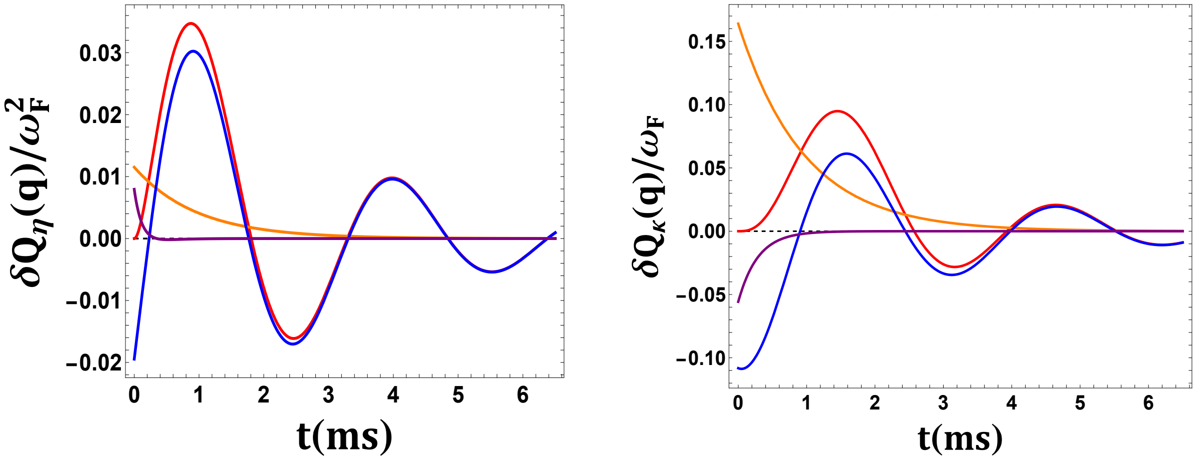

Figure 5.8: Viscous force and heat current response for $T/T_F \simeq 0.37$ and $\lambda \simeq 37.0\ \mu$m showing mode content. First sound mode (blue), thermally diffusive mode (orange), fast relaxation mode (purple).

Figure 5.9 shows the difference (red) between the fast relaxation approximation (blue) and the kinetic theory relaxation model (orange). We see that the deviation from the fast relaxation (long-wavelength) approximation is significant, emphasizing the need for the analysis based on the relaxation model. With the new kinetic theory model, the finite relaxation time corrections to the transport properties are included in the analysis, enabling determination of the static transport properties, as discussed in chapter 6.

5.5 Stored energy

In this section, we estimate the change in the energy per particle W_1 that arises from the energy stored in the initial spatially periodic density profile. This stored energy is converted to kinetic energy after the perturbation is extinguished and finally into heat. To show that the change in the average energy per particle is negligible, we determine the stored energy W for the ideal case of an adiabatic change of the density, δn, starting from a uniform density n_0. As the total number of atoms does not change during the compression, we must have

$$\int d^3\mathbf{r}\,\delta n(\mathbf{r}) = 0, \tag{5.21}$$

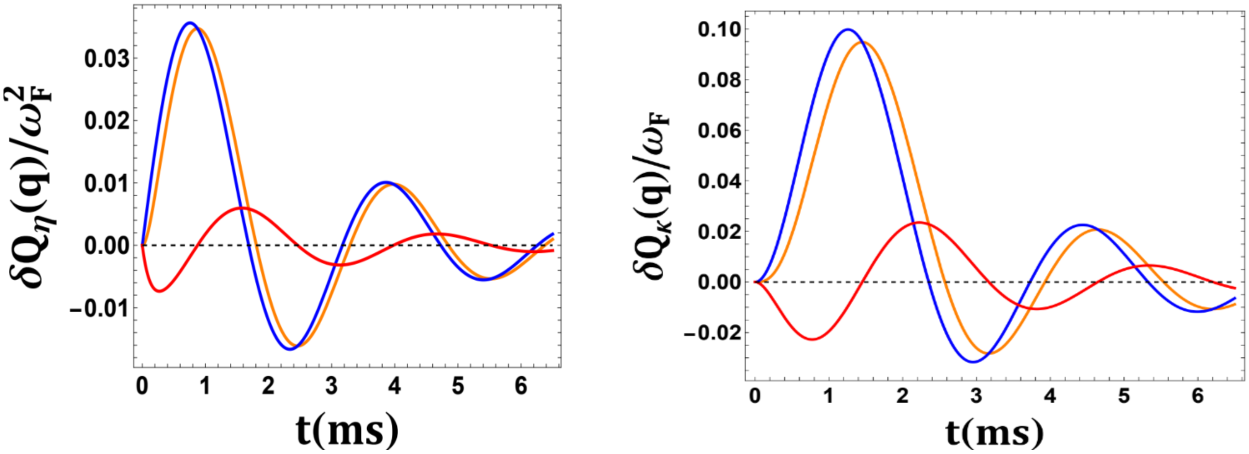

Figure 5.9: Difference (red) between the fast relaxation approximation (blue) and kinetic theory model (orange) for the viscous force (left) and heat current (right) with $T/T_F \simeq 0.37$ and $\lambda \simeq 37.0\ \mu$m.

Now consider a small volume ΔV of the cloud, containing a small number of atoms $\Delta N = n\Delta V$. Changing the volume for fixed ΔN, we have $d\Delta N = dn\Delta V + nd\Delta V = 0$. Taking $n \simeq n_0$, the density before perturbation is applied, we have

$$d\Delta V = -\Delta V \frac{dn}{n_0} \tag{5.22}$$

The work to change ΔV by $d\Delta V$ is just

$$d\Delta W = -p\, d\Delta V = (p_0 + \delta p)\Delta V \frac{dn}{n_0} \tag{5.23}$$

Then the net work to change the local density from n_0 to n is

$$\Delta W = \Delta V \int_{n_0}^{n} \frac{dn}{n_0}(p_0 + \delta p) \tag{5.24}$$

For the integration variable, we use the local change in density $\delta n \equiv n - n_0, dn = d\delta n$. Assuming an adiabatic change in pressure, $p - p_0 \equiv \delta p = mc_S^2\delta n$, with c_S the adiabatic sound speed and p_0 the uniform background pressure, we have

$$\Delta W = \Delta V \int_0^{n_0} \frac{d\delta n'}{n_0}(p_0 + mc_S^2\delta n') = \Delta V\left(\delta n \frac{p_0}{n_0} + mc_S^2 \frac{(\delta n)^2}{2n_0}\right) \tag{5.25}$$

Replacing the local volume ΔV by $d^3\mathbf{r}$, we have for the total stored energy

$$W = \int d^3\mathbf{r}\left(\delta n \frac{p_0}{n_0} + m c_S^2 \frac{(\delta n(\mathbf{r}))^2}{2n_0}\right) \simeq \frac{m c_S^2}{2} \int d^3\mathbf{r}\; n_0 \left[\frac{\delta n(\mathbf{r})}{n_0}\right]^2 \tag{5.26}$$

In Eq. 5.26, since the background pressure p_0 and density n_0 are spatially uniform, Eq. 5.22 requires that the term linear in δn vanish. For simplicity,we ignore the spatial variation of sound speed c_S and background density n_0 in the region of interest. Defining the stored energy per particle W_1 in terms of the mean square fractional density perturbation, we have finally,

$$W_1 = \frac{m c_S^2}{2} \left\langle \left[\frac{\delta n(\mathbf{r})}{n_0}\right]^2 \right\rangle . \tag{5.27}$$

The same result can be obtained by finding the rate of change of the total kinetic energy K from the dissipationless equation of motion $n_0 m \partial_t \mathbf{v} = -\nabla \delta p$, which yields $\partial_t(K+W)=0$, so that W is the effective potential energy. Note that for a unitary Fermi gas, $m c_S^2 = 10E_1/9$ from Eq. 4.18, where E_1 is the energy per particle. Therefore for a sinusoidal perturbation with a 20% amplitude, $\langle [\delta n(\mathbf{r})/n_0]^2 \rangle \simeq (0.2)^2 \times \langle \sin^2(\mathbf{r}) \rangle = (0.2)^2 \times \frac{1}{2}$, which gives $W_1 \simeq 0.01 E_1$. W_1 is negligible.

CHAPTER

6

EXPERIMENTAL RESULTS

In this chapter I present the experiment results of the relaxation time measurement and corresponding transport coefficients [Li et al. (2024)]. In particular, the measured relaxation times directly determine the universal density shift coefficients for the static shear viscosity and thermal conductivity. The current experiment results are compared with results from a previous experiment [Wang et al. (2022)]. In addition, I discuss the Drude model correction for the previous experiment, which serves as a relatively crude way to estimate the deviation of measured transport properties from their static values. The Drude corrected results for previous experiment are compared with current results to show the consistency. Finally we compare our results of sound diffusivity measurement with the results from MIT group [Patel et al. (2020)].

6.1 Measured static transport properties

The two relxation times τ_η and τ_κ are determined from the fit. The static shear viscosity is given in units of $\hbar n_0$ by

$$\eta = \tau_\eta p = \alpha_\eta \hbar n_0 \tag{6.1}$$

Eq 4.15 for p gives the dimensionless shear viscosity coefficient,

$$\alpha_\eta = \frac{2\pi}{5}\frac{\tau_\eta}{\tau_F} f_E(\theta) \tag{6.2}$$

Here we define the Fermi time τ_F as the time for an atom to move a Fermi wavelength λ_F at Fermi speed v_F. With $\lambda_F = 2\pi\hbar/(m v_F)$, and $m v_F^2 = 2\epsilon_F$, the Fermi time is

$$\tau_F = \frac{\pi\hbar}{\epsilon_F} \tag{6.3}$$

Similarly, the static thermal conductivity is given in units of $\hbar n_0 k_B/m$ by

$$\kappa_T = \frac{5}{2}\frac{k_B}{m}\tau_\kappa p = \alpha_\kappa \frac{k_B}{m}\hbar n_0 \tag{6.4}$$

where the dimensionless thermal conductivity coefficient is

$$\alpha_\kappa = \pi\frac{\tau_\kappa}{\tau_F} f_E(\theta) \tag{6.5}$$

In order to compare with the static transport properties, we parameterize α_η as

$$\alpha_\eta = \alpha_{3/2}\theta^{3/2} + \alpha_{2\eta} \tag{6.6}$$

Here, the first term is high temperature limit, which is obtained from a virational calculation [Bruun and Smith (2007)], $\alpha_{3/2} = 45\pi^{3/2}/(64\sqrt{2}) = 2.76849 \simeq 2.77$ and $\alpha_{2\eta}$ is the universal density shift coefficient, which is used as a fit parameter. Similarly, we parameterize α_κ as

$$\alpha_\kappa = \frac{15}{4}(\alpha_{3/2}\theta^{3/2} + \alpha_{2\kappa}) \tag{6.7}$$

Here, the leading factor of 15/4 is chosen to yield the correct high temperature limit for the ratio κ_T/η. In this limit, Eqs. 6.5 and 6.7 yield $\kappa_T = \frac{15}{4}\frac{k_B}{m}$, where we have used $\tau_\kappa/\tau_\eta = 3/2$ in the high temperature Boltzmann limit[Frank et al. (2020)]. One can show that it holds for any isotropic collision cross section $d\sigma/d\Omega$.

With Eqs. 6.6 and 6.7, the relaxation times are then parameterized by inverting Eqs. 6.2 and 6.5 as

$$\frac{\tau_\eta}{\tau_F} = \alpha_\eta \frac{5}{2\pi}\frac{1}{f_E(\theta)} \tag{6.8}$$

and

$$\frac{\tau_\kappa}{\tau_F} = \alpha_\kappa \frac{1}{\pi}\frac{1}{f_E(\theta)} \tag{6.9}$$

Figures. 6.1 and 6.2 show the extracted relaxation time τ_η for shear viscosity and τ_κ for thermal conductivity, in units of the Fermi time τ_F, as function of reduced temperature $\theta = T/T_F$. The red dashed curves are predicted high-temperature limit, i.e. $\alpha_{2\eta} = 0, \alpha_{2\kappa} = 0$. The measured relaxation times are on the order of one Fermi time τ_F, significantly deviating from this high-T limit. The red solid curves are fitting with Eqs. 6.8 and 6.9 with $\alpha_{2\eta}$ and $\alpha_{2\kappa}$ obtained from the static transport fits. From this we can see the density-shift coefficients $\alpha_{2\eta}$ and $\alpha_{2\kappa}$ are sensitive to the finite relaxation times. For τ_η/τ_F, the fit to Eq. 6.8 gives the density-shift coefficient $\alpha_{2\eta} = 0.45(04)$; For τ_κ/τ_F, the fit to Eq. 6.9 gives the density-shift coefficient $\alpha_{2\kappa} = 0.22(03)$.

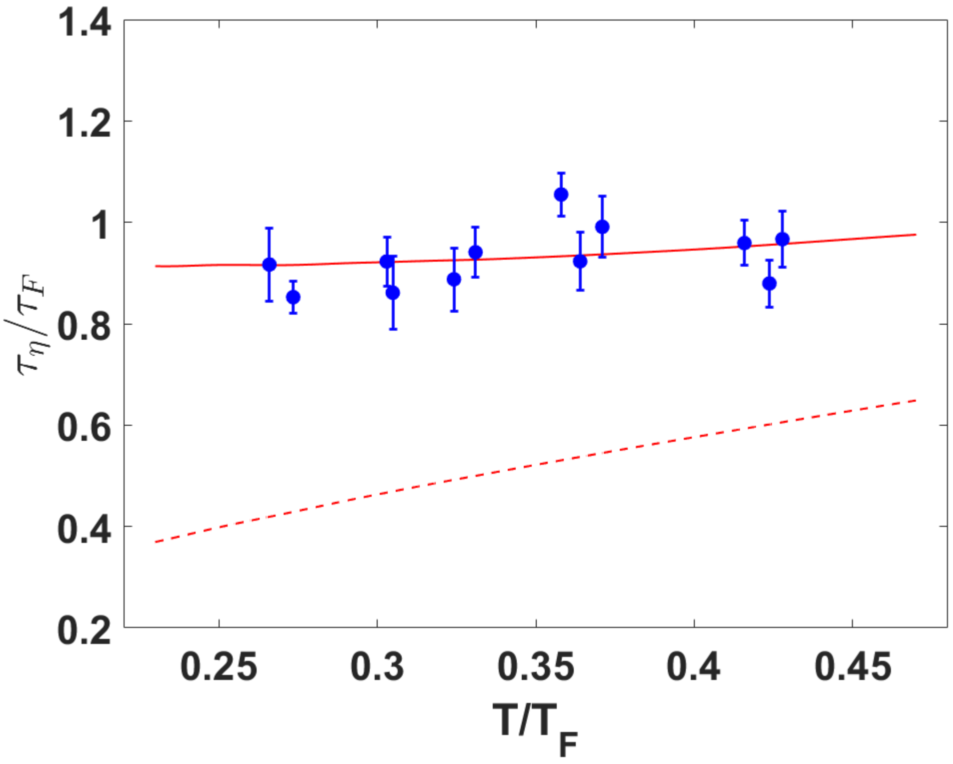

Figure 6.1: Relaxation time τ_η in units of Fermi time τ_F as a function of T/T_F. Red solid curve is fitting to Eq. 6.8 with $\alpha_{2\eta} = 0.45$, red dashed curve is the high temperature limit,where $\alpha_{2\eta} = 0$.

One of the major advantages of current optical setup is that we can reliably project essentially any wavelength of perturbation with the third DMD. Figures 6.3 and 6.4 shows τ_η/τ_F and τ_κ/τ_F as a function of wavelengths for roughly the same $T/T_F \simeq 0.3$. One can see for different wavelengths, ranging from 22μm to 40μm, τ_η/τ_F and τ_κ/τ_F shows negligible λ-dependence as expected.

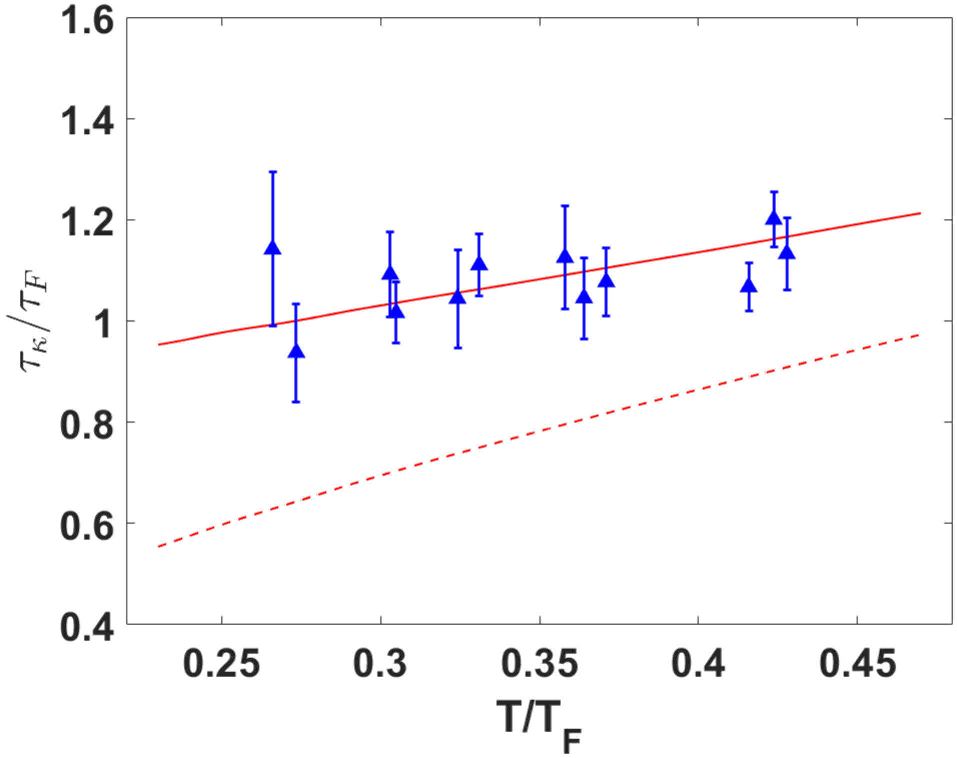

Figure 6.2: Relaxation time τ_κ in units of Fermi time τ_F as a function of T/T_F. Red solid curve is fitting to Eq. 6.9 with $\alpha_{2\kappa} = 0.22$, red dashed curve is the high temperature limit, where $\alpha_{2\kappa} = 0$.

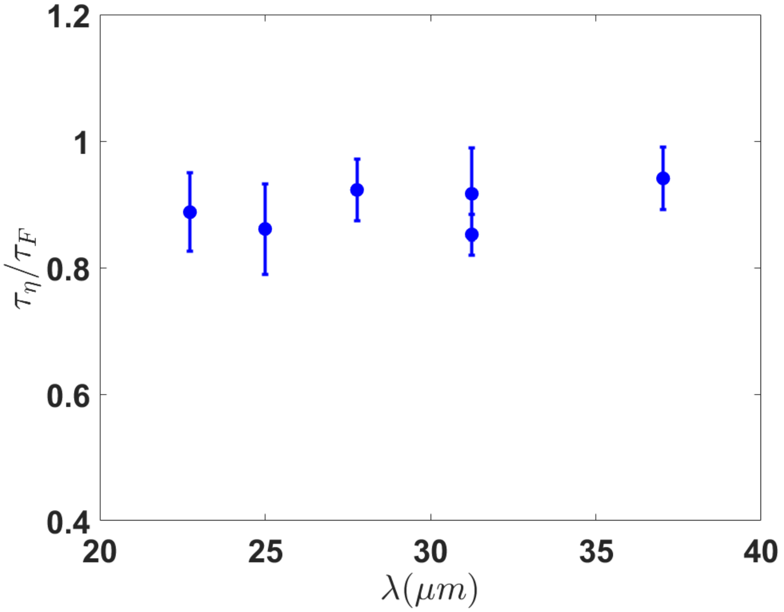

Figure 6.3: Relaxation time τ_η in units of Fermi time τ_F as a function of perturbation wavelength λ.

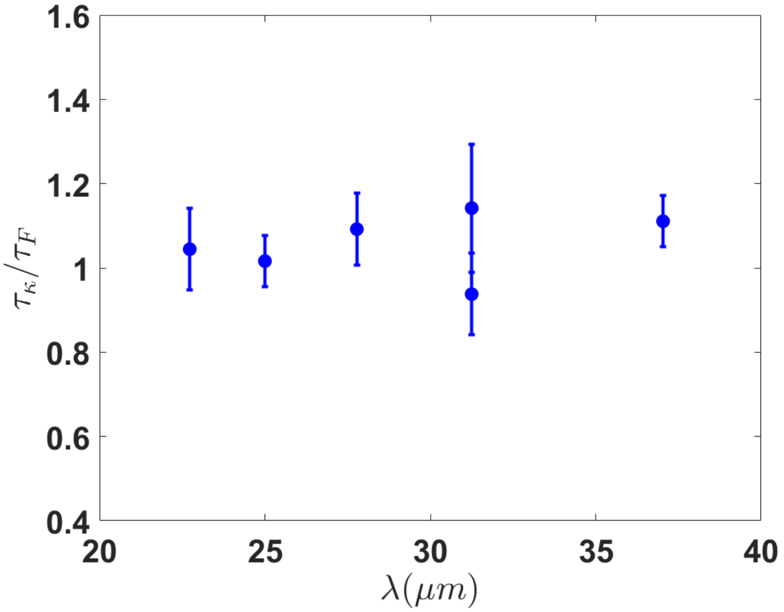

Figure 6.4: Relaxation time τ_κ in units of Fermi time τ_F as a function of perturbation wavelength λ.

Due to experimental constraint, the highest reduced temperature we can reach without loss of atoms in purpose is around $\theta \simeq 0.43$. At this point, we got $\tau_\kappa/\tau_\eta \simeq 1.2$, deviating significantly from the high-T limit (dashed curves), where $\tau_\kappa/\tau_\eta = 3/2$ [Frank et al. (2020)].

The measured τ_η is then used to determine the static shear viscosity and thermal conductivity with Eqs 6.1 and 6.4. Pressure p is determined by Eq 4.15. Figure 6.5 is the extracted dimensionless shear viscosity (blue dots) plotted as a function of reduced temperature θ. The red solid curve is fit with Eq. 6.6, where $\alpha_{3/2} = \frac{45\pi^{3/2}}{64\sqrt{2}} \simeq 2.77$ [Bruun and Smith (2007); Braby et al. (2010); Bluhm et al. (2017)]. The density shift coefficient is the only fit parameter here, corresponding to the fitting for τ_η/τ_F, it also yields $\alpha_{2\eta} = 0.45(04)$. The red dashed curve is the high temperature limit, i.e. $\alpha_{2\eta} = 0$.

Similarly, the measured τ_κ determines the static thermal conductivity with Eq. 6.4. Figure 6.6 is the extracted dimensionless thermal conductivity versus reduced temperature θ. The red solid curve is fit with Eq. 6.7 with $\alpha_{2\kappa}$ the only fitting parameter, yielding $\alpha_{2\kappa} = 0.22(03)$, i.e., the shift is $15/4 \times 0.22$ in units of $n_0\hbar k_B/m$. The red-dashed curve is again the high temperature limit, i.e., $\alpha_{2\kappa} = 0$.

The measured relaxation times τ_η and τ_κ determine the first sound diffusivity [Landau and

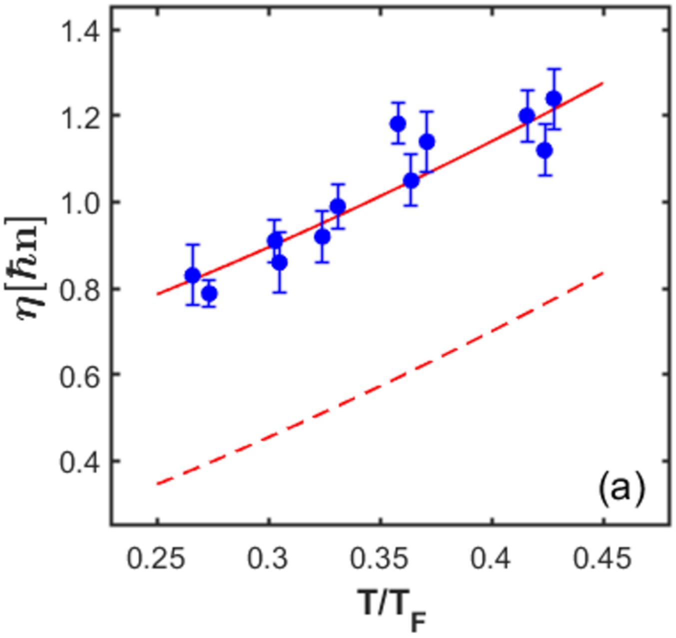

Figure 6.5: Measured dimensionless shear viscosity α_η (blue dots) versus reduced temperature $\theta \equiv T/T_F$.

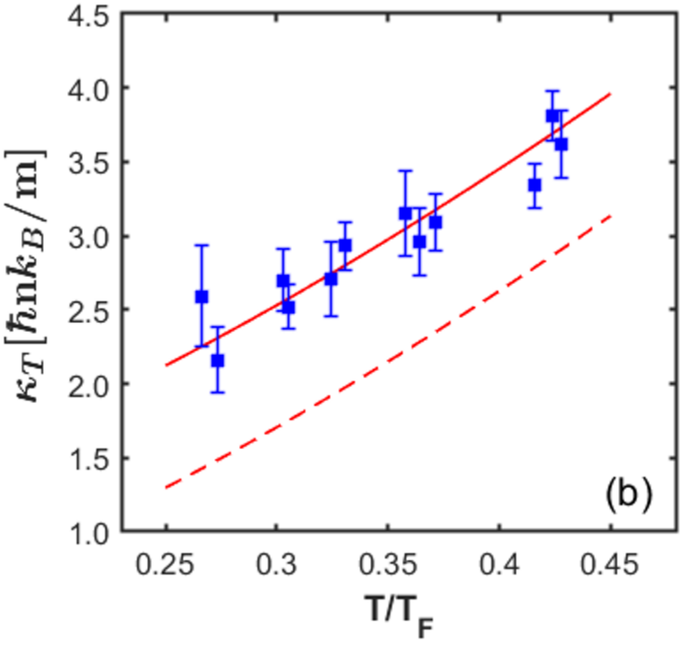

Figure 6.6: Measured dimensionless thermal conductivity α_κ (blue dots) versus reduced temperature $\theta \equiv T/T_F$.

Lifshitz (2013)] D_1 in units of $\hbar/m$

$$\frac{D_1}{\hbar/m} = \frac{8\pi}{15}\frac{\tau_\eta}{\tau_F} f_E(\theta) + \frac{2\pi}{3}\frac{\tau_\kappa}{\tau_F}\theta \tag{6.10}$$

Figure 6.7 is the plot of D_1 in units of $\hbar/m$, as a function of θ. The red solid curve is the fit with static shear viscosity and thermal conductivity, substitute Eqs. 6.8 and 6.9, we have

$$\frac{D_1}{\hbar/m} = \frac{4}{3}\alpha_\eta + \frac{5}{2}\frac{\theta}{f_E(\theta)}\alpha_\kappa \tag{6.11}$$

With our measured density shift coefficients, it becomes

$$\frac{D_1}{\hbar/m} = \frac{4}{3}(2.77\theta^{3/2} + 0.45) + \frac{5}{2}\frac{\theta}{f_E(\theta)}(2.77\theta^{3/2} + 0.22) \tag{6.12}$$

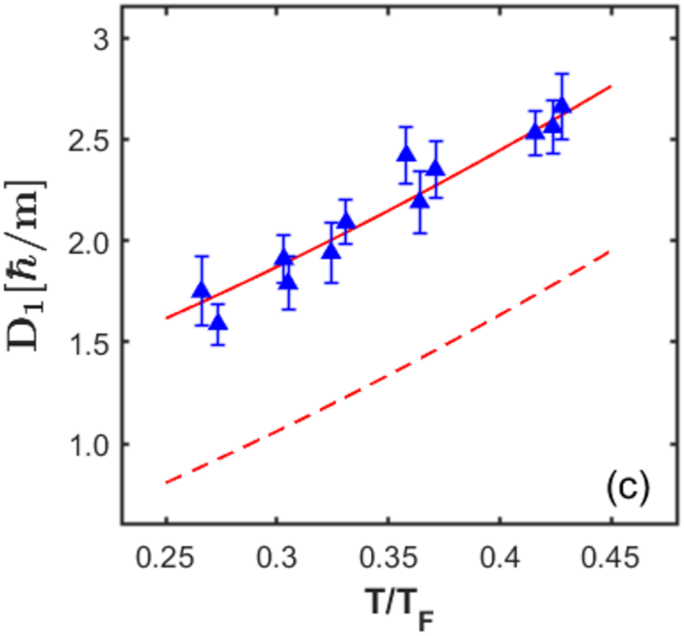

Figure 6.7: Measured first sound diffusivity D_1 (blue dots) versus reduced temperature $\theta \equiv T/T_F$.

The extracted first sound diffusivity D_1 can be used to compare with the MIT group's sound attenuation measurement at normal fluid regime. Figure 6.8 is the plot of our sound diffusivity data (blue) and the sound diffusivity data measured from sound attenuation by Martin Zwierlein's group (orange) [Patel et al. (2020)]. We see that the high temperature behavior obtained from Eq.6.11 using the fitted density shifted coefficients for the shear viscosity and thermal conductivity, Eq.6.12, is in good agreement with the sound attenuation measurements. However, the lower temperature measurements of sound diffusivity in [Patel et al. (2020)], still in normal fluid regime, exhibit a nearly constant upward shift relative to our relaxation time measurements.

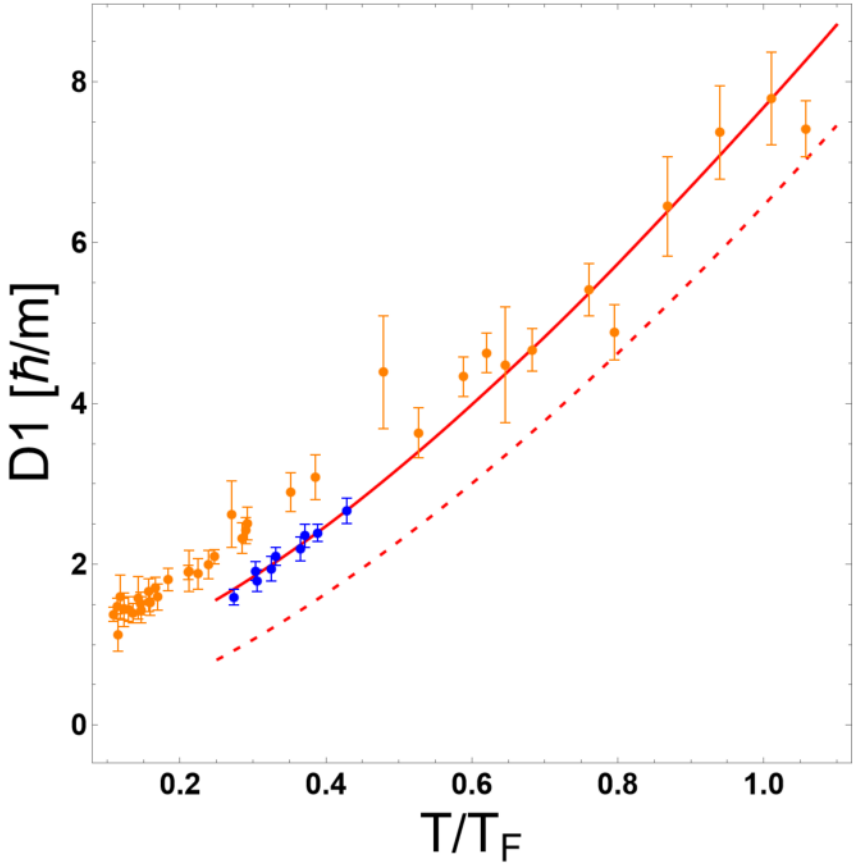

Figure 6.8: Measured first sound diffusivity D_1 (blue dots) from Eq. 6.10, in units of $\hbar/m$ versus reduced temperature $\theta \equiv T/T_F$. Red solid curve is from Eq. 6.12. Red-dashed curve (high temperature limit): $f_E(\theta) \to 5\theta/2$, $D_1[\hbar/m] = 7/3 \times 2.77\theta^{3/2}$. Sound diffusivity data of [Patel et al. (2020)] (orange dots). Error bars (blue dots) are statistical.

6.2 Comparison to Drude model

In this part, we estimate the static transport coefficients from our measured values at finite frequencies by applying a simple Drude model correction. Here we compare our direct static transport properties measurements with the Drude model corrected results from previous experiment to show some consistency. Before doing that, we need to point out that the Drude model is not a rigorous way to correct the results. Because the Drude model is merely a crude estimate for the second order hydrodynamic effects, and it has not been proved to be true for the strongly interacting Fermi gas in normal fluid regime where the data are taken. Nevertheless, it still provides certain insights of how breakdown of first order hydrodynamics could effect the measured results, and also to estimate the extreme cases of possible corrections to the hydrodynamic relaxation model. More importantly, by comparing our current results with the Drude corrected results, we justify the necessity of explicitly incorporating the finite relaxation times in our hydrodynamic model.

In our previous hydrodynamic relaxation model [Wang et al. (2022)], where the relaxation times assumed to be negligible, we have

$$\delta\ddot{n} = c_T^2\partial_z^2(\delta n + \delta\tilde{T}) + \frac{4\eta}{3n_0 m}\partial_z^2\delta\dot{n} \tag{6.13}$$

$$\delta\dot{\tilde{T}} = \epsilon_{LP}\delta\dot{n} + \frac{\kappa_T}{n_0 c_V}\partial_z^2\delta\tilde{T} \tag{6.14}$$

Fitting this model to the data in the Fourier space gave us η and κ_T measured at finite frequency ω. In the Drude approximation [Braby et al. (2011); Enss (2012)], the shear viscosity measured at finite frequency $\eta(\omega)$ is related to the static one $\eta(0)$ by

$$\eta(\omega) = \frac{\eta(0)}{1+(\omega\tau_\eta)^2} \tag{6.15}$$

similarly, for thermal conductivity

$$\kappa_T(\omega) = \frac{\kappa_T(0)}{1+(\omega\tau_\kappa)^2} \tag{6.16}$$

To estimate the correction, we make the approximation $\omega \simeq \omega_S$, the adiabatic sound frequency with spatial period λ, which equals $(2\pi/\lambda)c_S(\theta)$. The adiabatic sound speed c_S is determined from Eq. 4.19, where $f_E(\theta)$ is the universal, dimensionless function for unitary Fermi gas that can be determined with measured Equation of State (EoS) [Ku et al. (2012)], $v_F = \sqrt{2\epsilon_F/m}$ is the Fermi speed. Now, Eqs. 6.8 and 6.9 relate the relaxation time τ_η and τ_κ to the static shear viscosity and thermal conductivity $\alpha_\eta(0)$ and $\alpha_\kappa(0)$ [1], we find

$$\omega_S \tau_\eta \simeq 5\pi \sqrt{\frac{2\hbar^2}{3m\lambda^2 \epsilon_F(n)} \frac{\alpha_\eta(0)}{\sqrt{f_E(\theta)}}} \tag{6.17}$$

and

$$\omega_S \tau_\kappa \simeq 2\pi \sqrt{\frac{2\hbar^2}{3m\lambda^2 \epsilon_F(n)} \frac{\alpha_\kappa(0)}{\sqrt{f_E(\theta)}}} \tag{6.18}$$

Here, $\alpha_\eta(0)$ and $\alpha_\kappa(0)$ are static dimensionless shear viscosity and thermal conductivity for a known θ, i.e. $\omega = 0$. With Eqs. 6.15 and 6.16, the measured dimensionless shear viscosity $\alpha_\eta(\omega_S)$ is related to $\alpha_\eta(0)$ by

$$\alpha_\eta(0) = [1 + (\omega_S \tau_\eta)^2]\, \alpha_\eta(\omega_S) \tag{6.19}$$

Similarly, for thermal conductivity

$$\alpha_\kappa(0) = [1 + (\omega_S \tau_\kappa)^2]\, \alpha_\kappa(\omega_S) \tag{6.20}$$

Substitute Eqs. 6.17 and 6.18 into Eqs. 6.19 and 6.20, we can solve for the two static transport coefficients, $\alpha_\eta(0)$ and $\alpha_\kappa(0)$ for a particular reduced temperature θ.

In Figures 6.9 and 6.10, we plot the previous measured dimensionless shear viscosity α_η and thermal conductivity α_κ in [Wang et al. (2022)] (black triangles), together with the corrected value by applying the Drude model (Purple triangles) and the current experiment's data from Figures. 6.5 and 6.6 (Blue circles). For the shear viscosity, Figure 6.9, we can see that in the relatively low temperature regime, $\theta \leq 0.35$, there is no significant deviation between the new data (blue circle) and previous measured values (black triangle). The correction from Drude model is small, which is expected because at low temperature, the gas is colder and the density is high, both the relaxation time τ and sound frequency ω decreasing, so that we are more in the fast relaxation regime. Therefore the correction is not significant. As θ increases, we can clearly see that the previous results from the fast relaxation model are lower than the results from our new relaxation model, and the Drude model correction for the previous results is also significantly larger. One can also see that the corrected values agree with our new data and the fitting to the high temperature regime.

The difference between the new results and previous results are more obvious in the thermal conductivity measurement shown in Figure 6.10. At $\theta \leq 0.35$, the new results (blue circles) and the corrected value of previous results (purple triangles) agree very well, but for higher temperature, the previous results obtained from fast relaxation deviate significantly from our

---

[1] The α_η and α_κ in Eqs. 6.8 and 6.9 are static shear viscosity and thermal conductivity, i.e. $\alpha_\eta(0)$ and $\alpha_\kappa(0)$.

new results. Even the corrected value are downshifted relative to our new results and fits to the high temperature regime.

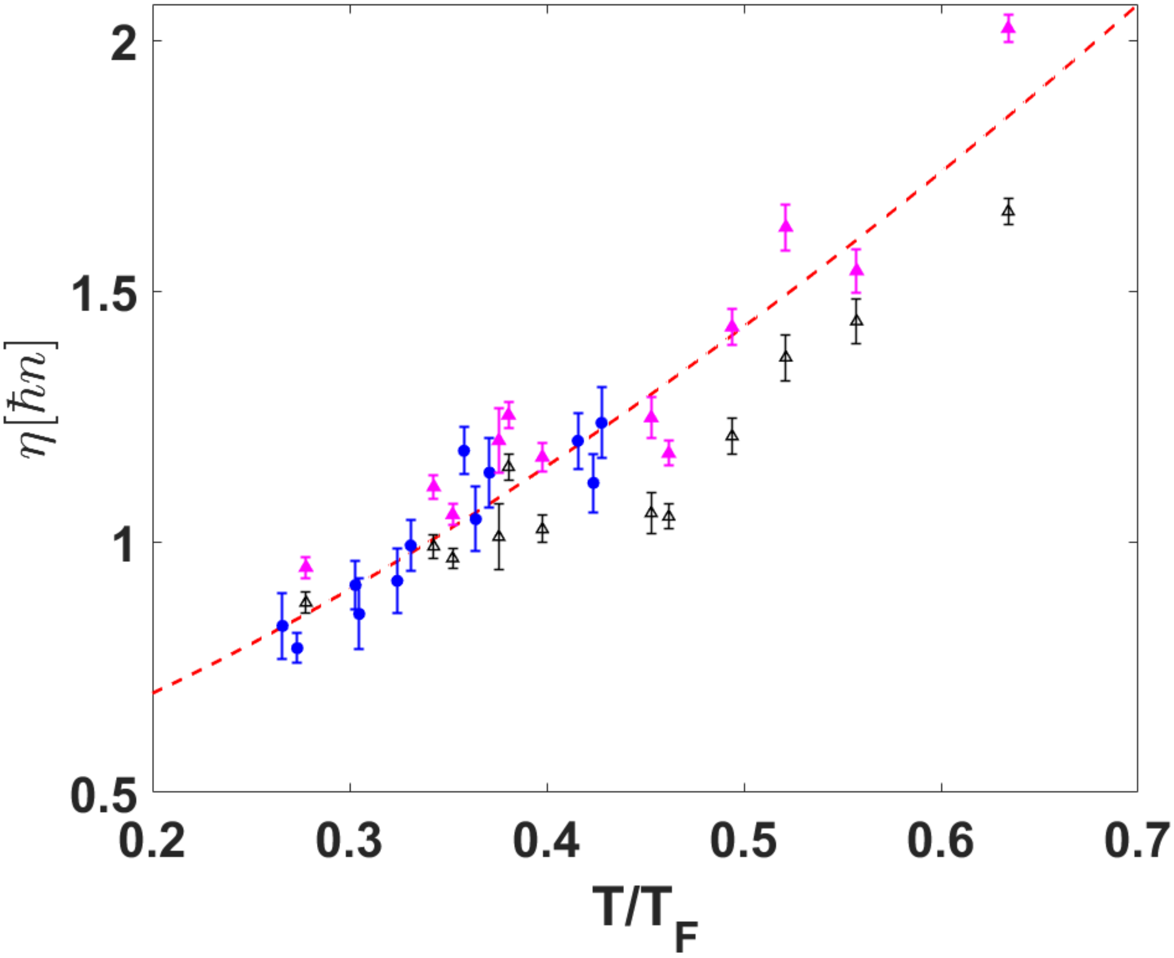

Figure 6.9: Measured shear viscosity and results from previous experiment. Blue circles are data from current experiment as in Figure 6.5. Black triangles are the measured shear viscosity from previous experiment [Wang et al. (2022)], purple triangles are the corrected value for Black triangle data by applying Drude model. Red dashed curve is $\alpha_\eta = 2.77\theta^{3/2} + 0.45$.

This crosscheck with the Drude model correction justifies the validity of our new kinetic model and experimental results. We also found that the latest results for shear viscosity and thermal conductivity are more self-consistent. The measured transport coefficients agree better with the leading $T^{3/2}$ prediction, compare to previous experiment results. This is another proof of properly counting the effects of finite relaxation times.

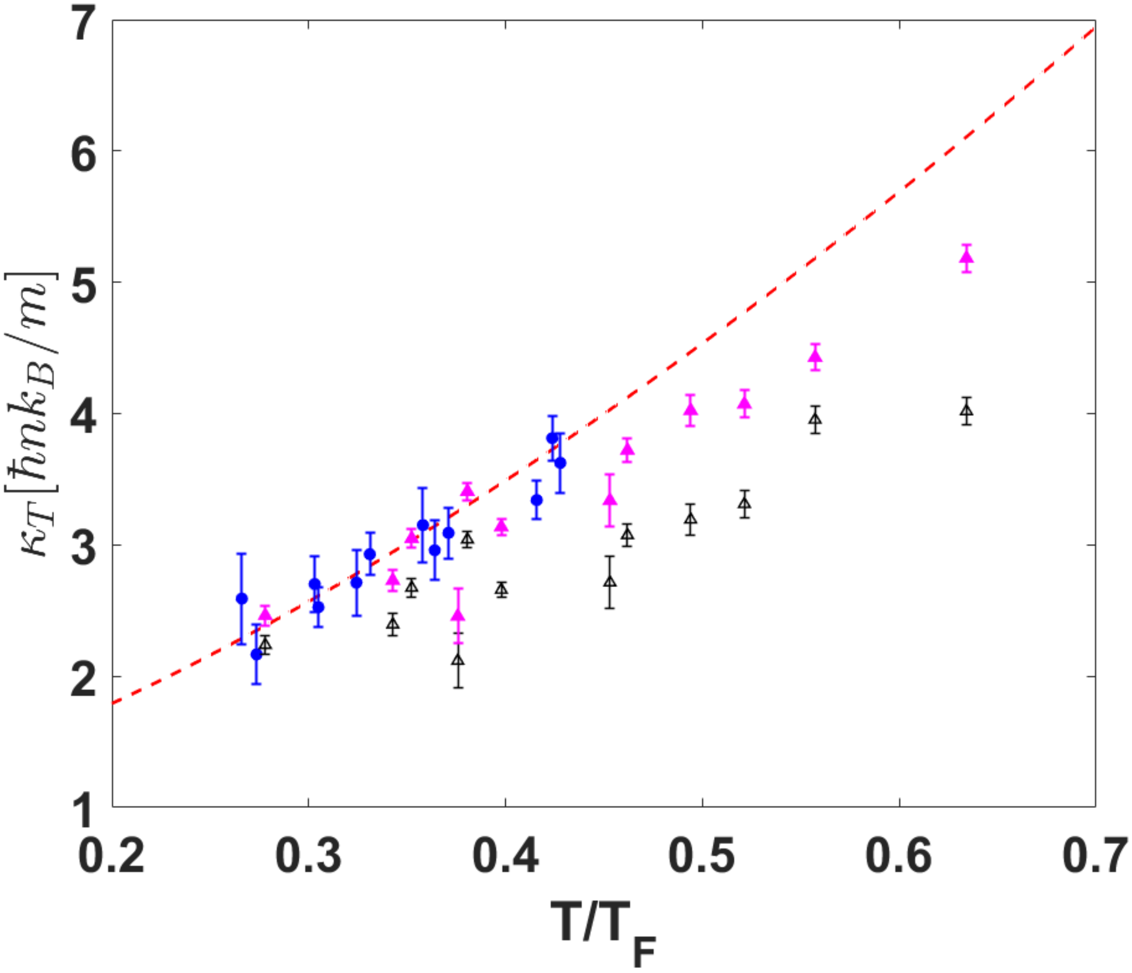

Figure 6.10: Measured thermal conductivity and results from previous experiment. Blue circles are data from current experiment as in Figure 6.6. Black triangles are the measured thermal conductivity from previous experiment [Wang et al. (2022)], purple triangles are the corrected value for Black triangle data by applying Drude model. Red dashed curve is $\alpha_\kappa = \frac{15}{4}(2.77\theta^{3/2}+0.22)$.

CHAPTER

7

CONCLUSION

7.1 Summary

We have developed a new method to measure the universal density shift coefficients for static shear viscosity and thermal conductivity of the unitary Fermi gas at normal fluid regime. By implementing the third DMD to independently control the repulsive perturbation, the experiments were performed with a better controlled and more precise procedure than the former experiment [Wang et al. (2022)]. This new system allows us to explore any wavelength-dependence of the measured transport properties.

On the theory side, we found that the previous fast relaxation model is inadequate to measure the static transport properties. The assumption that the system instantly relaxes to local thermal equilibrium ,i.e. $\tau_\eta = \tau_\kappa = 0$, is incorrect. The new experiment explicitly measured the two relaxation times τ_η and τ_κ, for shear viscosity η and thermal conductivity κ_T. We found that τ_η and τ_κ are indeed small, compare to the time scale for the density variation to decay, which is several miliseconds, but definitely not negligible. The relaxation times are found to be on the order of one Fermi time τ_F of the system, which is about 100 μs. We then developed a new kinetic relaxation model to explicitly incorporate the two relaxation times in our hydrodynamic linear response model.

The model uses four fitting parameters, the isothermal sound frequency ω_T, the two relaxation times τ_η and τ_κ and the initial amplitude of the dominant spatial Fourier component A to fit the oscillatory decay of the density variation in **TIME** domain. The number of fit parameters is the same as we used in the previous experiments. Instead, by replacing η and κ_T with their corresponding relaxation times τ_η and τ_κ, we are able to properly include the effect of finite relaxation times and extract the static shear viscosity and thermal conductivity in the normal fluid regime. The results are then compared to the high-temperature prediction for both transport properties. A consistent up-shift relative to the high-temperature prediction is determined. These universal density shift coefficients were predicted many years ago but have never been systematically measured. Our results provide the first measurements of these universal density shift coefficients of shear viscosity and thermal conductivity for the unitary Fermi gas at normal fluid regime.

We subsequently compared our results with the results of sound attenuation experiment from MIT group [Patel et al. (2020)]. The measured first sound diffusivity D_1 from both experiment are shown in Figure 6.8. Both results have the same T/T_F scaling. Our data ranges from $T/T_F \simeq 0.25$ to $T/T_F \simeq 0.45$. The extrapolation of our data to higher temperature regime agrees with the measured results of MIT group. But at low temperature regime, their results still have a small up-shift relative to ours.

In addition, we applied a Drude model correction for previous experiment results [Wang et al. (2022)], estimated the corresponding static shear viscosity and thermal conductivity. Although the Drude model is just a relatively crude method to determine the second order hydrodynamic effects, it nevertheless provides a way to crosscheck our latest measured results for the static transport properties. The current results for shear viscosity are in agreement with the Durde model correction for previous fast relaxation results, as shown in Figure 6.9. This suggests that the fast relaxation model we used before indeed neglected important information hidden in the finite relaxation time. On the other hand, the measured static thermal conductivities exhibit a significant up-shift compare to the fast relaxation measurements, and are even larger than the corrected value at high temperature regime, as shown in Figure 6.10.

Another way to look at this difference is shown in Figure 5.8, where we plot the two fast relaxation modes explicitly. The fast modes only contribute 1% to the density relaxation, but 10% to the temperature relaxation, which tells us we should expect a larger correction for the static thermal conductivity than the shear viscosity.

Our new time domain method has its advantage to directly extract the static transport properties, compare to the traditional frequency domain method. In frequency domain, it is hard to disentangle the contribution from different modes. Instead, our time domain method focuses on the oscillatory decay of the dominant Fourier mode of the density perturbation, watch how it diffuses as a function of time. We believe our time domain method is general, and it can be extended to study other quantum many-body systems.

7.2 Future direction

So far our experiments have all been carried out with spin-balanced unitary Fermi gas, it is very natural to think about measuring the transport properties of a spin-imbalanced unitary Fermi gas. Just before I finished this thesis, we have successfully implemented another function generator to transfer atoms between different spin states, and we achieved a stable imbalanced ratio. However, the atom number is not good because the spin imbalanced is achieved by transfer one of the two spin states to a third spin state, which is expelled from the trap by a resonant optical pulse. In order to get a high imbalance ratio, we need to transfer and expel more atoms for the minority spin. Further, there is always significant loss during the loading from CO_2 trap to box trap. These are the technical problems we need to fix in the future.

Another topic of great interest is to look at the superfluid regime. The major difference between a superfluid and a normal fluid is the emergence of second sound below the superfluid transition temperature T_C. Other groups, for example [Li et al. (2022); Yan et al. (2024)] , have studied the second sound diffusivity and mapped out the thermograpy of the unitary Fermi gas cross the superfluid transition. With our time domain method, we expect to see that the exponentially decaying thermal mode evolves into an oscillating second sound mode as we cross T_C. However, to achieve the superfluid transition for the unitary Fermi gas, where $T_C/T_F \simeq 0.17$, we need a much higher density in the box.

Our current experiment results clearly suggest a more rigorous calculation of the leading universal density shifted coefficients are needed. Our measurements can serve as a benchmark for future theoretical studies.

REFERENCES

Adams, A., Carr, L. D., Schäfer, T., Steinberg, P., and Thomas, J. E. (2012). Strongly correlated quantum fluids: ultracold quantum gases, quantum chromodynamic plasmas and holographic duality. *New Journal of Physics*, 14(11):115009.

Anderson, M. H., Ensher, J. R., Matthews, M. R., Wieman, C. E., and Cornell, E. A. (1995). Observation of bose-einstein condensation in a dilute atomic vapor. *science*, 269(5221):198–201.

Baird, L., Wang, X., Roof, S., and Thomas, J. (2019). Measuring the hydrodynamic linear response of a unitary fermi gas. *Physical Review Letters*, 123(16):160402.

Baird, L. R. (2019). *Linear Hydrodynamic Response in a Uniform Fermi Gas.* North Carolina State University.

Bloch, I., Dalibard, J., and Nascimbene, S. (2012). Quantum simulations with ultracold quantum gases. *Nature Physics*, 8(4):267–276.

Bloch, I., Dalibard, J., and Zwerger, W. (2008). Many-body physics with ultracold gases. *Reviews of modern physics*, 80(3):885.

Bluhm, M., Hou, J., and Schäfer, T. (2017). Determination of the density and temperature dependence of the shear viscosity of a unitary fermi gas based on hydrodynamic flow. *Physical Review Letters*, 119(6):065302.

Braby, M., Chao, J., and Schäfer, T. (2010). Thermal conductivity and sound attenuation in dilute atomic fermi gases. *Physical Review A*, 82(3):033619.

Braby, M., Chao, J., and Schäfer, T. (2011). Viscosity spectral functions of the dilute fermi gas in kinetic theory. *New Journal of Physics*, 13(3):035014.

Bradley, C. C., Sackett, C., Tollett, J., and Hulet, R. G. (1995). Evidence of bose-einstein condensation in an atomic gas with attractive interactions. *Physical review letters*, 75(9):1687.

Brooker, G. (2003). *Modern classical optics*, volume 8. Oxford University Press.

Bruun, G. M. and Smith, H. (2007). Shear viscosity and damping for a fermi gas in the unitarity limit. *Physical Review A*, 75(4):043612.

Cao, C., Elliott, E., Joseph, J., Wu, H., Petricka, J., Schäfer, T., and Thomas, J. E. (2011). Universal quantum viscosity in a unitary fermi gas. *Science*, 331(6013):58–61.

Chin, C., Bartenstein, M., Altmeyer, A., Riedl, S., Jochim, S., Denschlag, J. H., and Grimm, R. (2004). Observation of the pairing gap in a strongly interacting fermi gas. *Science*, 305(5687):1128–1130.

Chin, C., Grimm, R., Julienne, P., and Tiesinga, E. (2010). Feshbach resonances in ultracold gases. *Reviews of Modern Physics*, 82(2):1225.

Davis, K. B., Mewes, M.-O., Andrews, M. R., van Druten, N. J., Durfee, D. S., Kurn, D., and Ketterle, W. (1995). Bose-einstein condensation in a gas of sodium atoms. *Physical review letters*, 75(22):3969.

DeMarco, B. and Jin, D. S. (1999). Onset of fermi degeneracy in a trapped atomic gas. *science*, 285(5434):1703–1706.

Elliott, E. (2014). *Quantum Transport and Scale Invariance in Expanding Fermi Gases*. PhD thesis, Duke University.

Elliott, E., Joseph, J., and Thomas, J. (2014). Observation of conformal symmetry breaking and scale invariance in expanding fermi gases. *Physical Review Letters*, 112(4):040405.

Enss, T. (2012). Quantum critical transport in the unitary fermi gas. *Physical Review A*, 86(1):013616.

Enss, T., Haussmann, R., and Zwerger, W. (2011). Viscosity and scale invariance in the unitary fermi gas. *Annals of Physics*, 326(3):770–796.

Fano, U. (1961). Effects of configuration interaction on intensities and phase shifts. *Physical review*, 124(6):1866.

Feshbach, H. (1958). Unified theory of nuclear reactions. *Annals of Physics*, 5(4):357–390.

Floyd, R. W. (1976). An adaptive algorithm for spatial gray-scale. In *Proc. Soc. Inf. Disp.*, volume 17, pages 75–77.

Fox, A. M. (2006). *Quantum optics: an introduction*, volume 15. Oxford University Press, USA.

Frank, B., Zwerger, W., and Enss, T. (2020). Quantum critical thermal transport in the unitary fermi gas. *Physical Review Research*, 2(2):023301.

Ho, T.-L. (2004). Universal thermodynamics of degenerate quantum gases in the unitarity limit. *Physical review letters*, 92(9):090402.

Hofmann, J. (2020). High-temperature expansion of the viscosity in interacting quantum gases. *Physical Review A*, 101(1):013620.

Hou, Y.-H., Pitaevskii, L. P., and Stringari, S. (2013). Scaling solutions of the two-fluid hydrodynamic equations in a harmonically trapped gas at unitarity. *Physical Review A*, 87(3):033620.

Houbiers, M., Stoof, H. T. C., McAlexander, W. I., and Hulet, R. G. (1998). Elastic and inelastic collisions of ^{6}Li atoms in magnetic and optical traps. *Phys. Rev. A*, 57:R1497–R1500.

Hu, J., Urvoy, A., Vendeiro, Z., Crépel, V., Chen, W., and Vuletić, V. (2017). Creation of a bose-condensed gas of 87rb by laser cooling. *Science*, 358(6366):1078–1080.

Joseph, J., Clancy, B., Luo, L., Kinast, J., Turlapov, A., and Thomas, J. (2007). Measurement of sound velocity in a fermi gas near a feshbach resonance. *Physical review letters*, 98(17):170401.

Joseph, J., Elliott, E., and Thomas, J. (2015). Shear viscosity of a unitary fermi gas near the superfluid phase transition. *Physical Review Letters*, 115(2):020401.

Ketterle, W. and Zwierlein, M. W. (2008). Making, probing and understanding ultracold fermi gases. *La Rivista del Nuovo Cimento*, 31:247–422.

Kinast, J. (2006). *Thermodynamics and Superfluidity of a Strongly Interacting Fermi Gas*. Duke University.

Kinast, J., Hemmer, S., Gehm, M., Turlapov, A., and Thomas, J. (2004). Evidence for superfluidity in a resonantly interacting fermi gas. *Physical Review Letters*, 92(15):150402.

Krinner, S., Stadler, D., Husmann, D., Brantut, J.-P., and Esslinger, T. (2015). Observation of quantized conductance in neutral matter. *Nature*, 517(7532):64–67.

Ku, M. J., Ji, W., Mukherjee, B., Guardado-Sanchez, E., Cheuk, L. W., Yefsah, T., and Zwierlein, M. W. (2014). Motion of a solitonic vortex in the bec-bcs crossover. *Physical review letters*, 113(6):065301.

Ku, M. J., Sommer, A. T., Cheuk, L. W., and Zwierlein, M. W. (2012). Revealing the superfluid lambda transition in the universal thermodynamics of a unitary fermi gas. *Science*, 335(6068):563–567.

Landau, L. D. and Lifshitz, E. M. (2013). *Fluid mechanics: Landau And Lifshitz: course of theoretical physics, Volume 6*, volume 6. Elsevier.

Lee, B. (2008). Introduction to±12 degree orthogonal digital micromirror devices (dmds). *Texas Instruments*, pages 2002–2018.

Li, X., Huang, J., and Thomas, J. (2024). Universal hydrodynamic transport times in the normal phase of a unitary fermi gas. *arXiv preprint arXiv:2402.14104*.

Li, X., Luo, X., Wang, S., Xie, K., Liu, X.-P., Hu, H., Chen, Y.-A., Yao, X.-C., and Pan, J.-W. (2022). Second sound attenuation near quantum criticality. *Science*, 375(6580):528–533.

Navon, N., Smith, R. P., and Hadzibabic, Z. (2021). Quantum gases in optical boxes. *Nature Physics*, 17(12):1334–1341.

O'hara, K., Hemmer, S., Gehm, M., Granade, S., and Thomas, J. (2002). Observation of a strongly interacting degenerate fermi gas of atoms. *Science*, 298(5601):2179–2182.

Patel, P. B., Yan, Z., Mukherjee, B., Fletcher, R. J., Struck, J., and Zwierlein, M. W. (2020). Universal sound diffusion in a strongly interacting fermi gas. *Science*, 370(6521):1222–1226.

Romatschke, P. and Young, R. E. (2013). Implications of hydrodynamic fluctuations for the minimum shear viscosity of the dilute fermi gas at unitarity. *Physical Review A*, 87(5):053606.

Sakurai, J. J. and Commins, E. D. (1995). Modern quantum mechanics, revised edition.

Shankar, R. (2012). *Principles of quantum mechanics*. Springer Science & Business Media.

Sidorenkov, L. A., Tey, M. K., Grimm, R., Hou, Y.-H., Pitaevskii, L., and Stringari, S. (2013). Second sound and the superfluid fraction in a fermi gas with resonant interactions. *Nature*, 498(7452):78–81.

Sommer, A., Ku, M., Roati, G., and Zwierlein, M. W. (2011). Universal spin transport in a strongly interacting fermi gas. *Nature*, 472(7342):201–204.

Son, D. (2007). Vanishing bulk viscosities and conformal invariance of the unitary fermi gas. *Physical review letters*, 98(2):020604.

Stellmer, S., Pasquiou, B., Grimm, R., and Schreck, F. (2013). Laser cooling to quantum degeneracy. *Physical review letters*, 110(26):263003.

Strinati, G. C., Pieri, P., Röpke, G., Schuck, P., and Urban, M. (2018). The bcs–bec crossover: From ultra-cold fermi gases to nuclear systems. *Physics Reports*, 738:1–76.

Taylor, E. and Randeria, M. (2010). Viscosity of strongly interacting quantum fluids: Spectral functions and sum rules. *Physical Review A*, 81(5):053610.

Truscott, A. G., Strecker, K. E., McAlexander, W. I., Partridge, G. B., and Hulet, R. G. (2001). Observation of fermi pressure in a gas of trapped atoms. *Science*, 291(5513):2570–2572.

Ulichney, R. (1987). *Digital halftoning*. MIT press.

Wang, X. (2022). *Hydrodynamic Relaxation in a Unitary Fermi Gas*. North Carolina State University.

Wang, X., Li, X., Arakelyan, I., and Thomas, J. (2022). Hydrodynamic relaxation in a strongly interacting fermi gas. *Physical Review Letters*, 128(9):090402.

Wlazłowski, G., Magierski, P., and Drut, J. E. (2012). Shear viscosity of a unitary fermi gas. *Physical Review Letters*, 109(2):020406.

Yan, Z., Patel, P. B., Mukherjee, B., Vale, C. J., Fletcher, R. J., and Zwierlein, M. W. (2024). Thermography of the superfluid transition in a strongly interacting fermi gas. *Science*, 383(6683):629–633.

Yefsah, T., Sommer, A. T., Ku, M. J., Cheuk, L. W., Ji, W., Bakr, W. S., and Zwierlein, M. W. (2013). Heavy solitons in a fermionic superfluid. *Nature*, 499(7459):426–430.

Zhang, Y. (2012). *Radio Frequency Spectroscopy Of a Quasi-Two-Dimensional Fermi Gas*. PhD thesis, Duke University.

Zhou, H. and Ma, Y. (2021). Thermal conductivity of an ultracold fermi gas in the bcs-bec crossover. *Scientific Reports*, 11(1):1228.

Zwierlein, M. W. (2016). Thermodynamics of strongly interacting fermi gases. In *Proceedings of the International School of Physics' Enrico Fermi*, volume 191, pages 143–220.

Zwierlein, M. W., Abo-Shaeer, J. R., Schirotzek, A., Schunck, C. H., and Ketterle, W. (2005). Vortices and superfluidity in a strongly interacting fermi gas. *Nature*, 435(7045):1047–1051.

APPENDIX

APPENDIX

A

MIRROR CLOCKING PULSES

The DMD pixel is an electro-mechanical element in that there are two stable micromirror states (+12^o and -12^o for most current DMDs) that are determined by geometry and electrostatics of the pixel during operation.

Below each micromirror is a memory cell formed from dual CMOS memory elements. The state of the two memory elements are not independent, but are always complimentary. If one element is logical 1, then the other element is logical 0, and vice versa. The state of the pixel memory cell plays a part in the mechanical position of the micromirror, however, loading the memory cell does not automatically change the mechanical state of the micromirror [Lee (2008)].

In order for the state of the CMOS memory to be transferred to the mechanical position of the micromirror, the pixel must receive a "mirror clocking pulse" (formerly referred to as a "reset"). This mirror clocking pulse momentarily releases the micromirror and then re-lands it based on the state of the CMOS memory below. Therefore, it is important that the memory cell is not overwritten during a mirror clocking pulse operation. This allows the memory of groups of pixels to be pre-loaded and their mechanical position to be changed simultaneously with a mirror clocking pulse [Lee (2008)].

In our daily experiment, we found that this "mirror clocking pulse" (MCP) caused some serious problems. The two TI DLP6500 we use to create the horizontal box walls and perturbation beam, the MCP resulted a continuous ’glitch’ of projected pattern. Figure A.1 shows power readout on the oscilloscope of the DMD pattern, it is measured by a photodiode. In our case the pulse occurred every 105 μs.

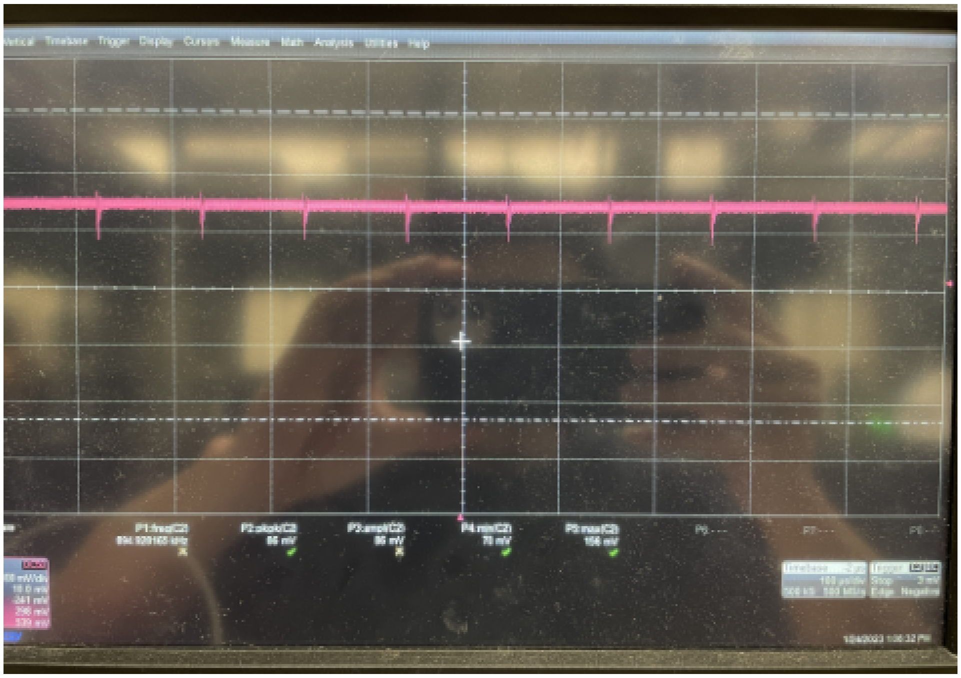

Figure A.1: Power glitching due to MCP, the pulse occurred every 105 μs.

This pulsing does not cause much trouble for making the box, because the walls only contact with a small portion of atoms near the edge. But the perturbation beam is different, it is directly projected into the box. Therefore, the pulsing may cause unwanted heating or even loss of considerable number of atoms.

After discussion with technicians from Texas Instruments (TI), the issue is resolved. The solution is to set the exposure time to 105 μs, and only use external trigger for frame advance. In addition, one must use the latest version of DLP GUI issued by TI. The latest version include a feature of maintaining the frame, which is done by uncheck the "clear" box option. Together with the first two steps, these ensure that we do not have this power glitching during the whole experiment cycle.